Wind tunnel experiments with a model turbine: Dynamic inflow investigation

Frederik Thore Berger

Von der Fakultät für Mathematik und Naturwissenschaften
der Carl von Ossietzky Universität Oldenburg
zur Erlangung des Grades und Titels eines

DOKTORS DER INGENIEURWISSENSCHAFTEN
DR.-ING.

angenommene Dissertation

von Herrn Frederik Thore Berger
geboren in Baden, Schweiz

Gutachter: Prof. Dr. Martin Kühn

Zweitgutachter: Prof. Dr. Carlos Simão Ferreira

Tag der Disputation: 17.06.2022

to
Maria, Freja and Henrik

Abstract

The dynamic inflow effect describes the unsteady aerodynamic response to fast changes in rotor loading due to a gradual adaption of the rotor induction. The effect leads to dynamic loads that cannot be caught by the basic Blade Element Momentum (BEM) theory. Dynamic inflow engineering models are used for BEM based aeroelastic simulations to obtain relevant loads in the design, certification and controller tuning process of wind turbines. The objective of this thesis was to increase the understanding of the dynamic inflow effect due to pitch steps and wind gusts on the basis of scaled experiments in the wind tunnel and thus also allow for engineering model improvements.

For the wind tunnel experiments, a scaled model turbine, closely resembling the induction aerodynamics of a contemporary multi MW reference turbine, was designed. The model features several sensors and has fast pitch and torque control capabilities.

A pitch step experiment was conducted, applying a novel method to directly probe the radially resolved rotor induction, which is the signal of interest. The results show a clear asymptotic decay of the axial wake induction factor and thus the first direct experimental evidence of dynamic inflow for wind turbines. The radial dependency of this decay process and the differences between pitch directions is discussed based on time constants, which are obtained from fitted exponential models. The further analysis of near wake and load measurements gives a comprehensive overview of the effect.

The experiment is compared with different engineering models, a free vortex wake model (FVWM) and an actuator line (AL) large eddy simulation. The trends in the radial dependency of the experiment can also be seen in the FVWM and AL simulations. Comparing different dynamic inflow engineering models, the Øye model performed closest to the experiment.

In another wind tunnel campaign, rotor coherent gusts were generated in a reproducible manner with an active grid and imposed to the model turbine. The dynamic inflow effect due to gusts was experimentally shown for the first time. It is extracted as the difference between the dynamic experiment and a quasi-steady case, interpolated from a steady experimental characterisation through the wind gust. The dynamic inflow effect leads to reduced load amplitudes, in contrast to common engineering models, which indicate an increase. This is caused by the induced velocity, which exhibits an amplified behaviour during a gust in the experiment and a reduced amplitude in the engineering models. FVWM was proven to catch the phenomenon correctly. A new implementation of the Øye dynamic inflow model to also catch the gust phenomenon is proposed.

This experimentally driven thesis increases the understanding of the mechanisms of dynamic inflow for pitch steps and introduces the relevance of the effect for gust situations.

Zusammenfassung

Der ′dynamic inflow′ Effekt beschreibt die instationäre aerodynamische Reaktion auf schnelle Änderungen der Rotorbelastung durch eine graduelle Anpassung der Rotorinduktion. Der Effekt führt zu dynamischen Belastungen, die von der grundlegenden Blatt-Element-Impulstheorie (BEM) Theorie nicht erfasst werden können. ′Dynamic inflow′ Ingenieurmodelle werden für BEM-basierte aeroelastische Simulationen verwendet, um relevante Lasten bei der Konstruktion, Zertifizierung und Reglerabstimmung von Windturbinen zu erhalten. Das Ziel dieser Arbeit war es, das Verständnis des ′dynamic inflow′ Effektes durch Pitchschritte und Windböen auf der Basis von skalierten Experimenten im Windkanal zu verbessern und damit auch Verbesserungen der Ingenieurmodelle zu ermöglichen.

Für die Windkanalversuche wurde eine skalierte Modellwindturbine entworfen, die die Induktionsaerodynamik einer modernen Multi-MW-Referenzturbine abbildet. Das Modell ist mit mehreren Sensoren ausgestattet und verfügt über eine schnelle Pitch- und Drehmomentsteuerung.

Es wurde ein Pitchschritt-Experiment durchgeführt, bei dem eine neuartige Methode zur direkten Messung die radial aufgelöste Rotorinduktion, angewandt wurde. Die Ergebnisse zeigen ein deutliches asymptopisches Abklingen des axialen Nachlaufinduktionsfaktors und damit den ersten direkten experimentellen Nachweis des ′dynamic inflow′ Effektes bei Windkraftanlagen. Die radiale Abhängigkeit des Abklingprozesse und die Unterschiede zwischen den Pitchschrittrichtungen werden anhand von Zeitkonstanten diskutiert, die aus Exponentialmodellen gewonnen werden. Die weitere Analyse von Nachlauf- und Lastmessungen gibt einen umfassenden Überblick über den Effekt.

Das Experiment wird mit verschiedenen Ingenieurmodellen verglichen, einer ′free vortex wake′ Methode (FVWM) und einer Large Eddy Aktuator Linien Simulation (AL). Die radialen Trends des Experiments sind auch in diesen FVWM- und AL-Simulationen zu erkennen. Beim Vergleich verschiedener Ingenieurmodelle stimmt das Øye-Modell am Besten mit dem Experiment überein.

In einer weiteren Windkanal Kampagne wurden rotorkohärente Böen auf reproduzierbare Weise mit einem aktiven Gitter erzeugt und der Modellturbine aufgeprägt. Der ′dynamic inflow′ Effekt durch Böen wurde zum ersten Mal experimentell nachgewiesen. Er wird als Differenz zwischen dem dynamischen Experiment und einem quasistationären Fall extrahiert. Der quasistationäre Fall basiert auf einer stationären Charakterisierung und wird über die Windböe interpoliert. Der 'dynamic inflow' Effekt führt zu reduzierten Lastamplituden, im Gegensatz zu gängigen Ingenieurmodellen, die eine Erhöhung anzeigen. Dies ist auf die induzierte Geschwindigkeit zurückzuführen, die im Experiment während einer Böe eine höhere Amplitude und im Ingeniermodell eine reduzierte Amplitude zeigt. Es hat sich gezeigt, dass der Effekt mit FVWM korrekt erfasst wird. Es wird eine verbesserte Implementierung des Øye 'dynamic inflow' Ingeniermodells vorgeschlagen, das auch den Effekt aufgrund von Böen abbildet.

Diese experimentell gestützte Arbeit erweitert das Verständnis der Mechanismen des 'dynamic inflow' Effektes für Pitchschritte und zeigt die Relevanz des Effekts für Böen auf.

Contents

List of Figures

List of Tables

List of Symbols and Abbreviations

Symbols	**Definition**
α	angle of attack
β	azimuth angle of the sampling point
γ	geometrical angle between chord and rotor plane
Γ	circulation
ε	Gaussian width
η	dynamic viscosity
Θ	inflow angle
λ_D	design tip speed ratio
ρ	density
ρ_{xy}	Pearson correlation coefficient
τ	time constant
τ_{typ}	typical single time constant for dynamic inflow
τ_{fast}, τ_{slow}	time constants for two-time-constant Øye model
Ω	angular rotor speed
a	axial induction factor
a'	tangential induction factor
c	chord length
C_{L}	lift coefficient
C_{D}	drag coefficient
C_{M}	rotor moment coefficient
C_{P}	power coefficient
C_{T}	thrust coefficient

C_{flap}	flapwise blade root bending coefficient
D	diameter
F	tip loss correction factor
F_{L}	lift force
F_{D}	drag force
F_{N}	normal force
F_{T}	tangential force
F_{thrust}	thrust force
f_i	projected force field
I_{rot}	rotational inertia of rotor and drivetrain
k	constant for Øye model
k_u	constant for improved Øye model
l	characteristic length
M_{aero}	aerodynamic rotor torque
M_{flap}	flapwise blade root bending moment
N	number of blades
n_{L}	length scaling factor
n_{T}	time scaling factor
N_{crit}	critical background turbulence parameter
r	radial position
R	Radius
Re	Reynolds number
T	time period
u_0	undisturbed global (spatial mean) reference wind velocity
$\overline{u_0}$	mean undisturbed global (spatial mean) reference wind velocity
$u_{0,\mathrm{local}}$	local reference wind velocity
u_{ax}	axial velocity in rotor plane
u_{ta}	tangential velocity in rotor plane
u_{i}	blade induced velocity
u_{ind}	wake induced velocity

u_{rel}	relative velocity at rotor segment

Abbreviation	**Definition**
AD	Actuator Disk
AL	Actuator Line
AoA	Angle of attack
BEM	Blade Element Momentum
BET	Blade Element Theory
BMWi	Federal Ministry for Economic Affairs and Energy, Germany
CFD	Computational Fluid Dynamics
DTU	Technical University of Denmark
EAWE	European Academy of Wind Energy
ECN	Energy Center of the Netherlands
EU	European Union
FAST	Fatigue Aerodynamics Stresses Turbulence
FVWM	Free Vortex Wake Method
GDWM	Generalised Dynamic Wake Model
GH	Garrad Hassan
HAWC2	Horizontal Axis Wind turbine Code 2nd ed.
IEA	International Energy Agency
LDA	Laser Doppler Anemometer
LES	Large Eddy Simulation
LLT	Lifting Line Theory
MoWiTO	Model Wind Turbine Oldenburg
MEXICO	Model EXperiment in controlled COnditions
NASA	National Aeronautics and Space Administration
NI	National Instruments
NREL	National Renewable Energy Laboratories
NTNU	Norwegian University of Science and Technology
Polimi	Polytechnic University of Milan

TSR	Tip Speed Ratio
TUD	Technical University of Delft
TUM	Technical University of Munich

Chapter 1

Introduction

Long term research challenges in wind energy were outlined by representatives of 13 European and one US universities and institutes focusing on wind energy and organised within the European Academy of Wind Energy (EAWE), in *Van Kuik et al. (2016)*. An objective is to identify current technological and scientific barriers and thus stimulate overcoming them to accelerate wind energy penetration and development in the energy mix.

Aerodynamics is defined as a central topic in wind energy research. A fundamental challenge is the multi-scale nature of the flow phenomena, which needs to be analysed, reaching from the scale of 10^{-3} m in the boundary layer forming over the wind turbine blades up to 10^{5} m for the interaction of wind farm clusters. This wide spread of scales cannot be resolved with high fidelity computational fluid dynamic (CFD) simulations. For a competitive utilisation of wind energy, efficient design methodologies and tools are needed. Especially for the design of wind turbines and farms, engineering models are needed to catch unsteady aerodynamic effects (e.g. for dynamic stall, oblique inflow and dynamic inflow). Such models are increasingly used, however questions remain if they represent all relevant physics *(Van Kuik et al., 2016)*.

Van Kuik et al. (2016) define model validation through scaled wind tunnel experiments in controlled conditions as a critical challenge. A common disadvantage in wind tunnel experiments is the limited possibilities for realistic and unsteady inflow conditions. They further argue that validation is often performed based on integral measurements hiding error cancellation. Therefore development and application of new techniques to directly obtain the relevant quantities from experiments is needed.

In this dissertation, these challenges are addressed for the wind turbine load response on fast blade pitch changes and wind gusts. Wind tunnel experiments with a purpose designed model wind turbine and an active grid for reproduction of realistic gust and turbulence conditions in the wind tunnel form the basis. Beyond pure validation, it is aimed for an increase in the understanding of the relevant physics.

1.1 State of the art

In this section, the state of the art for the general interaction of inflow conditions with rotor aerodynamics and the dynamic inflow effect including relevant model development steps are introduced. In the last part, an overview on different kinds of scaled wind turbines for wind tunnel experiments is given, focusing on the specific design driving objectives.

1.1.1 Interaction of inflow conditions and rotor aerodynamics

Wind turbines operate in the atmospheric boundary layer with a large variety of inflow conditions, including shear, gusts and turbulence. With the gradually growing rotor diameters, the unsteadiness of the wind field over the swept area increases. Further, the turbine control actively interacts through pitch actuation of the rotor blades and rotor speed changes with the flow, leading to highly dynamic fluctuations in the rotor flow. These fluctuations result from the extraction of kinetic energy from the wind flow, described by the slowing down of the axial velocity component, the induced velocity, and the change in the tangential velocity component due to the formed induction zone and wake. This combination leads to high complexity in obtaining the relevant turbine loads.

Aero-servoelastic simulations are used in industry and academia for the calculation of wind turbine design loads in various operating conditions. The 'servo' part in these simulations is resting on control inputs to the turbine actuators (e.g. generator torque, blade pitch motors, yaw mechanism and the flaps of future smart blades). The 'elastic' part of the simulations is based on multibody formulations of the different structural parts that move, deform and are connected by joints. The 'aero' part of these simulations is commonly dealt with by the blade element momentum (BEM) theory, which gives the aerodynamic forces acting on the rotor blade segments. BEM however is inherently based on steady and uniform flow assumptions, and engineering models need to be used to model dynamic phenomena *(Hansen, 2008)*.

Mid and high fidelity representations of the 'aero' part in aero-servoelastic simulations are free vortex wake methods (FVWM) *(Boorsma et al., 2020)* and computational fluid dynamics (CFD) *(Dose et al., 2020)*, respectively. The wake is physically resolved for both simulation types, and the induced velocity is obtained based on this representation. Effects of wind unsteadiness and control inputs on the loads are intrinsically modelled. For CFD further, the airfoil aerodynamics are physically modelled, whereas FVWM depends on prescribed airfoil characteristics like BEM.

1.1.2 Dynamic inflow

The dynamic inflow effect is an unsteady aerodynamic phenomenon observed on unducted aerodynamic rotors due to sudden changes in the aerodynamic rotor load. The effect leads to dynamic peaks in the lift force and thus rotor loading and is essential for helicopters, for which the effect was firstly observed and investigated, as well as for pitch regulated wind turbines. The main process is sketched in Fig. 1.1 for the pitch step on a wind turbine from a low to high turbine load. Between the stationary operation states prior and after the load event, the stream-tube, representing the flow through the rotor consisting of upstream induction zone and downstream wake, has to adapt. Due to the inertia of the air in the stream-tube the axial induction, more specifically induced velocity, only adapts gradually to the new steady state and the turbine loads show an overshoot.

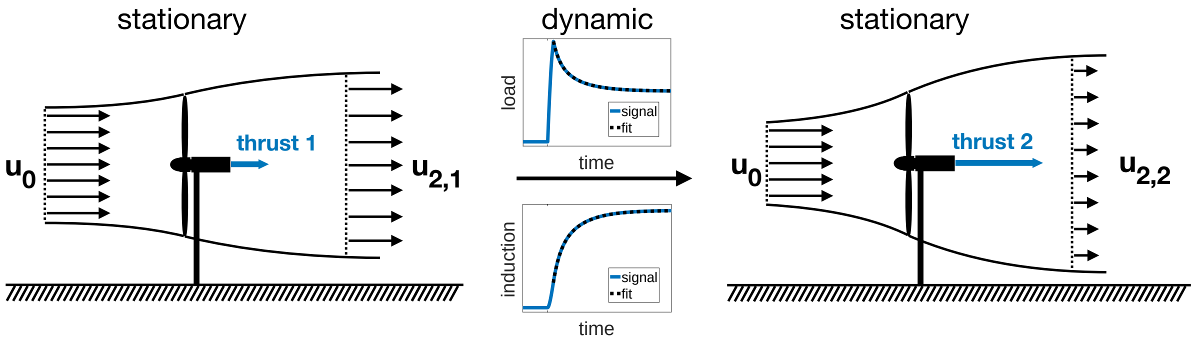

Figure 1.1: Indicated course of dynamic turbine load and induction for a sudden pitch step to higher load at constant wind velocity with stream-tubes for the steady start and end point.

Peters (2009) outlines the history and ongoing and future relevance of simple dynamic inflow models for helicopter applications. In the early 1950ies *Carpenter and Fridovich (1953)* describe a dynamic response of the rotor thrust and induced velocity to a rapid blade pitch increase on a full scale helicopter rotor test setup. From a zero load operation, the dynamic thrust reaches nearly twice the new steady thrust level directly after the pitch step. They describe a delayed buildup of induced velocity that is indicated by the measured drag force on balsa wood paddles positioned in the near wake. This buildup is explained by the air mass that needs to be initially accelerated before the new steady operational point is reached. Based on an analogy with a moving impervious disk they estimate this additional apparent mass leading to the first dynamic inflow model for pitch steps, providing reasonable prediction of the thrust force overshoots. In the following decades, models were continuously refined, with an essential step being the development of the model by *Pitt and Peters (1981)*. This model was adopted on a broad scale for design, control and simulation applications *(Peters, 2009)*. Building on these model evolvements, additional operational cases were added, which are relevant for helicopters. One of the main conclusions of *Peters (2009)* on the historical development of the understanding and modelling of the dynamic inflow effects for helicopters is, that main advances always have been triggered by experimental data, that did not fit the current models.

Stall-regulated wind turbines of the ′classic Danish design′ were the predominant commercial turbine type before and in the 1980ies *(Gasch and Twele, 2012)*. These turbines are directly connected to the grid by induction generators and operate at nearly constant rotational speed and constant blade pitch angle. No sudden rotor load changes are expected, and the dynamic inflow phenomenon was of little practical interest for wind turbines. In the 1990ies, variable speed wind turbines with pitch to feather (decrease of the angle of attack) control to limit power and loads at high wind velocities were commissioned on large scales *(Gasch and Twele, 2012)*. For these turbines with pitch actuation and changes in rotor speed, the dynamic inflow effect moved into the research focus.

The main difference concerning the effect between wind turbines and helicopters is based on the design objective of a high thrust force at low power input for helicopters and high power output from the available wind for wind turbines. This leads to lower typical axial induction factors for helicopter designs than for an optimal wind turbine design and the application of linearized helicopter models for wind turbine applications should be questioned *(Snel and Schepers, 1994)*.

Within two historic EU projects on dynamic inflow *(Snel and Schepers, 1994; Schepers and Snel, 1995)*, the first generation of dynamic inflow engineering models for wind turbines (e.g. Øye, ECN, adapted version of Pitt and Peters) were compared and tested for pitch steps and a gust case. An experiment with a 1.2 m diameter model turbine with constant chord length was performed in a wind tunnel with a gust generator. Investigations of that experiment and simulations of that case did not show a clear dynamic inflow effect. It was concluded that the gust was not fast and severe enough to trigger such effects. An important first pitch step test case have been the free field measurements of out-of-plane blade root bending moments and rotor shaft torque on the 2 MW Tjæreborg wind turbine *(Øye, 1991)*, which are still used as a reference today.

The dynamic inflow effect for wind turbines was further investigated based on the up to date largest model experiment for wind turbines, i.e. with a diameter of 10 m, under controlled wind conditions within the NREL unsteady aerodynamics experiments phase VI in the NASA AMES wind tunnel (see *Hand et al., 2001*, organised within the IEA Wind task 20). A pitch step experiment between no loading and a very high loading in the turbulent wake state was performed, and integral loads and blade pressure derived local aerodynamic forces were used for investigations. *Schepers (2007)* fitted an exponential decay model with one time constant to this data to investigate the decay process of the normal forces. He found relevant differences between the radial dependence of these time constants of the experiment and a cylindrical wake model used to obtain time constants for the ECN dynamic inflow engineering model *(Snel and Schepers, 1994)*.

Based on the 'Model Experiment in Controlled Conditions' (MEXICO) *(Schepers and Snel, 2008)* and 'New MEXICO' *(Boorsma and Schepers, 2014)* the dynamic inflow effect was also investigated based on blade pressure derived local aerodynamic forces for pitch steps on the MEXICO model turbine, i.e. with a diameter of 4.5 m, within the Mexnext project phases (phase 1 *Schepers et al., 2012*, phase 2 *Schepers et al., 2014* and phase 3 *Boorsma et al., 2018*, organised within IEA Wind Task 29). The pitch steps were slower than for the phase VI experiment (compared to one rotor revolution) and the normal force signals showed no sufficiently smooth decay process for time-constant analysis. Further numerical cases were considered within the IEA task 29, and it was shown how unsteady aerodynamic effects on the blade level also influence the force overshoot, thus hiding part of the dynamic inflow effect. *Pirrung and Madsen (2018)* conclude that normal forces from measurements or simulations are not suited well for the tuning of time constants in dynamic inflow models and efforts should be taken to directly probe the induced velocity, which are readily available from FVWM simulations, however not available easily from CFD simulations or experiments. They further react to the observed mismatch in the one time-constant exponential fit by *Schepers (2007)*. Also, based on a cylindrical wake model, they show how the mismatch can be cleared by modelling the dynamic inflow effect with two time constants.

The recent development of improved dynamic inflow models by *Yu et al. (2019)* and *Madsen et al. (2020)* further demonstrat, on the one hand, the current interest on the dynamic inflow effect and, on the other hand that no consensus on a best practice model exists, indicating a lack of information on the actual effect.

1.1.3 Scaled wind turbines for wind tunnel experiments

Schepers and Schreck (2018) emphasize the need for detailed aerodynamic measurements on scaled wind turbines in a controlled environment for an improved understanding of wind turbine aerodynamics. The EAWE wind tunnel testing committee (WTTC *2022*) was proposed at the 'wind energy science & wind tunnel experiments experts meeting' at ForWind - University of Oldenburg in March 2018 to enhance communication between universities and research institutes. The aim is to investigate the influence of different wind tunnels, measurement devices and model turbines in experiments and to provide a general overview of the facilities and hardware.

In the following, an overview of different model turbines is given. They are assigned in Fig. 1.2 to clusters based on diameter and design tip speed ratio λ_D, which is the tip speed ratio (TSR) the blade design is based on. The turbines in each cluster were designed for similar research objectives that dictated that design. Isolines for representative Reynolds number Re are plotted. The Reynolds number defines the ratio of inertial to frictional forces in the blade boundary layer and is the most important scaling issue for wind tunnel experiments. Depending on the objectives for the model turbine, requirements on Re differ, as explained in more detail below.

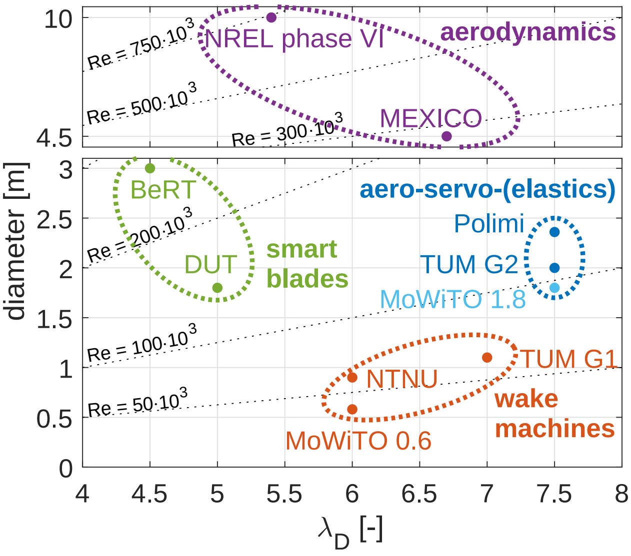

Figure 1.2: Overview of representative model wind turbines for different objectives, based on design tip speed ratio and diameter.

Re is defined by Eq. (1.1).

$$\mathrm{Re} = \frac{l \cdot u_{\mathrm{rel}} \cdot \rho}{\eta} \tag{1.1}$$

The density of air ρ and the dynamic viscosity η are constant (at lab conditions). In our comparison, the characteristic length l is the chord length c, based on a Betz design *(Gasch and Twele, 2012)* for a fixed position at 80 % span of the blade. It is proportional to the radius of the turbine R, the number of blades N, λ_D and the design lift coefficient $C_{\mathrm{L,D}}$, as outlined in Eq. (1.2). The reference velocity u_{rel} is the relative velocity at the blade segment, proportional to the wind velocity u_0 and λ_D, as given in Eq (1.2). The resulting Re isolines are given for a design lift coefficient of 0.8 and a reference wind velocity of $6\,\mathrm{ms}^{-1}$.

$$\text{with} \quad l = c_{0.8\mathrm{R}} \propto \frac{R}{N \cdot \lambda_D^2 \cdot C_{\mathrm{L,D}}} \quad \text{and} \quad u_{\mathrm{rel}} \propto \lambda_D \cdot u_0 \quad \text{follows} \quad Re \propto \frac{R \cdot u_0}{\lambda_D \cdot N \cdot C_{\mathrm{L,D}}} \tag{1.2}$$

The above mentioned NREL phase VI experiments *(Hand et al., 2001)* were performed on a two-bladed turbine. with relatively light composite blades made from fibre glass and carbon fibre. One blade featured the measurement of pressure distributions at five radial stations and both blades had strain gauges at the blade root and fast pitching motors. Experiments were performed at constant rotor speed in different inflow speeds and focused on blade aerodynamics. The experiments with the MEXICO turbine *(Schepers and Snel, 2008)* focused on blade and induction aerodynamics. In addition to pressure measurements on one of the three rather heavy aluminium blades, the flow around the rotor was investigated based on particle image velocimetry (PIV) measurements.

Both examples aim at high Reynolds numbers for scaled experiments by either large rotor size (NREL phase VI) or a combination of large rotor size and high design wind velocity (MEXICO). They are not derived from actual turbines but designed for lower λ_D, increasing the Re values. The designs are based on a representative C_{T} and the turbines operate at steady setpoints or perform predefined manoeuvres. They form the two large model experiments on aerodynamics that have both been carried out within a large consortium of institutes and universities as part of IEA tasks (20 and 29) and are thus labelled 'aerodynamics' in Fig. 1.2.

For these two turbines, different Re values are reported than indicated by the Re-isoline estimation in Fig. 1.2. The isoline values can be easily adjusted with the proportionality in Eq (1.2) to changed parameters. The NREL phase VI turbine has two blades (instead of 3, thus a factor of $\frac{3}{2}$ for the Re isolines) and the MEXICO turbine operates at $15\,\mathrm{ms}^{-1}$ (instead of $6\,\mathrm{ms}^{-1}$, thus a factor of $\frac{15}{6}$ to the Re isolines) leading to an indicated Re value of $1.1 \cdot 10^6$ compared to a reported typical chord-based Re of $1 \cdot 10^6$ and indicated Re of $0.75 \cdot 10^6$ (at the nearest isoline) compared to reported $0.8 \cdot 10^6$, respectively. Unless mentioned or for a two-bladed design, the isolines give a good indication for the following examples. In general, a critical threshold of $50 \cdot 10^3$ is often considered as minimum Re, below which the flow over an airfoil is mainly separated *(Winslow et al., 2018)*.

The category of 'smart blades' in Fig. 1.2 is represented by a two-bladed model of Delft University of Technology (DUT) *(Hulskamp et al., 2011)* and the 'Berlin Research Turbine' (BeRT) *(Soto-Valle et al., 2020)* of Technical University of Berlin. These turbine types use a low λ_D and maximum allowable diameter in the respective wind tunnel to maximize the blade chord and thus space for smart actuators. This does also lead to high Re values (for model experiments). Both devices feature load measurements at the blade root but lack a pitch system. These designs are pinpointed to the testing of such smart devices in a rotating system. However, due to the λ_D mismatch, changes in dynamic loading due to the smart actuators cannot be easily mapped to contemporary wind turbines.

In Fig. 1.2, the turbines of the Norwegian University of Science and Technology (NTNU) *(Krogstad and Lund, 2012)*, MoWiTO 0.6 *(Schottler et al., 2016)* and of the Technical University Munich (TUM) G1 *(Campagnolo et al., 2016)* are denoted 'wake machines'. With the smaller size of these turbines, no direct blade loads are measured. The latter two feature pitch actuators. These model turbines are designed for realistic C_T and used to study the far wake of wind turbines in various conditions, the interaction of two and more turbines, and testing of wind farm control approaches. Blades are made from aluminium for the NTNU machine, plastic (injection moulding) for MoWiTO 0.6 and carbon fibre for the TUM G1. They are designed for lower λ_D than actual turbines to increase the Re over $50 \cdot 10^3$. The MoWiTO 0.6 actually reaches Re of over $60 \cdot 10^3$ at $7.5\,\mathrm{ms}^{-1}$ (instead of $6\,\mathrm{ms}^{-1}$, thus a factor of $\frac{7.5}{6}$ to the Re isolines) and is just above the critical threshold of $50 \cdot 10^3$.

The last segment is denoted 'aero-servo-(elastics)', represented by the TUM G2 *(Bottasso et al., 2014)*, the Polytechnic University of Milan (Polimi) turbine *(Bayati et al., 2016)* and the MoWiTO 1.8 *(Berger et al., 2018)*, which was designed in the scope of this thesis. These machines are based on reference multi-MW wind turbines and map the lift distribution of these turbines over the relevant TSR-range. They have individual pitch control (IPC) capabilities and sensors for flapwise blade root bending moments. All turbines have a relatively stiff but lightweight blade set with a carbon fibre shell. For the TUM G2 also an elastically scaled rotor blade based on a foam core and carbon fibre spars, is available *(Campagnolo et al., 2014)*. The experimental focus with these turbines is mainly directed towards turbine control, induction aerodynamics and turbine loads. Due to the scaling approach, certain results, e.g. the identified best pitch amplitude for IPC based load alleviation in a certain shear condition, resemble the amplitude needed for the reference turbine.

Chamorro et al. (2012) showed that the general statistics of wakes is also reproduced by smaller wind turbine models with Re values over $50 \cdot 10^3$, based on the turbine diameter as characteristic length and the wind speed as characteristic velocity. This is achieved with a 0.13 m diameter model at $7\,\mathrm{ms}^{-1}$ wind velocity. Re values at the airfoil level are much lower as can be estimated from Fig. 1.2. Such models show severe flow separation on the blades and thus are not considered here. However they are very valuable for studies on wind farm flows, e.g. as in *Chamorro and Porté-Agel (2011)* and *Bastankhah and Porté-Agel (2019)*.

1.2 Research questions

The motivation that led to the experimental focused research presented in this thesis is the lack of a comprehensive understanding of the dynamic inflow effect for wind turbines.

Despite the long history of research on the related phenomena, there is a multitude of open questions and problems in prior investigations. The two large-sized experiments with pitch steps in controlled conditions within the IEA wind scope concentrated on a few radial pressure derived force transients, concluding on the need to directly probe the induced velocities. Reliable trends of the radial dependency of the decay process still cannot be derived from these experiments, mainly due to the unrealistic scaling of such a change in pitch step in these experiments (model scaling and not representative load levels for contemporary wind turbines). In the single study on the dynamic inflow effect due to gusts, no clear effect was observed. In this study, the slow wind variation during the gust was already assumed to be too slow.

Therefore a new generation of experimental investigations is required to overcome these limitations. This study is based on wind tunnel experiments while also considering engineering models and mid-fidelity simulations to increase the understanding of the dynamic inflow effect. Within the scope of this thesis, the following research questions were addressed:

1. *How can a contemporary wind turbine be scaled in the wind tunnel size for experiments focused on induction aerodynamics?*

2. *What insights on the dynamic inflow process can be obtained from a radially resolved induction measurement of a pitch step experiment in combination with load and near wake measurements?*

3. *How well do common engineering models and FVWM and CFD based AL simulation setups catch the induction and load overshoot characteristic of an experimental pitch step case?*

4. *What are the characteristics of the dynamic inflow effect due to gusts and how can it be modelled by engineering models?*

1.3 Structure of the thesis

This thesis in cumulative form consists of an introduction, four main chapters and conclusions, followed by appendices, as outlined in Fig. 1.3.

Chapter 2 is published in the Journal of Physics: Conference Series as *Berger et al. (2018)*. The scaling approach, mechanical design and aerodynamic characterisation of the designed 'Model Wind Turbine Oldenburg 1.8 m' (MoWiTO 1.8) is described in this contribution.

Chapter 3 is published in the Wind Energy Science Journal as *Berger et al. (2021a)*. In this contribution, the dynamic inflow effect due to a pitch step is investigated based on experimental measurements of the inductions, obtained based on 2D Laser Doppler Anemometer measurements in the rotor plane, hot wire measurements in the near and close far wake and integral load measurements. The first direct evidence of the dynamic inflow effect for a wind turbine application is given. Exponential models are fitted to the data for analysis of the relevant time constants and the radial dependency of the inductions. The dynamic behaviour of the wake is connected to the observed radial dependency of the decay process of the inductions.

Chapter 4 is published in the Journal of Physics: Conference Series as *Berger et al. (2020)*. Here the experiment from Chap. 3 is compared to different engineering models for the dynamic inflow effect, a FVWM simulation setup and an actuator line (AL) simulation in a large-eddy CFD simulation. The time constants of the fitted exponential models are compared as well as load overshoots.

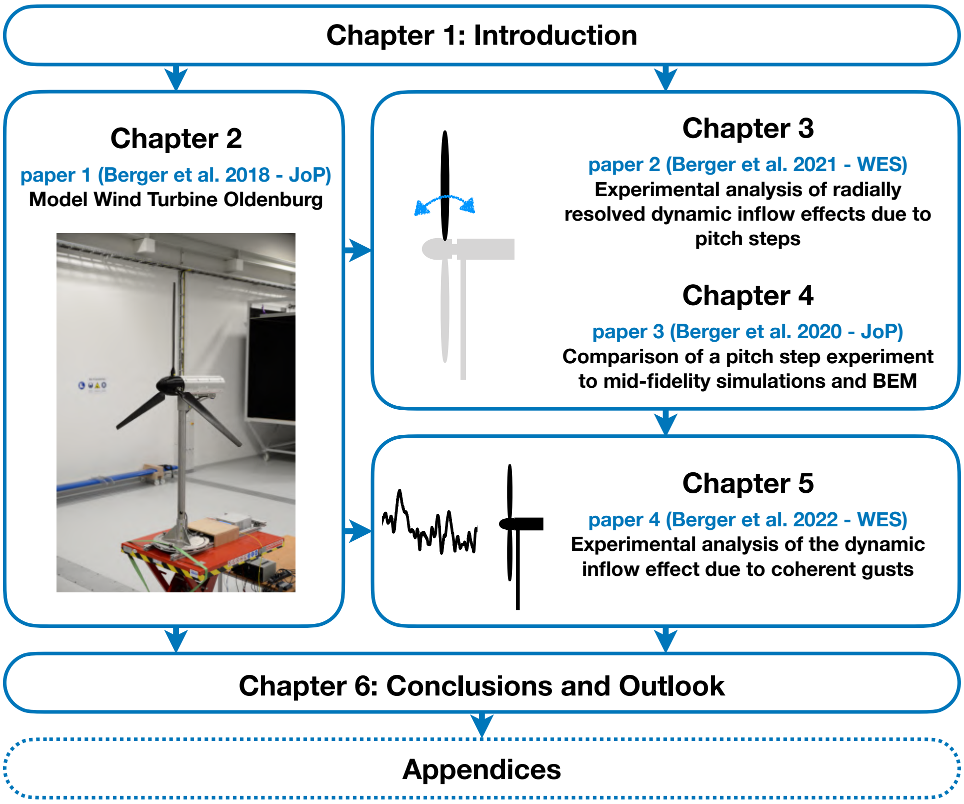

Figure 1.3: Overview of the papers this thesis is based on. WES refers to 'Wind Energy Science Journal' and JoP 'Journal of Physics: Conference Series' papers.

Chapter 5 is published in the Wind Energy Science Journal as *Berger et al., 2022*. Here, the dynamic inflow effect due to gusts is assessed in a wind tunnel experiment. The effect is investigated by comparing two experimental cases. The first case is the dynamic measurement of loads and the velocities in the rotor plane during a rotor coherent gust that is generated with an active grid. For the second case, these measurements are reconstructed for the gust based on a detailed characterisation of the turbine in steady inflow. Thus the dynamic inflow effect is isolated as the difference between the two cases. The identified effect is further compared to a common engineering model and a new implementation of that model to cover gust effects is proposed.

In Chap. 6, the main results and conclusions of Chap. 2 to 5 are summarised and on that basis suggestions for future research questions are given.

In App. A, correction models for MoWiTO measurements and a finely resolved aerodynamic characterisation is presented. In App. B, the relevant turbine information for simulation setups is documented.

Chapter 2

Model Wind Turbine Oldenburg

The content of this chapter, excluding the added amendment, is identical to:

Berger, Frederik, Lars Kröger, David Onnen, Vlaho Petrović and Martin Kühn (2018). 'Scaled wind turbine setup in a turbulent wind tunnel'. In: *Journal of Physics: Conference Series* 1104, p. 012026. `DOI: 10.1088/1742-6596/1104/1/012026`.

Abstract

Wind tunnel experiments with scaled model turbines are a viable complement to field tests and simulations. The scaling of a 5 MW reference turbine with the aim of maintaining the design tip speed ratio and lift distribution is introduced. The machine, named MoWiTO 1.8 (Model Wind Turbine Oldenburg 1.8 m), is described in this paper and the setup in the WindLab wind tunnel of the University of Oldenburg, featuring an active grid, is described. Based on aerodynamic simulations in a turbulent wind field flow, the calculated aerodynamic loads of the reference turbine and the scaled model are compared. Furthermore, the aerodynamic characterization of the machine is presented, with focus on power and thrust coefficients and sensitivity to changes in the Reynolds number. It is shown, that with the chosen approach many attributes of the reference turbine can be scaled into the controllable wind tunnel environment.

Amendment

The content of this chapter is identical to the above mentioned publication and based on the knowledge at that time. In the meantime, this knowledge was extended. The wind tunnel experiments presented in Sect. 2.3.2 show the initial characterisation measurements of the turbine performed in the wind tunnel in 2017. Subsequently the small differences between these measurements, simulations and expected values from scaling were investigated. Three main factors were identified. Firstly, the power coefficient is not corrected for the friction losses in the drivetrain. These friction losses now have been quantified, leading to an increased maximum power coefficient. Secondly, a small mismatch of the initial absolute zero position of the pitch angle was suspected and could be verified in the following measurement campaigns. The pitch angles for the measurements shown in this chapter, therefore, have to be corrected by about -1° (towards stall). Lastly, re-calibration of the strain gauges on the tower in early 2018 showed a slightly changed slope of the calibration curve, leading to about 5% overestimated thrust values in this paper. These mismatches are cosistent for all measurements presented in this chapter and do not change the ratio between those, but only slightly the reference position. Shown FAST 7 simulations are performed at 0° pitch setting. The correction models for torque due to friction, thrust due to tower drag and updated, corrected and finer resolved power and thrust coefficient curves for the design pitch angle are shown in App. A. Relevant information for simulation setups of MoWiTO are additionally documented and linked in App. B.

For an in-depth overview of the various aspects, approaches and limitations in aeroservoelastic downscaling based on non-dimensional numbers the recent publication *Canet et al. (2021)* is recommended to the interested reader as a source of additional information to read after this chapter. Note that the described approach of scaling the non-dimensional circulation (see *Canet et al., 2021* Eq.(8)) can be simplified to the scaling approach based on the non-dimensional lift, which is introduced in this chapter in Eq. (2.3).

2.1 Introduction

Investigations with scaled model wind turbines in the controlled environment of a wind tunnel are a viable addition to simulations and field testing. The aforementioned have the disadvantage of mostly not being able to represent all relevant physical phenomena for simulation models, respectively the unknown and not reproducible boundary conditions of open field test measurements. For scaled wind turbine investigations in the wind tunnel these disadvantages are not present, however the main problem is that in the scaling process not all non-dimensional numbers can be maintained. In addition, space for sensors and actuators is limited.

Besides the large wind tunnel campaigns of NASA Ames *(Hand et al., 2001)* and of the Mexico project *(Schepers and Snel, 2008)*, which focused on aerodynamics, different model wind turbines in the size range of 1 m to 2 m have been designed and used for experiments by various researchers, e.g. *Hulskamp et al. (2011)* and *Bottasso et al. (2014)*, with the main purpose being smart blades testing and control applications. Depending on the aim, the scaling process is different.

The objective of this contribution is to introduce a newly constructed model wind turbine with a diameter of 1.8 m, that represents the generic offshore reference wind turbine NREL 5 MW *(Jonkman et al., 2009)*. This includes the scaling process, comparison of aerodynamic loads and forces for reference and the scaled turbine under turbulent inflow, based on aerodynamic simulations, as well as the aerodynamic characterisation in the wind tunnel. The turbine model is aimed for investigations in the area of inflow and rotor aerodynamics, turbulence-turbine interaction and testing of control approaches.

2.2 Scaled wind turbine model and wind tunnel with active grid

2.2.1 Scaling

The scaling approach has the goal of maintaining the design tip speed ratio (TSR) of 7.5 of the reference turbine. Furthermore, the lift distribution over the blade length should be representative of the reference turbine, for all operational TSR. If these aims can be fulfilled, this results in a representative thrust as function of TSR curve and representative blade root bending moments in the flapwise direction, as these quantities are mostly an integration of the lift along the blade span. The turbine diameter should be as large as possible within the limitations of the wind tunnel size to benefit the Reynolds number, as well as to allow for the implementation of sensors and an individual pitch system in the blade root.

The model turbine diameter is chosen to be 1.8 m, on the basis of the target wind tunnel with an open test section and a square nozzle outlet of 3 m by 3 m and experiences with a smaller wind turbine in a smaller wind tunnel with a similar turbine to tunnel ratio (*Schottler et al., 2016*). The NREL 5 MW turbine with a rotor diameter of 126 m *(Jonkman et al., 2009)* is chosen as a reference, because of its prevalence in scientific studies and thus possibility to easily compare findings, as well as the availability of the design.

The rotor diameter is scaled with a length factor n_L according to Eq. (2.1). Due to safety considerations the rated rotational speed is limited to 600 rpm, hence, the time scaling factor n_T is governed by Eq. (2.2).

$$n_L = \frac{D_{scaled}}{D_{reference}} = \frac{1.8\ m}{126\ m} = \frac{1}{70} \tag{2.1}$$

$$n_T = \frac{n_{scaled}}{n_{reference}} = \frac{600\ 1/min}{12.1\ 1/min} = 49.6 \tag{2.2}$$

Based on the length and time scaling factors, the main parameters of the scaled wind turbine are obtained. These are listed in Tab. 2.1 along with the reference values *(Jonkman et al., 2009)* and the specific scaling factor.

Table 2.1: Scaling of main turbine parameters

Rated values	**Factor**	**Reference**	**Scaled**
rotor diameter	n_L	126 m	1.8 m
rotor speed	n_T	12.1 1/min	600 1/min
tip speed	$n_L \cdot n_T$	80 m/s	57 m/s
power	$n_L^5 \cdot n_T^3$	5 MW	363 W
torque	$n_L^5 \cdot n_T^2$	3.95 MNm	5.8 Nm
wind speed	$n_L \cdot n_T$	11.4 m/s	8.1 m/s
thrust	$n_L^4 \cdot n_T^2$	700 kN	72 N
max. chord Reynolds number	$n_L^2 \cdot n_T$	$1.1 * 10^7$	$1.1 * 10^5$

2.2.2 Blade design

The approach to scale the lift distribution for the model turbine is to, in a first step, keep the twist distribution over the non-dimensional radius $\frac{r}{R}$ of the reference turbine. Under the hypothetical assumption, that the profiles of the reference rotor blade have the same lift characteristics as when used in the scaled experiments, a simple geometrical scaling of the blade would be sufficient. However chord based Reynolds numbers are decreased by a factor of 100 due to the scaling process (see Tab. 2.1). The reference profiles would suffer severe separation at this reduced Reynolds number and the lift and drag polars would change significantly.

For the reference blade two representative airfoils are used to describe the aerodynamic properties. These are the DU35 for the root section and the NACA 64618 for the midspan and tip region. These profiles were exchanged with the two low Reynolds number airfoils SG6040 and SG6041 *(Giguere and Selig, 1998)*. The root airfoil SG6041 has a relative thickness ratio of 16 % and is used from 0.2 R to 0.38 R and the midspan and tip airfoil SG6041 has a relative thickness ratio of 10 % and is employed from 0.5 R up to the tip. Between 0.38 R and 0.5 R the profiles are interpolated.

The airfoils were chosen on the basis, that both have their maximum glide ratio (GR) at the angle of attack, that the corresponding reference airfoils have theirs as well. Considering the low operational Reynolds number the maximum GR of these airfoils is comparibly high. A further reason was the high relative thickness of the root airfoil, due to structural considerations. In addition, the SG6041 airfoil was chosen because it is a low lift airfoil, as is explained below.

In Fig. 2.1 a - d the slope of the lift coefficient and glide ratio of the applied low Reynolds number airfoils is plotted together with the corresponding airfoils used on the base turbine *(Jonkman et al., 2009)*. The polars of the low Reynolds number airfoils are estimated with XFoil, with a Reynolds number of $75 \cdot 10^3$ for the SG6040 airfoil and $115 \cdot 10^3$ for the SG6041 airfoil, which represent typical operation at 480 rpm, a N_{crit} value of 7 *(Drela, 1989)* and without forced transition, within the QBlade environment *(Marten et al., 2013)*. The polars of the corresponding airfoils of the reference blade are taken from the FAST turbine model. The lift slope of the tip airfoil SG6041 has an offset to the reference NACA airfoil, because it is a low lift airfoil. To maintain the non dimensional lift, the chord length is extended, based on Eq. (2.3).

$$\frac{C_L(\alpha)\ c(r)}{R} = const. \tag{2.3}$$

The chord is extended for the whole blade, based on the lift offset at the tip airfoil at a design angle of attack of 4°, corresponding to design operating conditions at 0.7 R to 0.9 R and results in a chord enlargement of 31 %. This approach has the benefit of

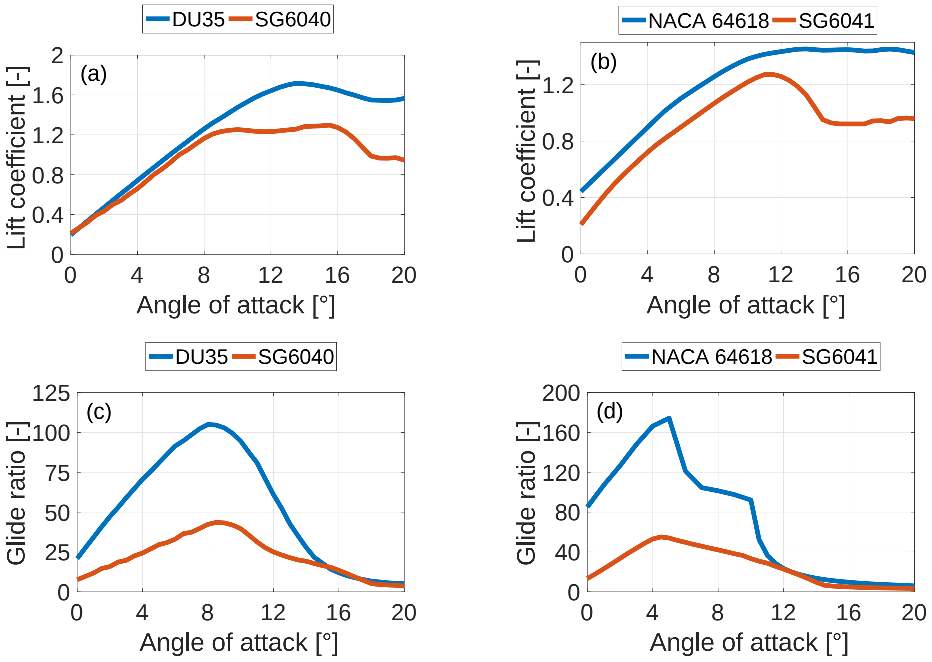

Figure 2.1: Lift coefficient (a) and glide ratio (c) over angle of attack for root airfoils and lift coefficient (b) and glide ratio (d) over angle of attack for tip airfoil.

increasing the chord based Reynolds number along the scaled blade at a maintained design tip speed ratio of 7.5. For the manufacturing of the blade the airfoil shapes have been slightly modified with a constant finite trailing edge thickness (0.5 mm), as well as by increasing the minimum leading edge radius slightly for the tip airfoils ($r_{\text{min}} = 0.5\,\text{mm}$). The requirement for the first eigenfrequency of the blade was to be safely above the 3 P excitation of the rotor, which is at 30 Hz. This was achived by a rotorblade design with a carbon fiber shell and a foam spar, weighing about 160 g per blade and providing a basically rigid blade. At the root the blade is glued on a metal adapter.

2.2.3 Turbine layout

Fig 2.2 a shows the layout of the nacelle and Fig. 2.2 b the assembled turbine. A brushless DC motor, designed for the use in RC airplanes, is used as a generator and converts mechanical rotor to electrical power. The generated electric power is then rectified and disspiated by an electronic load with a nominal power of 400 W. Connected to the generator is a planetary gearbox with a ratio of 1:5. Through a coupling a torque meter, with a nominal torque of 20 Nm, is connected, which also features a dual optical encoder with 360 steps per revolution. With a further coupling the torque meter is connected to the main shaft. This hollow shaft is mounted on two roller bearings with a slip ring with 24 channels in between. Through this slip ring, signals and power are transferred from the stationary nacelle to the rotating rotor hub and vice versa. The wires are layed through a hole in the hollow shaft and bypass so the rotor bearing. On the shaft, a board with five measurement amplifiers is mounted. The amplifiers with an output range of ± 10 V are utilised to amplify the strain gauge signals used to measure flapwise blade bending moments on all blades and shaft bending moments. Full Wheatstone bridges are applied for the strain gauge measurements. Local bending is increased at the places of measurement by means of four symmetrical recesses on the hollow shafts of the blade roots and the main shaft. This way the signal output is increased and the recess openings are used as cable passages. In front of the rotor three motor boards are positioned, which drive the individual pitch motors. The motor boards are controlled with the CANopen protocol, which enables the control of the individual pitch motors with only five cables, including power supply, that have to be passed through the slip ring. The cables are distributed to the single controllers with a distribution board.

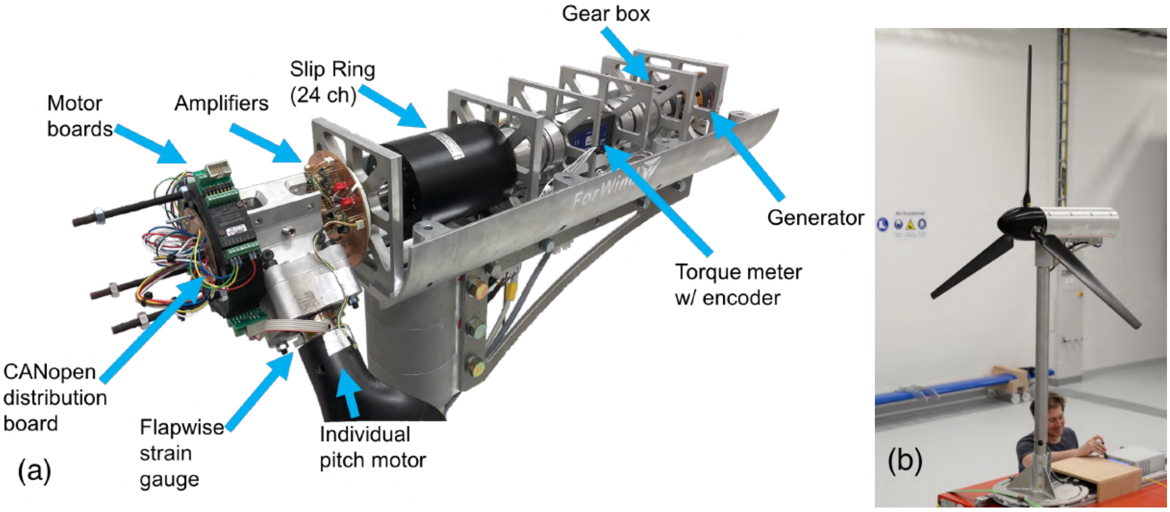

Figure 2.2: (a) Nacelle of model turbine. (b) Turbine.

DC motors with an encoder and a 1:159 planetary gearbox are used for pitching and are positioned within the root of each blade. The pitch system is preloaded with a torsional spring to prevent play in the pitch system. The metal adapter, glued to the composite blades, acts also as the housing for the pitch motor and shaft surface for the pitch bearings.

The turbine nacelle, which is aluminium milled and designed to allow for modular changes of different turbine components, is mounted on a hollow tower. All cables of the nacelle are layed inside the tower. At the tower base there are strain gauges to measure the bending moments in fore-aft and side-side directions. Again, the strain and thus strain gauge output are increased by four symmetrical recesses, which are also used to lead the cables out of the hollow tower. The tower is mounted on a height adjustable support structure. The first eigenfrequency modes in fore-aft and side-side directions are below the excitation of 1 P at 400 rpm.

The control and data acquisition runs on the Real Time System of a Compact RIO PAC system. Analog signals of the strain gauges on the blades, shaft and tower base are recorded synchroniosly, together with optional flow measurements, e.g. with hot wires. The current of the electronic load, which is proportional to the rotor torque, is controlled by 0-10 V output of the PAC system. Further modules for digital signals of the torque sensor encoder, which are processed on the integrated FPGA, and for the CANopen communication are used.

2.2.4 Setup in wind tunnel with active grid

The dimensions of the Göttingen type wind tunnel in the WindLab of ForWind - University of Oldenburg are 3 x 3 x 30 m^3, with maximum wind speeds in the open test section configuration of $32\,\mathrm{ms}^{-1}$. In Fig. 2.3 a, the typical turbine setup in the tunnel is sketched. The turbine is mounted on a height adjustable support to bring the turbine hub to the center of the wind tunnel. The tunnel is operated in an open test section configuration, so that no blockage effects are to be expected *(Ryi et al., 2015)*. The distance between nozzle and rotor plane is 4.8 m, corresponding to $2.7\,D$.

To the nozzle, an active grid can be attached (see Fig. 2.3 b), with which specific turbulent flow patterns can be repeatedly impressed on the flow, as described by Heißelmann et al. for a smaller version of this grid *(Heißelmann et al., 2016)*. These patterns, for example, can be wind characteristics as measured in the free field by Lidar systems, scaled in size and speeded up in time to match the scaling of the model turbine.

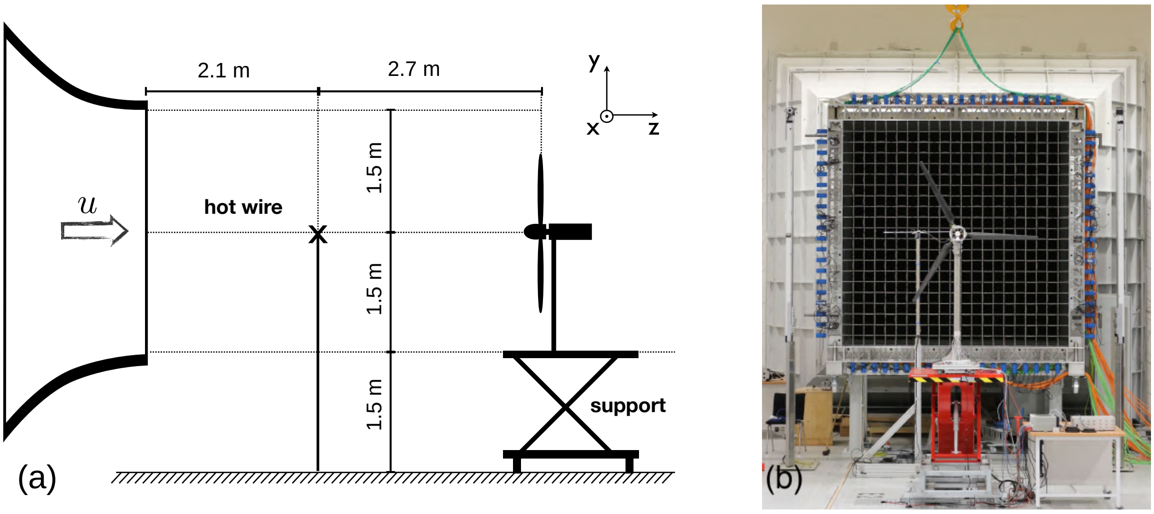

Figure 2.3: (a) Scaled turbine setup in tunnel without grid. (b) Turbine in tunnel with grid.

2.3 Investigations of aerodynamic scaling based on aeroelastic simulations

2.3.1 Simulation setup

A model of the scaled turbine has been set up in FAST v7 *(Jonkman and Buhl, 2005)*. The model includes the aerodynamic shape of the turbine blade which consists of 14 segments. The polars are based on XFoil simulations as described in section 2. The degree of freedom for aerodynamic forces is enabled for the considered simulations, whereas all other structural degrees of freedom are disabled. Furthermore an existing FAST model of the NREL 5 MW turbine is used, also only with the aerodynamic forces degree of freedom enabled and without the originally specified rotor tilt, in order to match the scaled model.

The Beddoes Leishman dynamic stall model and the implemented dynamic inflow model are turned on in the calculation of the aerodynamic forces. The NREL 5 MW turbine spins with a constant rotational velocity of 7 rpm, whereas the scaled model rotates at 490 rpm, that is 70 times the speed of the reference turbine. For the investigation a ten minute turbulent wind seed generated with TurbSim with the IEC Kaimal model is considered. The wind field (class 1A) is created for the NREL 5 MW wind turbine and has a mean wind speed of 6.17 ms^{-1}, turbulence intensity of 23.5 % and a shear layer with a power law exponent of 0.2. Using the same tip speed and upstream mean wind leads to the same mean tip speed ratio of 7.5, which is the design TSR. The ratio of rpm corresponds to the geometric scaling in this numerical investigation in contrast to the prior chapter for the hardware design. The length of the full size turbulence wind box corresponds to simulation time times the mean velocity, which leads to identical number of rotor revolutions. The wind field therefore is compressed in a next step in size by a factor of $\frac{1}{70}$ and the time is speeded up by a factor of 70, thus leading to a time length of the wind field of 8.57 s for the scaled turbine.

2.3.2 Aerodynamic response in turbulent conditions

Both turbines, the reference and the scaled turbine, have been simulated with the described setup and the same number of simulation time steps. The pitch angle of the scaled turbine was set to 1° (in feather direction), as this was identified as the perfect operational point, as described in Sect. 2.4. The output of the scaled turbine model simulation has been scaled back to the size of the 5 MW reference turbine. For a perfect scaling of the rotor blade all time series of aerodynamic forces and angle of attack distributions over the rotor radius, as well as integrated quantities like torque, thrust and flapwise blade bending moment should match.

In Fig. 2.4 scatter plots for the angle of attack variation, as well as the force component normal to the rotor plane, at three blade segments of $0.42R$, $0.67R$ and $0.92R$, are presented. Firstly, a high correlation for both quantities can be seen at all three radii. However, the exchange of the airfoils and enlarging of the chord have an influence. The red lines, representing the best linear fit, depict, that the slope for the angle of attack is quite similar, whereas for the normal forces it is less steep, compared to the x=y function. That means there are slightly overestimated maximum normal forces and also underestimated minimal normal forces, for the scaled turbine. The main reason is, that the chord scaling was based on the design angle of attack at a radius of $0.7\ R$ to $0.9\ R$. For operation off these conditions the chord scaling factor of 1.31 does not fit perfectly.

In Fig. 2.5 scatter plots for thrust, torque and blade bending moment in flapwise direction are presented. For these quantities, that represent an integration of the aerodynamic forces, again a good correlation is found, especially for thrust and torque. For the thrust and bending moment, the same trend as for the normal forces is visible, which is expected, since the forces normal to the rotor plane are the underlying forces for these quantities. For the torque, the values for the reference turbine are in general slightly higher. The main reason for this is that the glide ratios of the profiles used for the scaled blade are at least lower by a magnitude of two.

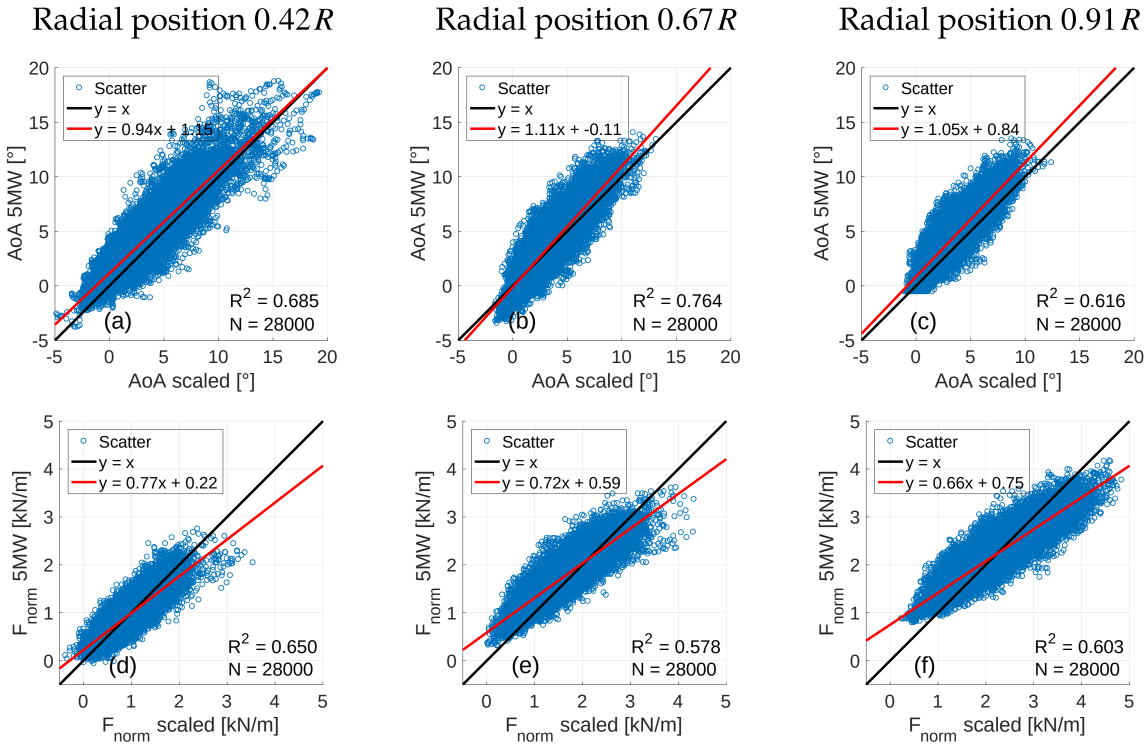

Figure 2.4: Aerodynamic simulations: Scatter of angle of attack (a-c) and and force normal to the rotor plane (d-f) for radial positions of $0.42\,R$, $0.67\,R$ and $0.91\,R$.

2.4 Wind tunnel experiments

The setup in the wind tunnel is sketched in Fig. 2.3. At the hot wire position, 1.5 D in front of the turbine where the flow is not yet disturbed by the rotor, an array of three hot wires is placed. One is on the center line and the two others are at 0.4 m in positive and negative x-direction. As a reference longitudinal velocity the mean value of these three hot wires is taken. Torque and revolutions are measured with the torque meter. The thrust is derived from the measured tower base bending moment in fore-aft direction. The characterisation curves are recorded at a constant rotational velocity and the wind velocity is adjusted to achieve different tip speed ratios. With this approach, the chord based Reynolds number does not change significantly along the radius, since the rotational velocity component is the main contributor.

2.4.1 Aerodynamic characterisation

For the aerodynamic characterisation, the rotational velocity is kept constant at 480 rpm with a PI controller. For every operational state average values of power coefficient (C_P) and thrust coefficient (C_T) are computed over five second periods. In Fig. 2.6 a

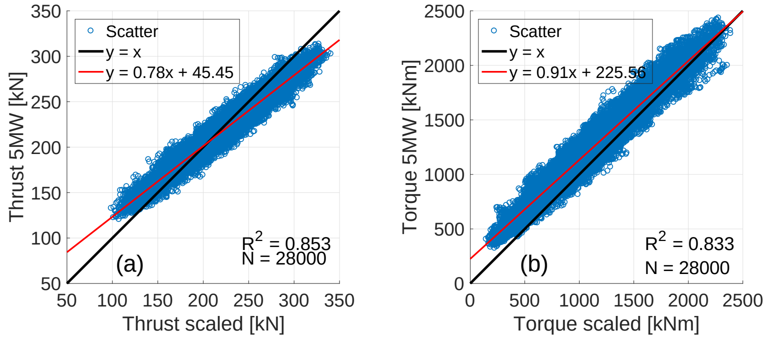

Figure 2.5: Aerodynamic simulations: Scatter of thrust (a), torque (b) and flapwise blade root bending moment (Myb) (c)

contour plot of C_P based on 56 measured operational states is presented. The tip speed ratio is varied from 5.5 to 9 with a step size of 0.5 and the pitch angle is changed from minus two (towards stall) to four (towards feather) in steps of one degree. The turbine performance at a pitch angle of one is the best. The optimal tip speed ratio is in the range between 7 and 8.

In Fig. 2.6 b the thrust coefficient for the same experimental matrix is presented. For a pitch angle of one degree and tip speed ratios of 7 and 7.5, C_T is close to a value of the optimal thrust coefficient of $\frac{8}{9}$. The here given thrust coefficients are based on the tower bottom bending moment inf fore-aft direction and are corrected for the tower and nacelle drag, which was measured on the structure without the blades attached.

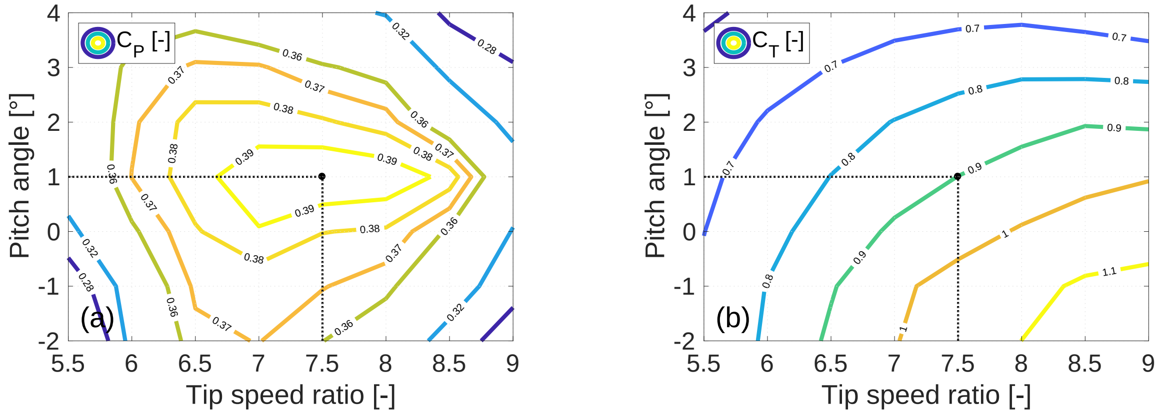

Figure 2.6: Contour plot of power coefficient (a) and thrust coefficien (b) for different tip speed ratios and pitch angles.

The power coefficient as a function of the tip speed ratio for a pitch angle of one degree is plotted in Fig. 2.7 a and compared to numerical results for the NREL 5 MW turbine obtained with the FAST model described in Sect. 2.3. The error bars indicate the influence of an error of ± $0.1\ \mathrm{ms}^{-1}$ in the measurement of the reference velocity, which is considered a conservative margin of uncertainty for the hot wire measurements. When increasing TSR, this uncertainty rises as well, since the wind velocity is decreased at constant rotational speed. The power coefficient shows a good match to the general slope over TSR, with the power coefficient peaking at a TSR of 7.5. For the offset between the curves, at least two reasons play a significant role. Firstly, the glide ratio of the profiles used for the scaled turbine are lower by a factor of at least two in comparison to the reference turbine. Secondly, in the experiment, the power is measured by the torque meter. Between this device and the rotor there are mechanical losses in the bearings of the main shaft and the slip ring contact, that have not been accounted for.

In Fig. 2.7 b, the thrust coefficient is plotted as a function of the tip speed ratio, again in comparison to the reference turbine. The experiment fits the reference in slope and also in absolute values.

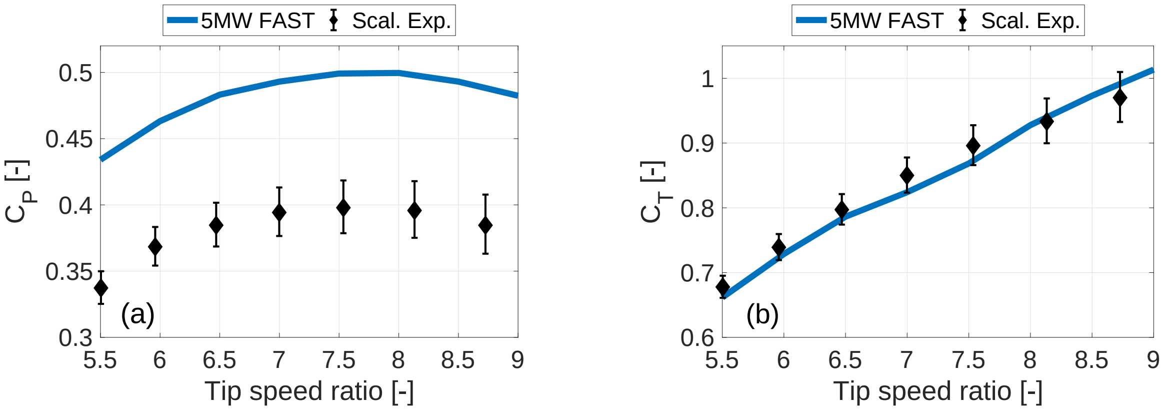

Figure 2.7: (a) C_P over TSR at 480 rpm and 1° pitch compared to the reference turbine. (b) C_T over TSR at 480 rpm and 1° pitch compared to the reference turbine.

2.4.2 Influence of Reynolds number

In some experiments, especially in turbulent flow with a controller, the rotational velocity is not constant. The main operational window of the turbine is in the range of 400 rpm to 600 rpm. Chord based Reynolds numbers for the profiles range from $50 \cdot 10^3$ at the root to a maximum of $100 \cdot 10^3$ for operation at 400 rpm and from $70 \cdot 10^3$ to $140 \cdot 10^3$ for operation at 560 rpm.

For the three settings of 400, 480 and 560 rpm and the optimal pitch setting of 1°, the power coefficient and the thrust coefficient over tip speed ratio have been recorded and are plotted in Fig. 2.8 a and b, respectively. For the 560 rpm case not all tip speed ratio configurations are available, since these measurements would have exceeded the design loads of the machine. For the 400 and 480 rpm operating points the maximum C_P is at a TSR of 7.5 and the slope for higher TSR matches, whereas the maximum for the 560 rpm opearting points is slightly shifted to the lower TSR of 7. For tip speed ratios of 8 to 9 the operating measurements at the higher rpm values of 480 and 560 match with, whereas the measurements at 400 rpm show a faster decline in power coefficient. The thrust coefficient for all situations match, however at TSR higher than 8, again, the case with 400 rpm shows slightly lower values. This decline can be attributed to the change in Reynolds number and is due to a distinct flow over the blade. Laminar separation or a separation bubble on a blade section, due to the decreased Reynolds number, are a possible explanation, however not provable with the available data.

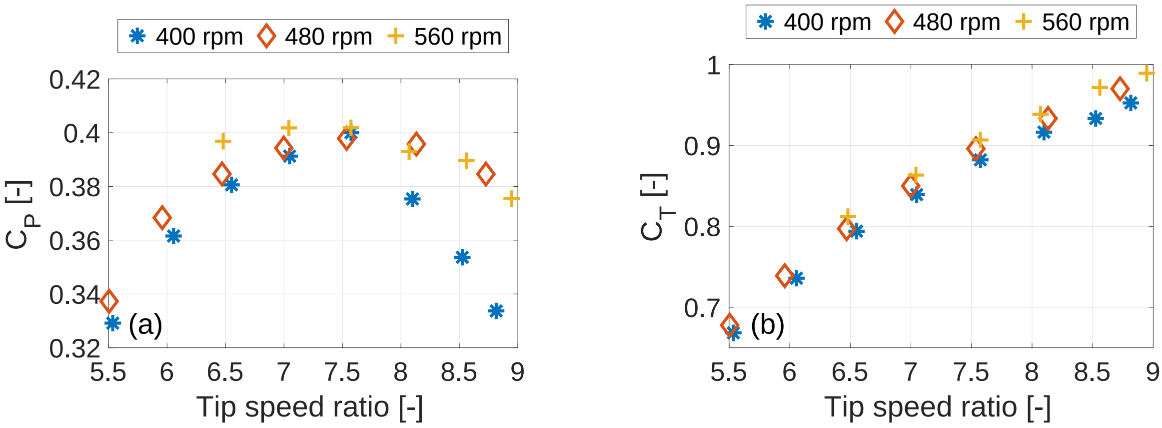

Figure 2.8: (a) C_P over TSR at different angular rotor velocity and 1° pitch. (b) C_T over TSR at different angular rotor velocity and 1° pitch.

2.5 Conclusions

A scaled wind turbine model, based on a 5 MW reference turbine, has been introduced. This includes the scaling process, design of the blades, hardware introduction of the machine and setup in the wind tunnel. Aerodynamic forces and loads of the scaled turbine were compared to the reference turbine under turbulent inflow and in an aerodynamic simulation environment. These simulations were performed in preparation of experimental measurements in tailored turbulent inflow conditions. Furthermore the aerodynamic characterisation measurements obtained with the turbine in the wind tunnel were presented. The following conclusions can be drawn from the investigations in this paper:

- Based on the aerodynamic simulations it is presented, that the scaled turbine model maps the thrust, torque and flapwise blade bending characteristics, but also the normal forces and angle of attack variation at different blade segments of the reference turbine.
- In the experiments, the machine reaches the maximum power coefficient of 0.4 at the design tip speed ratio and shows a match of the general slope for power coefficient and a good fit for the thrust characteristic in comparison to the numerical results of the reference turbine.
- The power coefficient and thrust coefficient slope, for operation at different rotor speeds and thus chord Reynolds numbers, depict a good match, apart from slight deviations for the case with the lowest rotational speed at high tip speed ratios.
- The approach for enlarging the chord and thus the Reynolds number by 31 % by applying low lift profiles without changing the design tip speed ratio proves useful, especially considering, that at 400 rpm first indication of the influence of the decreasing Reynolds number are visible.

Acknowledgment

This work is partly funded by the Federal Ministry for Economic Affairs and Energy according to a resolution by the German Federal Parliament (Smart Blades 2.0 0324032D) and by the Ministry for Science and Culture of Lower Saxony through the funding initiative Niedersächsisches Vorab (project ventus efficiens). We further thank the mechanical and electrical workshops of our institute for the help in realising MoWiTO 1.8 (Model Wind Turbine Oldenburg 1.8 m).

Chapter 3

Experimental analysis of radially resolved dynamic inflow effects due to pitch steps

The content of this chapter is identical to:

Berger, Frederik, David Onnen, Gerard Schepers and Martin Kühn (2021). 'Experimental analysis of radially resolved dynamic inflow effects due to pitch steps'. In: *Wind Energy Science* 6.6, pp. 1341–1361. `DOI: 10.5194/wes-6-1341-2021`.

Abstract

The dynamic inflow effect denotes the unsteady aerodynamic response to fast changes in rotor loading due to a gradual adaption of the wake. This does lead to load overshoots. The objective of the paper was to increase the understanding of that effect based on pitch step experiments on a 1.8 m diameter model wind turbine, which are performed in the large open jet wind tunnel of ForWind – University of Oldenburg. The flow in the rotor plane is measured with a 2D laser Doppler anemometer, and the dynamic wake induction factor transients in axial and tangential direction are extracted. Further, integral load measurements with strain gauges and hot-wire measurements in the near and close far wake are performed. The results show a clear gradual decay of the axial induction factors after a pitch step, giving the first direct experimental evidence of

dynamic inflow due to pitch steps. Two engineering models are fitted to the induction factor transients to further investigate the relevant time constants of the dynamic inflow process. The radial dependency of the axial induction time constants as well as the dependency on the pitch direction is discussed. It is confirmed that the nature of the dynamic inflow decay is better described by two rather than only one time constant. The dynamic changes in wake radius are connected to the radial dependency of the axial induction transients. In conclusion, the comparative discussion of inductions, wake deployment and loads facilitate an improved physical understanding of the dynamic inflow process for wind turbines. Furthermore, these measurements provide a new detailed validation case for dynamic inflow models and other types of simulations.

3.1 Introduction

Dynamic inflow describes the unsteady response of loads to fast changes in rotor loading, e.g. due to fast pitching of the rotor blades or gusts. This unsteady aerodynamic effect leads to load overshoots due to the inertia of the global flow field, as the axial wake induction in the rotor plane cannot change instantaneously but only gradually to a new equilibrium flow field.

In addition to the direct impact on the dynamic loading, *Van Engelen and Van Der Hooft (2004)* emphasise the need to model these dynamic inflow effects for the pitch controller design to enhance the stability and thus reduce unnecessary fatigue loads with optimised pitching transients, especially near rated operation. The dynamic wake behaviour due to load changes is intrinsically considered in higher-fidelity approaches as computational fluid dynamics (CFD) and free vortex wake method (FVWM) simulations, thus modelling the dynamic inflow effect. However, engineering models are required to mimic this effect in blade element momentum (BEM) theory, which is commonly applied for aeroelastic simulations for the design and certification of wind turbines. Well-tuned engineering models help to avoid too conservative predictions of fatigue loads.

First extensive studies in the 1990s within the Joule I and II projects on the development of dynamic inflow models for wind turbines are described in *Snel and Schepers (1994)* and *Schepers and Snel (1995)*. There the free field measurements of out-of-plane blade root bending moment and rotor shaft torque for pitch steps on the 2 MW Tjæreborg wind turbine, described in *Øye (1991)*, are used for validation.

Later *Schepers (2007)* employed a one-time-constant model to analyse force transients. These are derived from pressure sensor arrays at five radial stations, after the pitch steps of the NREL (National Renewable Energy Laboratory) phase VI turbine with 10 m diameter (see *Hand et al., 2001*) in the NASA Ames wind tunnel. Forces for the pitch step to low load adapt faster to the new equilibrium than for the step to high load. They could not experimentally validate the strong radial dependency of the time constant, which they expect from cylindrical wake models. *Sørensen and Madsen (2006)* also investigated the same experiment and compared it to unsteady Reynolds-averaged Navier–Stokes (uRANS) CFD simulations. They suggest using a two-time-constant model to capture the dynamic inflow effect on the forces. The fast time constant represents the near-wake dynamics and decreases with radius, and the slow time constant represents the far-wake dynamics. Later *Pirrung and Madsen (2018)* investigated this experiment and uRANS CFD simulations again and compared them to a cylindrical wake model. Based on varying the wake length in the cylindrical wake model, they affirm that two different time constants best describe the dynamic inflow effect.

Within the Model EXperiment In controlled COnditions (MEXICO) framework, pitch steps are performed on a 4.5 m diameter model wind turbine, featuring pressure distribution measurements at five radial stations, as well as in high- and mid-fidelity simulations *(Boorsma et al., 2018)*. They find that unsteady aerodynamic effects on the blade chord level, namely the Theodorsen effect, reduce the load overshoot. This effect can be modelled as a time lag on the angle of attack of the order of the ratio of relative wind to respective chord length. In contrast, the typical dynamic inflow time constant is of the order of the ratio of radius to free wind velocity and 2 orders of magnitude higher.

Yu et al. (2017) used an actuator disc with variable blockage in a wind tunnel to study the wake evolution after a change in thrust. We also presented a preliminary pitch step experiment in *Berger and Kühn (2018)*, focusing on the integral turbine loads. The relevance of improved modelling of the dynamic inflow effect can be seen in the recent development of new dynamic inflow models by *Yu et al. (2019)*, *Madsen et al. (2020)* and *Ferreira et al. (2022)*.

Schepers and Schreck (2018) emphasise the value of experimental investigations of aerodynamic effects and also specifically the dynamic inflow effect to further improve and validate models. Higher-fidelity simulations depend on calibration and thus cannot solely fill this gap. Further, *Schepers and Schreck (2018)* outline the importance of radius-resolved aerodynamic measurements over integrated blade and rotor loads. No experimental investigation is available until now, where the wake induction is directly probed at various blade radii in the rotor plane.

The objective of this paper is to get deeper insights into the dynamic inflow effect for wind turbines due to pitch steps. The main novelty in this work is the dynamic induction measurement. The radial dependency and differences between the pitch directions are investigated using time constant analysis. Furthermore, the behaviour of the flow in the near and close far wake and integral loads are used to compare the differences between the pitch directions. These different measurements are contemplated together to allow for new insights into the dynamic inflow effect, test presumptions and validate findings of prior work.

3.2 Methods

In Sect. 3.2.1 the experiment is introduced. In Sect. 3.2.2 time constant models and the fitting approach are outlined. Lastly, in Sect. 3.2.3 the method for the load reconstruction based on the obtained wake inductions is outlined.

3.2.1 Experiment

In this subsection, all relevant information on the experiment is introduced, consisting of the setup, experimental matrix, wake induction derivation from measurements, ensemble averaging approach and correction models.

Setup

The experiments were performed in the large wind tunnel at ForWind – University of Oldenburg. It is a Göttingen-type wind tunnel that can be operated in an open jet or a closed test section configuration. The test section length measures 30 m, and the rectangular wind tunnel nozzle dimensions of 3 m by 3 m, as shown in Fig. 3.1 a. Wind velocities in the open jet configuration reach up to 32 m s^{-1}. *Kröger et al. (2018)* provide detailed information about the wind tunnel and the optional active grid. No active grid was used in the measurement, and the turbulence intensity of the inflow was of the order of 0.3 %.

The utilised Model Wind Turbine Oldenburg has a diameter of 1.8 m (MoWiTO 1.8). The machine is an aerodynamically scaled version of the NREL 5 MW generic turbine *(Jonkman et al., 2009)* with a length scaling factor of $n_{\text{length}} = \frac{1}{70}$. The scaling approach was to maintain the design tip speed ratio, thrust and power characteristic, as well as non-dimensional lift and thus axial induction distribution for the operational range. Low Reynolds number airfoils were used. The rotor blades have a stiff carbon-fibre-based

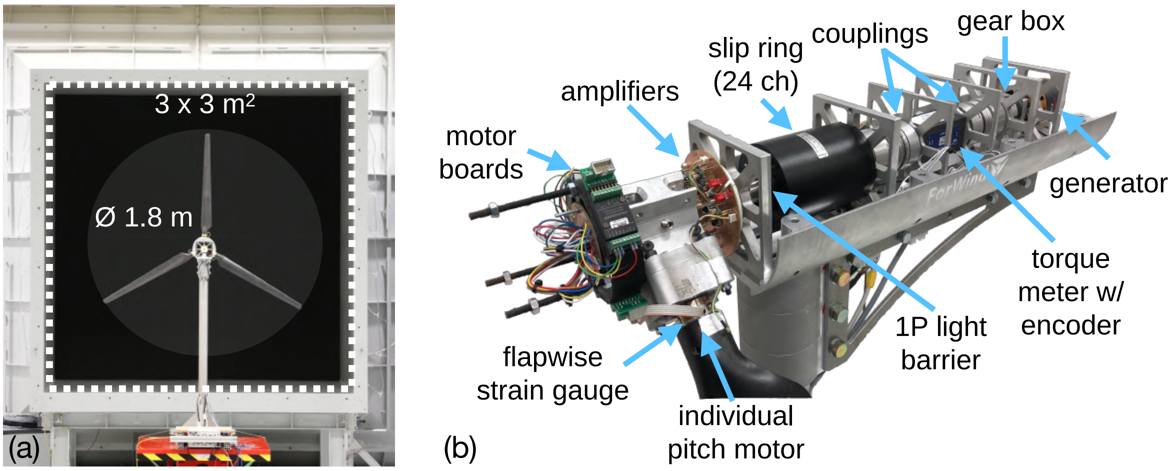

Figure 3.1: (a) Wind tunnel nozzle and MoWiTO 1.8 with main dimension. (b) MoWiTO 1.8 with open nacelle.

structure with the first eigenfrequency of 32 Hz and estimated maximum tip deflections of 0.01 m The scaling approach and turbine are described in detail in *Berger et al. (2018)*. The blockage ratio of the turbine in the used open jet configuration wind tunnel is 0.28; however, *Ryi et al. (2015)* showed that blockage effects are negligible for such an open jet configuration.

The MoWiTO 1.8 nacelle is shown in Fig. 3.1b. The turbine features individual pitch motors, which are mounted in the root of each blade. The pitch motors are small DC motors with a three-stage planetary gearbox with a gear ratio of 159 : 1 and integrated encoders. They are mounted and pretensioned with springs to counteract gear backlashes and thus allow for setting precise pitch angles. Pitching speeds up to 100 Hz (1.75 rad s^{-1}) can be achieved. The main shaft is supported by two roller bearings and connected by a coupling to a torque meter with an integrated encoder and through another coupling and one stage planetary gearbox to the generator. Flapwise blade root bending moments for each blade are measured by a full Wheatstone bridge strain gauge configuration on the metal adapter; the carbon-fibre blades are glued on. The power supply lines for the amplifiers and motor boards in the hub and their communication with the control hardware are channelled through a slip ring from the rotating hub to the stationary nacelle. Further, the thrust of the turbine is derived from a strain gauge measurement of the tower bottom bending in fore–aft direction, as outlined in Sect. 3.2.1. A National Instruments Compact Rio is used for control and data acquisition. Analogue data (e.g. strain gauges, external hot wires) are sampled at 5 kHz, and the control loop and pitch motor communication run at 100 Hz.

The setup of the MoWiTO 1.8 in the wind tunnel is sketched in Fig. 3.2a and b as a view from the side and top respectively. The wind speed is obtained by the measured pressure drop in the wind tunnel nozzle. The turbine is positioned 2.6 diameter (D) behind the wind tunnel nozzle, so the induction zone of the turbine is not influenced (see *Medici et al., 2011*).

Integral loads of flapwise blade root bending moment (M_{flap}), rotor thrust (F_{thrust}) and rotor torque (M_{aero}) are obtained based on strain gauge measurements shown in blue in the sketch.

Hot-wire measurements in the near wake (up to $1\,D$ according to *Vermeer et al., 2003*) and beginning far wake (more than $1\,D$) are performed at hub height. In flow direction (x axis), seven distances ranging from 0.5 to $2\,D$ behind the turbine are considered in steps of $0.25\,D$ and shown in red in the sketch. In radial direction (negative y axis), values between the rotor axis at 0 radii (R) to $1.4\,R$ in steps of $0.2\,R$ are considered. This adds up to 56 measurement positions.

In the rotor plane, laser Doppler anemometer (LDA) measurements are performed with a 2D system by TSI Inc. A beam expander with a focus length of 2.1 m is used to not disturb the flow. Both lasers have a maximum power of 1 W. The LDA probe is mounted on a three-axis traverse system and can be driven by 1.5 m in each direction by motor. Measurement points are in the rotor plane at hub height. They are positioned radially (negative y axis) from 0.25 to $0.95\,R$ with steps of $0.1\,R$ between 0.3 and $0.9\,R$ and the smaller extra steps at the edges of the range. The LDA measurement is indicated in green in the sketch, and the colour coding for the three signal types, strain gauge, hot wire and LDA, is maintained for all plots in this paper.

Experimental matrix

The turbine is operated at a rotational speed of 480 rpm and wind velocity of $6.1\,\mathrm{m\,s^{-1}}$. This corresponds to a tip speed of $45\,\mathrm{m\,s^{-1}}$ and a tip speed ratio of 7.4. Chord-based Reynolds numbers range from a minimum value of 60×10^3 at the first airfoil at $0.2\,R$ to values between 100×10^3 and 120×10^3 from $0.5\,R$ to the tip. Time constants in dynamic inflow models are related to a reference time constant $\tau_{\mathrm{ref}} = R/u_0$ (see *Schepers, 2012*). This amounts to 0.15 s here.

The rotor blades are collectively pitched by 5.9° between -0.9 and 5.0°, within 0.070 s, corresponding to about half a rotor revolution and half the reference time. The pitch step is from a low rotor load at a thrust coefficient $C_{\mathrm{T}} = 0.48$ to a high load at $C_{\mathrm{T}} = 0.90$ and vice versa, based on the strain-gauge-derived thrust. This corresponds to rotor effective inductions of $a_{\mathrm{eff}} = 0.14$ and $a_{\mathrm{eff}} = 0.34$ respectively, based on the momentum theory relation ($C_{\mathrm{T}} = 4a(1-a)$).

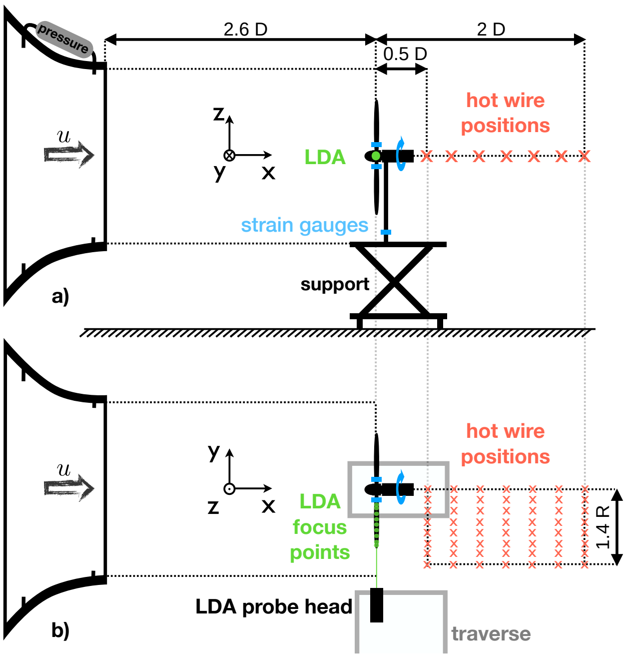

Figure 3.2: Sketch of the setup in the wind tunnel. View from (a) the side and (b) the top.

The representative encoder reading of one pitch motor is plotted in Fig. 3.3. Between the pitch steps, there are 3 s (24 revolutions) to allow for the flow to reach an equilibrium again. There is a slight overshoot of the pitch angle for both pitch directions by one encoder step (0.18°), which due to the small value has no noticeable effect on our investigation.

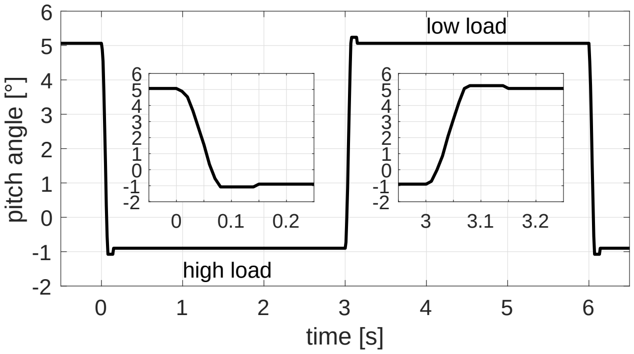

Figure 3.3: Pitch motor encoder signal for a pitch step to high load followed by a step to low load with additional zoomed in views of the actual pitch steps.

For the LDA measurements, 100 pitch steps were performed for each radial position and pitch direction at a typical sampling frequency of 600 Hz. This sampling frequency is just an order of magnitude estimate, since it depends on many parameters, especially the seeding of tiny oil droplets in the wind tunnel and thus varies constantly. Load measurements are taken during the LDA measurements. Therefore, load signals for 900 pitch steps are available. The hot-wire measurements have been performed separately. A wake rake consisting of four hot wires was used to measure at the described 56 positions in the wake. Thus, the experiment, consisting of 25 pitch steps, had to be performed $56/4 = 14$ times, and the wake rake was moved between those measurements.

Wake induction measurement by 2D LDA

The wake induction is derived from the LDA measurements by a method introduced by *Herráez et al. (2018)* for steady operation. The method uses the local velocity in the rotor plane, free of the influence of the bound circulation. This velocity is obtained by probing in the bisectrix of two rotor blades for axial and uniform inflow. In the bisectrix, the blade induction is counterbalanced and thus cancelled out.

In Fig. 3.4a the MoWiTO turbine is shown with the LDA laser beams and the probed axial (u_{ax}) and tangential (u_{ta}) velocity components at a specific radius. Alongside, in Fig. 3.4b, the concept of the counterbalancing of the bound circulation of the evenly loaded blades is sketched. For the shown position, the blade at the 9 o'clock position has no influence on the axial velocity on the indicated line of measurements. At that line, the downwash of the blade ahead of the indicated line counteracts the upwash of the blade behind it, and they cancel each other. The velocity at the line thus is only influenced by the wake induction. *Herráez et al. (2018)* argue that the trailed vorticity, especially at the tip, might play a non-negligible role, as it cannot be captured well at the high distance between the measurement position and the blade tip. Therefore, the method is less suited for the root and tip region of the blade.

Two constraints defined the line of LDA measurements. The first is the height range of the LDA probe head, which is from tower bottom to hub height. The second is to minimise the influence of the tower on the blade nearest to the tower for the measurements in the bisectrix of two blades. This led to a measurement line at the 3 o'clock position. The tower does disturb the axial symmetry, however, based on an estimation of the tower effect with a dipole model as in *Schepers (2012)* the tower effect on the 5 o'clock blade position is considered negligible.

To obtain the values in the bisectrix, the LDA system is synchronised with the MoWiTO data acquisition system. Measurements at the constant high load are plotted for one position of the axial and tangential probe over the azimuth angle ϕ_1 of the turbine in Fig. 3.5. The bisectrix values that are in a threshold of $\pm 3^{\circ}$ are marked in red. These threshold values were identified to give a good compromise between data points and data quality.

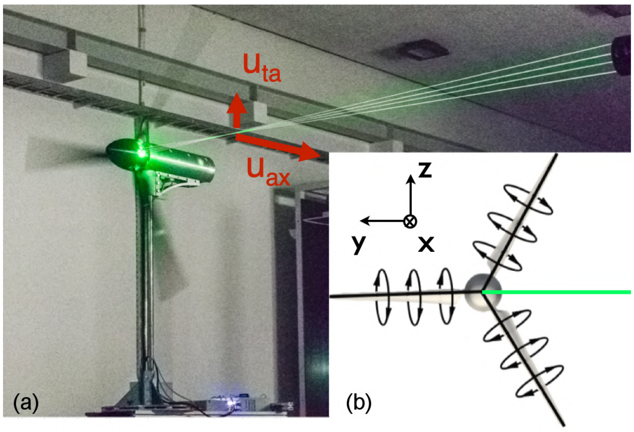

Figure 3.4: (a) Clockwise rotating MoWiTO 1.8 with 2D-LDA probing axial u_{ax} (along x-axis) and tangential u_{ta} (along z-axis) velocity components in the bisectrix of two blades. (b) Scheme of counterbalancing bound circulation of the evenly loaded blades of front view of clockwise rotating rotor. The LDA measurement line is indicated in green (adapted from *Herráez et al., 2018*).

In Fig. 3.5a the analytical course seen by the axial probe according to *Herráez et al. (2018)* (see Appendix 3.5) is presented and shows a good match to the measured signal. This good fit gives a high level of confidence to the applicability of the method to this experiment. For the tangential probe, data are missing around $-1.3\,\mathrm{m\,s^{-1}}$ and also at $2.3\,\mathrm{m\,s^{-1}}$ for the axial probe, which is due to the prototype status of the LDA software at that point in time. We were aware of this bug, and it has no influence on the presented measurements.

Based on these measured axial and tangential velocities, the undisturbed inflow velocity u_0 and the angular velocity Ω and the axial (a) and tangential (a') wake induction factors are defined by Eqs. (3.1) and (3.2). With the geometrical angle γ between the chord of the local blade segment and the rotor plane, consisting of twist and pitch, the angle of attack, α, can be calculated by Eq. (3.3).

$$a = 1 - \frac{u_{\mathrm{ax}}}{u_0}, \tag{3.1}$$

$$a' = \frac{u_{\mathrm{ta}}}{\Omega r}, \tag{3.2}$$

$$\alpha = \arctan\left(\frac{u_{\mathrm{ax}}}{u_{\mathrm{tan}} + \Omega r}\right) - \gamma. \tag{3.3}$$

The method was validated based on particle image velocimetry (PIV) measurements and CFD calculations of the MEXICO rotor by *Herráez et al. (2018)* for steady operation. They found a good performance of the method from $0.3\,R$ up to $0.9\,R$. In *Rahimi et al.*

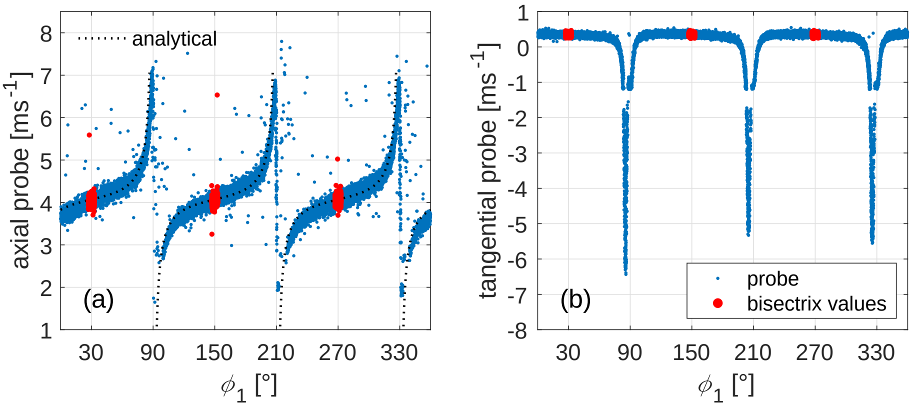

Figure 3.5: (a) Measurements of axial probe for high load case at a radius of $0.7\,R$ for 400 revolutions over azimuth angle ϕ_1 with marked data within the bisectrix threshold. $\phi_1 = 0°$ relates to the 12 o'clock position of blade 1. (b) Analogously for the tangential probe.

(2018), the model was further compared to alternative approaches applied to CFD simulations. Based on these comparisons and the specific focus on the dynamic change of inductions, rather than the total values, the agreement at the root radius at $0.25\,R$ and the tip radius at $0.95\,R$ is considered still reasonably good. Therefore, it is decided to include these radii in this analysis. However, they should be treated with care.

Ensemble averaging

Ensemble averages are used for the LDA data, hot-wire and strain gauge measurements. The data of many repetitions are aligned, triggered by the pitch command. An average value at each time step is constructed out of this data, for the time span -0.5 to 3 s, with the pitch step starting at 0 s. For example, the ensemble average of the flapwise blade root bending moment M_{flap} is given by Eq. (3.4), with the counter of cycles n, total cycles N and the time t.

$$M_{\mathrm{flap}}(t) = \frac{1}{N}\sum_{n=1}^{N} M^{(n)}_{\mathrm{flap,\,single\,cycle}}(t) \tag{3.4}$$

This approach can smooth out non-deterministic variations and also structural interactions. In Fig. 3.6a, the flapwise blade root bending moment for the step to low load is shown for single cycles and the ensemble average. As the pitch step is not aligned with the rotor position, the effect of the tower shadow, seen for the single cycles, is smoothed out for the ensemble average. The high number of 900 repetitions, due to the nine different LDA positions with 100 pitch steps each, leads to a very small 95 %

confidence interval (CI), which would barely be visible in the plots; therefore, is not shown here or later load-related plots.

The induction factors have no fixed sampling frequency, as, firstly, the underlying LDA measurements are non-equidistant and, secondly, only values within the bisectrix of two blades are considered. To construct a single ensemble average out of this data, the 100 repetitions per LDA position are sorted to one signal, and a smoothing approach based on local regression and a weighted least squares and first-order polynomial model is used. For the local regression, 1 % of the data (length of the total dataset is 4.5 s) are used, whereas outliers get weight penalties and are not considered for more than 6 standard deviations. This filter is implemented as “rlowess” within MATLAB 2019b. These smoothed ensembled LDA-based data are resampled to 1 kHz, reducing the original non-equidistant data points by a factor of about 3. The sorted data points along the smoothed resampled signal and 95 % CI for the axial rotor plane (rp) velocity at 0.7 R for the step to low load are shown in Fig. 3.6b.

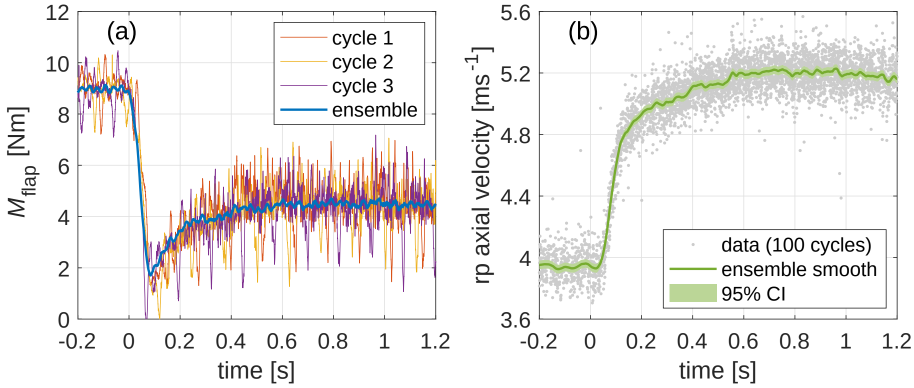

Figure 3.6: (a) Single cycles and ensemble average of flapwise blade root bending moment M_{flap}. (b) Data points and smoothed ensemble average for axial rotor plane (rp) velocity in bisectrix of blades.

Corrections

Steady corrections are applied to the thrust and torque signals. For the torque, the mechanical torque is measured at the torque meter. To obtain the aerodynamic rotor torque, the friction in the bearings and the slip ring was calibrated by running the drivetrain without blades with the motor, used as a generator in operation; thus, the friction was measured with the torque meter. A linear function of the angular rotor speed was obtained and the respective value added to the signal.

The rotor thrust is derived from the tower bottom bending moment in fore–aft direction. The strain gauge was calibrated using defined forces in the thrust direction applied to the nacelle at the height of the rotor axis. The tower and nacelle drag was experimentally calibrated with the turbine without blades and was subtracted from the signal. The free stream velocity (u_0) was used for this correction rather than a corrected wind velocity. This does lead to a small underprediction of the thrust. This error, however, is smaller as if no correction would be applied. In contrast to a dynamically corrected rotor plane wind velocity, this correction is a fixed value that does not influence the main shape of the dynamic load transient.

Dynamic corrections were considered for the torque and thrust signal. Directly after the pitch step, the torque control cannot keep the rotor speed completely steady, so there was a minor deviation of a maximum of 2 % of the rotor speed. Equation (3.5) is used to correct the torque by the contribution ΔM associated to the angular acceleration $\dot{\Omega}$, where I_{rot} is the equivalent rotational inertia of the rotor and drivetrain.

$$\Delta M(t) = I_{\text{rot}} \cdot \dot{\Omega}(t) \tag{3.5}$$

After the pitch step, there is an oscillation of the tower, which is seen in the tower bottom bending moment. The eigenfrequency of the tower and the damping constant of the oscillation is estimated iteratively and thus the measurement signal is corrected to obtain the aerodynamic thrust. The signals without the dynamic correction will also be shown in the results section as a reference (see Fig. 3.19).

3.2.2 Time constant analysis

The decay process after the pitch step is investigated in terms of time constant analysis. Firstly, a one-component time constant model (1c), like that used by *Schepers and Snel (1995)*, is applied, given by Eq. (3.6) for the arbitrary signal S.

$$S(t) = S_{t_0} - \Delta S \cdot \left(1 - \exp\left(\frac{(t_0 - t)}{\tau_{\text{single}}}\right)\right) \tag{3.6}$$

In Fig. 3.7a, the fitting approach is outlined for an exponential transition to a higher value without an overshoot, representing the behaviour that is expected from an induction transient. Figure 3.7b shows a signal with an overshoot and subsequent exponential decay to the new steady level. This represents the behaviour expected from a load. The fit starts when the pitch step is terminated at $t_0 = 0.070\,\text{s}$ at the signal value S_{t_0}. The new steady level after the pitch step is S_1, being the mean value from $t = 2\,\text{s}$ to $t = 3\,\text{s}$. The difference ΔS is given by $S_{t_0} - S_1$ and also contains the information on the direction. The time constant τ_{single} is fitted by means of the least root mean square error for the fitting range between $t_0 = 0.070\,\text{s}$ and $t_{\text{fit}} = 0.80\,\text{s}$.

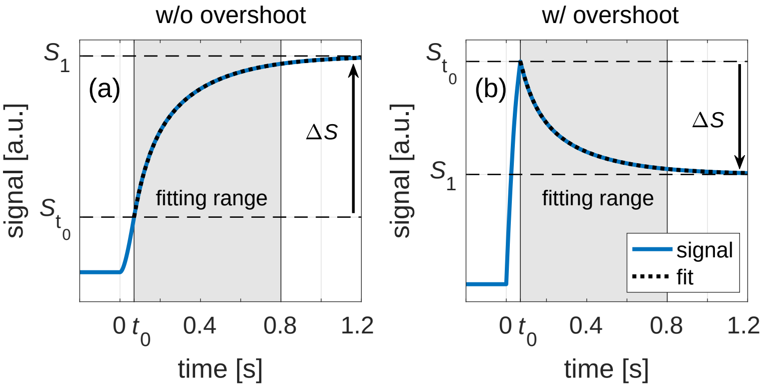

Figure 3.7: (a) Time constant fitting scheme for a signal with exponential decay behaviour without an overshoot. (b) Analogously for a signal with an overshoot.

Secondly, a model with two time constants (2c) similar to *Sørensen and Madsen (2006)* is used. The fitting model is given by Eq. (3.7). The fitting procedure is according to the single-time-constant model. However, three values are fitted: a fast time constant τ_{fast}, a slow time constant τ_{slow} and the weighting factor k of each exponential decay function, associated with the two time constants.

$$S(t) = S_{t_0} - \Delta S \cdot \left((1-k) \cdot \left(1 - \exp \frac{(t_0 - t)}{\tau_{fast}} \right) + k \cdot \left(1 - \exp \frac{(t_0 - t)}{\tau_{slow}} \right) \right) \tag{3.7}$$

These time constants can be used for comparison and tuning of the time constants in the dynamic inflow engineering models of Øye (see *Snel and Schepers, 1994*), used in OpenFAST and GH Bladed, and the new DTU model (see *Madsen et al., 2020*), used in HAWC2. The time constants of these engineering models are derived from simulations and parameterised to the turbine size and operational conditions considering the relevant dynamic inflow time scaling factor $\frac{R}{u_0}$, the radial position and the quasi-steady axial induction factor.

3.2.3 Load reconstruction from induction measurement

Additionally to the strain-gauge-measured integral turbine loads, these loads are also reconstructed based on the induction measurements. The angle of attack values along the rotor blade are already derived from the experiment through Eq. (3.3). The relative velocity u_{rel} is given by Eq. (3.8). Hence, the information obtained by the momentum part of a BEM code is known from the experiment. So the blade element theory (BET) part of a standard BEM code as outlined in detail by *Hansen (2008)* is used. The force for the blade segments can be calculated for the normal direction according to Eq. (3.11) and for the tangential direction according to Eq. (3.12), where the lift force of the segment is given by Eq. (3.9) and the drag force by Eq. (3.10). The inflow angle is defined by θ.

$$u_{\mathrm{rel}} = \sqrt{u_{\mathrm{ax}}^2 + (u_{\mathrm{ta}} + \Omega r)^2}, \tag{3.8}$$

$$F_{\mathrm{L}} = \frac{1}{2} \cdot C_{\mathrm{L}}(\alpha) \cdot \rho \cdot \Delta r \cdot c \cdot u_{\mathrm{rel}}^2 \cdot F, \tag{3.9}$$

$$F_{\mathrm{D}} = \frac{1}{2} \cdot C_{\mathrm{D}}(\alpha) \cdot \rho \cdot \Delta r \cdot c \cdot u_{\mathrm{rel}}^2 \cdot F, \tag{3.10}$$

$$F_{\mathrm{N}} = F_{\mathrm{L}} \cos\theta + F_{\mathrm{D}} \sin\theta, \tag{3.11}$$

$$F_{\mathrm{T}} = F_{\mathrm{L}} \sin\theta - F_{\mathrm{D}} \cos\theta. \tag{3.12}$$

$C_{\mathrm{L}}(\alpha)$ and $C_{\mathrm{D}}(\alpha)$ are the lift and drag coefficients for the respective angle of attack. These lift and drag polars are obtained by XFoil (see *Drela, 1989*). The lift polars are corrected for 3D effects, as lift coefficients on rotating blades can be significantly higher than for a stationary blade due to the effect of cross-flows related to a stall delay. This effect is most relevant for the root airfoils and was corrected by the method by *Snel et al. (1993)*. The blade segment width is Δr, and c the chord length. The air density is given by ρ. The factor F accounts for the tip losses based on the *Shen et al. (2005)* tip loss model. The integral load signals are reconstructed by integration of the forces along the rotor blade.

The influence of unsteady airfoil aerodynamics (uA) on the blade level, namely the Theodorsen effect, is not contained in the axial wake induction and therefore has to be additionally considered in the reconstruction. The implementation given in detail in *Pirrung et al. (2017)* is used. This is the inviscid part of the unsteady aerodynamics model by *Hansen et al. (2004)*, which treats the shed vorticity effects due to fast angle of attack changes as a time lag on the angle of attack α and has been extended to take the effect of camber into account. Thus, the magnitude and direction of the aerodynamic forces are influenced. The main model is reproduced in Appendix 3.5. The typical uA time constant which determines the lag of the angle of attack due to the uA effect is of the order of $\frac{c}{u_{\mathrm{rel}}}$, whereas the typical time constant of the dynamic inflow effect is $\frac{R}{u_0}$ and at least 2 magnitudes of size larger, as mentioned in Sect. 3.1. Reconstructed loads will be investigated with and without the uA model.

3.3 Results

Here the measurement results are described. In Sect. 3.3.1 the induction in the rotor plane is shown as a function of radial position determined with the procedure described in Sect. 3.2.1. Then Sect. 3.3.2 shows the wake measurements from the hot wires as a function of streamwise position at hub height. Finally Sect. 3.3.3 presents the loads as measured from the strain gauges and the loads derived from the induction measurements according to the procedure of Sect. 3.2.3.

3.3.1 Induction results

In Fig. 3.8a, the measured axial inductions, in Fig. 3.8b, the tangential inductions and in Fig. 3.8c, the derived angle of attack from the LDA measurements are presented for the steady high and low load cases.

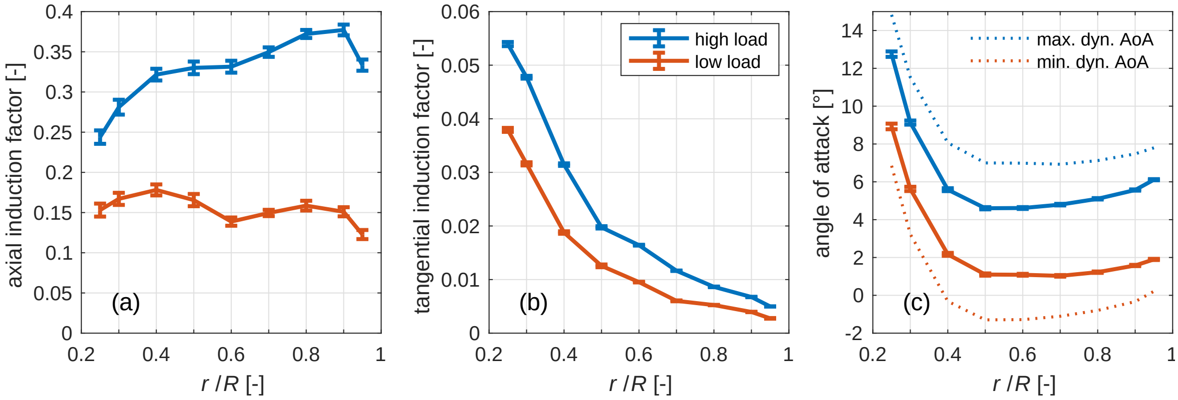

Figure 3.8: (a) Axial and (b) tangential wake induction factors and (c) derived angle of attack distribution from the LDA measurements for the steady high and low load case. The errorbars denote the 95% confidence interval, based on the measured data for axial and tangential velocity in the rotor plane considering 100 measurement cycles.

For the high load case, the axial induction has values between 0.25 near the root (0.25 R) and 0.38 near the tip (0.9 R), in general with an increasing trend with radius apart from the tip nearest radius. The low loaded case has a more uniform loading with values between 0.12 and 0.18. For comparison, the rotor equivalent axial induction obtained from momentum theory ($C_T = 4a(a-1)$) with C_T based on the strain gauge measurements do give similar values of 0.34 and 0.14 respectively.

The tangential induction for both cases is high near the root and decreases with radius with a high rate in the beginning and then more gentle. Due to the larger rotor torque, the high load case shows higher values.

The angle of attack distribution for the high load and low load cases shows angles of attack of 4 to 6° for the high load case from $0.4\,R$ on and 1 to 2° for the low load case. The values increase towards the root for both cases. The stall angle is estimated as the angle of attack with the highest lift coefficient, where the flow is not completely separated. This angle for the used airfoils at the respective Reynolds number of the experiment is at 15° for the root airfoil used up to $0.4\,R$ and at 11.5° for the tip airfoil used from $0.5\,R$ on. Thus, the considered range of the blade is operating outside of the stall regime for both load levels for the steady states.

The observed difference between the two angle of attack distributions is smaller than the pitch step value of 5.9° the blades do pitch. This is due to the flow through the rotor and induction factors that change between the two steady operational states. From this information, the maximum angle of attack range can be estimated a priori, in order to assess the flow conditions during the pitch steps. The dynamic maximum and minimum angle of attack distributions are estimated for an infinitely fast pitch step. We assume in a thought experiment that the flow field of the steady state before the pitch step is unchanged, but the pitch step and thus geometrical change of the inflow angle is already done. This allows us to estimate the extreme dynamic angles of attack, neglecting any damping uA effects for the infinitely fast pitch step.

These maximum and minimum dynamic angles of attack are shown as dotted lines in Fig. 3.8c. For the step to high load, the stall limit is approached at nearly 15° angle of attack at the root near radius of $0.25\,R$. For the step to low load, there is a minimum dynamic angle of attack of about $-1.5°$ in the middle of the rotor blade. This lowest angle of attack gives a lift coefficient of zero. For a finitely fast pitch step, the flow already adapts during the pitch step and the extreme dynamic values are closer to the new steady values. The uA effects further dampen the overshoot of angles of attack. So apart from the blade root at the step to high load, where the stall limit is approached, the blade is operated outside the stall region for the pitch steps.

The axial induction factor transients are shown in Fig. 3.9 for four different radii (0.3, 0.5, 0.7 and $0.9\,R$) for both pitch steps. They show direct evidence of dynamic inflow where the induction factors and therefore induced velocities reach the new equilibrium value only slowly.

The fits of the one-time-constant (1c) and two-time-constant (2c) models are also shown in the plots. The fits start from the instance the pitch step is terminated at t_0. At that time the axial induction has already adapted by about 28 % on average of the difference between the steady axial induction levels for the radii from 0.3 to $0.9\,R$ independent of the pitch direction.

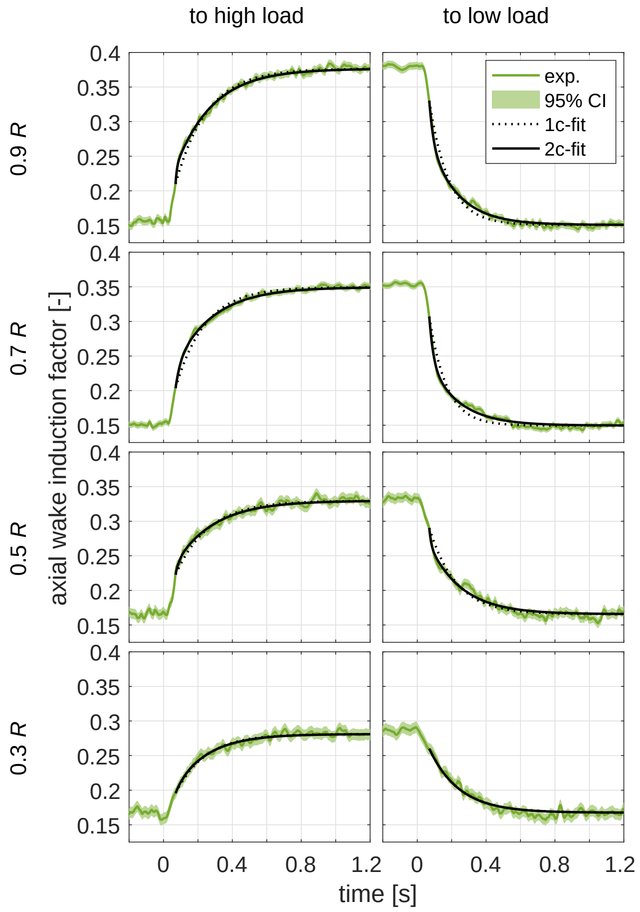

Figure 3.9: Axial wake induction factor over time for pitch step to high load and low load for the four radii $0.3R$, $0.5R$, $0.7R$ and $0.9R$ and the fitted exponential decay models with one time constant (1c) and two time constants (2c).

The fitted time constant τ_{single} of the 1c model is plotted over the radius for both pitch directions in Fig. 3.10. In the root near region up to $0.4R$ both pitch directions show similar values apart from the radius at $0.25R$, where the step to high load has a higher time constant. For radii from $0.5R$ on, the step to high load shows higher values than the step to low load. There is no clear trend obvious for the step to high load. In contrast, for the step to low load, there is a trend towards reduced time constants towards higher radii.

In Fig. 3.11, the three fitting parameters of the 2c model are presented. In the top row, the three fitted variables $k = k_{\text{free}}$, τ_{fast} and τ_{slow} are plotted over the radius. Near the root at $0.25R$, the k value for both pitch directions has a value of 1 and nearly 1 respectively, indicating no contribution from τ_{fast}, which consequently is also not plotted for these radii. For radii up to $0.5R$, the values for the step to low load have a higher k_{free} value than for the step to high load, switching from $0.6R$ on to the tip. τ_{fast} does have similar

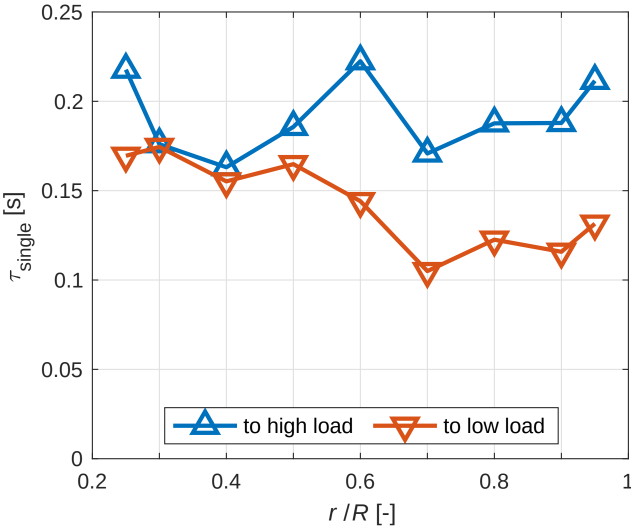

Figure 3.10: One-time-constant model fit of τ_{single} to the axial wake induction factor over the radius for both pitch directions.

values from $0.4\,R$ to the tip and for both pitch directions. Towards the root the decay process is only defined by τ_{slow} there, as k_{free} equals or nearly equals 1. For τ_{slow}, there is no clear radial trend for both pitch directions, but a clear difference between pitch directions. For the step to high load, τ_{slow} is higher for all radii than for the step to low load. Due to the influence of the varying weighting ratio of fast and slow time constant, a direct comparison of these time constants is limited.

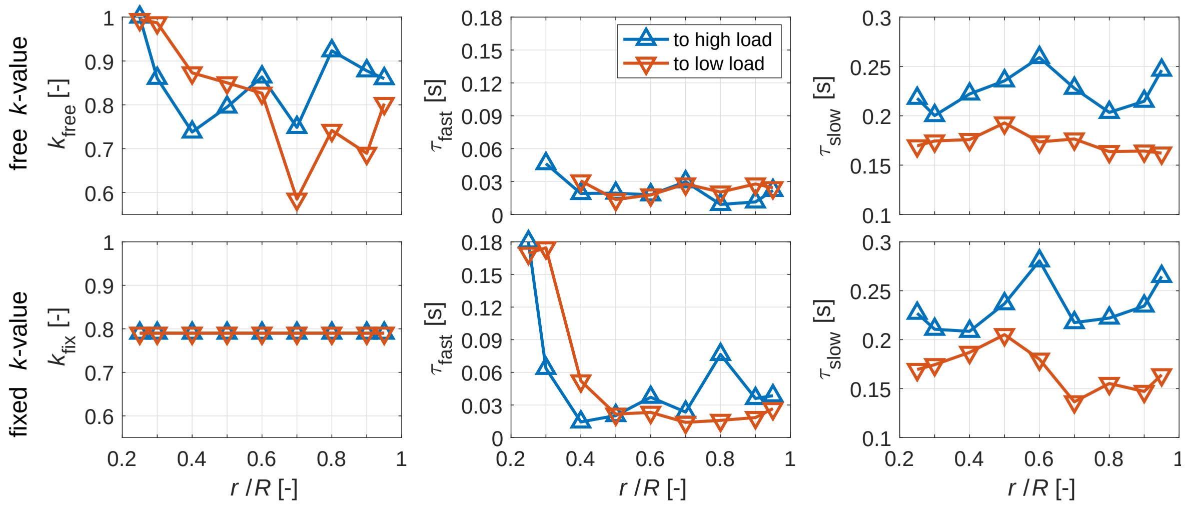

Figure 3.11: Two-time-constant model fit to the axial wake induction factor, derived from the rotor plane LDA measurements with the ratio k and the fast τ_{fast} and slow τ_{slow} time constants. In the top row the k value is fitted as a free parameter. In the bottom row the weighting ratio of fast and slow time constant k is fixed (to the mean value of both pitch directions and radii of the fit in the top row).

To overcome this limitation, the ratio k is fixed to a value of $k_{\text{fix}} = 0.79$, which is the mean value for all radii of both pitch directions of k_{free}. With this setting, τ_{fast} contributes by 21 % to the decay of the axial induction. This fit is shown in the bottom row of Fig. 3.11.

The fitted τ_{fast} is high near the root for both pitch directions. For the step to high load, τ_{fast} decreases from the root to 0.4 R, after which there is an increase again (ignoring an outlier at 0.8 R). From 0.5 to 0.9 R, τ_{fast} increases by 67 %. For the step to low load, τ_{fast} has more constant values from 0.5 to 0.9 R, decreasing by 14 %. Hence τ_{fast} is smaller for the negative load step, for radii larger than 0.5 R, which represents 75 % of the rotor swept area.

Values of τ_{slow} are slightly higher for the step to high load and show more variation than in the prior fit with $k = k_{\text{free}}$ ratio. There is a slight radial trend to higher values, with an increase in τ_{slow} from 0.3 to 0.9 R by 11 %. For the step to low load, also more variation is apparent, and a slight radial trend towards lower values is indicated, with a decrease in τ_{slow} from 0.3 to 0.9 R by 16 %. Taking the mean value over radius, the slow time constant for the step to low load is about 28 % lower.

The fitting accuracy of the applied models is determined based on the root mean square error (RMSE) in the fitting range t_0 to t_{fit} between the measured signal and the respective fitted model and plotted over the radius in Fig. 3.12.

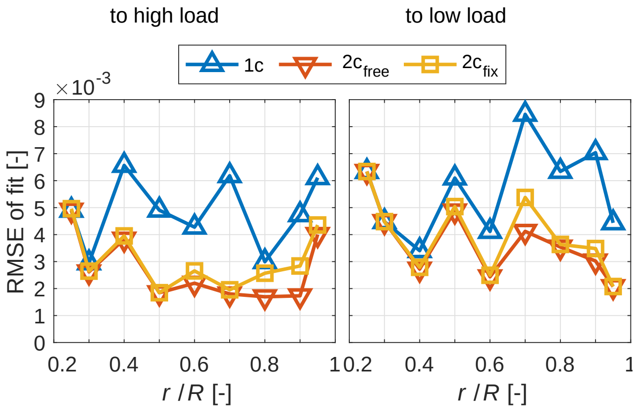

Figure 3.12: Root mean square error (RMSE) between measured axial wake induction factor and the three fitted models, 1c-fit and 2c-fit with k_{free} and $k_{\text{fix}}$for both pitch directions.

For both step directions, there is no difference in RMSE for the root near stations up to 0.3 R between the fitting models, which are the 1c and 2c model, one with $k = k_{\text{free}}$ and one with $k = k_{\text{fix}}$. For higher radii, the error of the 1c fit is higher than for the two variants of the 2c model. The differences between the two variants of the 2c model are

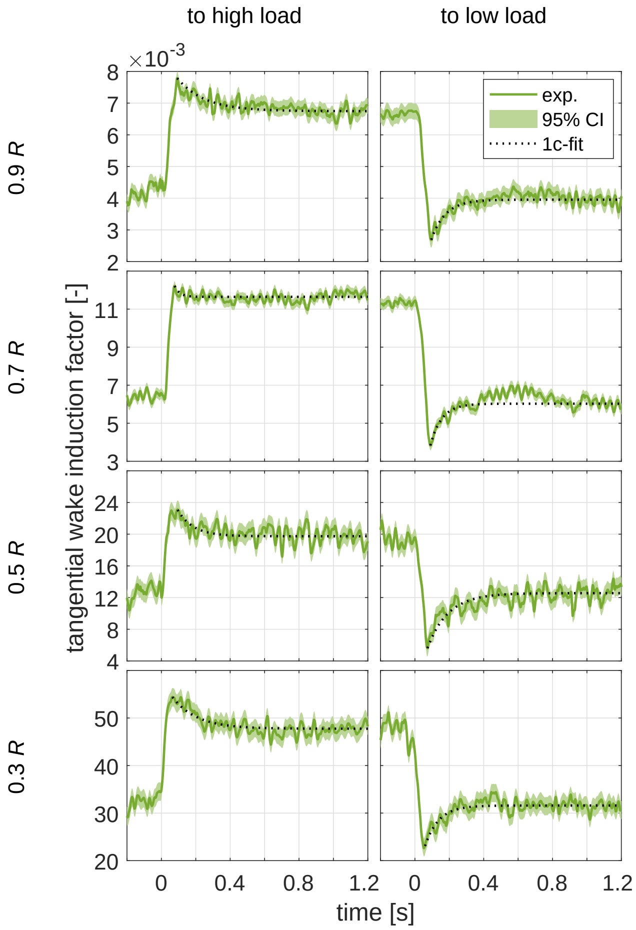

Figure 3.13: Tangential wake induction factor over time for pitch step to high load and low load for the four radii 0.3 R, 0.5 R, 0.7 R and 0.9 R and the fitted exponential decay model with 1 time constant (1c).

small, showing that there is only a small penalty for fixing the k ratio.

The tangential wake induction factors over time for both pitch directions are presented for the four radii 0.3, 0.5, 0.7 and 0.9 R with the fit of the 1c model in Fig. 3.13.

In contrast to the axial induction, the tangential induction shows an overshooting behaviour. The exponential fit starts around t_0 at the respective minimum or maximum peak, as this showed to improve the fitting. The starting point of the fit thus varies between 0.059 and 0.095 s, with a mean value of 0.074 s. The overshoot, in general, seems more prominent for the step to low load and only barely present within the signal noise at the radius of 0.7 R for the step to high load.

The fitted τ_{single} values to the 1c model are plotted over radius for both pitch directions in Fig. 3.14. Cases where the overshoot is smaller than 3 standard deviations of the filtered signal of the new equilibrium were excluded due to a very high sensitivity on the starting point of the fit.

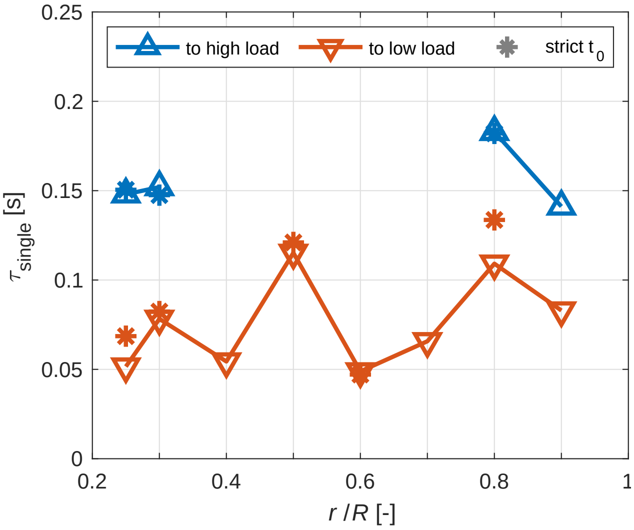

Figure 3.14: One-time-constant model fit of τ_{single} to the tangential wake induction over the radius for both pitch directions.

For the step to high load, only two radii at the root and two radii near the tip fulfil this requirement, whereas for the step to low load only the tip most radius at 0.95 R is excluded. For the radii where values for both pitch directions are available, the step to high load shows higher $\tau_{\rm single}$ values. For both pitch directions, $\tau_{\rm single}$ is lower than the corresponding $\tau_{\rm single}$ for the axial inductions. We see no connection of this unexpected overshooting behaviour of the tangential induction to the slight rotor speed deviations, which are present between 0 and 0.6 s and thus at a time frame up to 1 order of magnitude higher.

The influence of the small, allowed shift in the start of the fit is also investigated. For a strict starting point of the fit at t_0, shown in Fig. 3.14 as stars, the set criterion of overshoot to noise is fulfilled for only three radii for the step to high load and five radii for the step to low load. For the available radii, however, there are only negligible differences to the shown fit in comparison to the observed spread.

3.3.2 Wake results

In the following the hub height hot-wire measurements downstream of the turbine in the near and close far wake up to 2 D downstream are analysed. The wake measurements are shown as a surface plot for four different timestamps in Fig. 3.15 for both pitch directions and normalised by the free stream velocity.

The first contours at $t = 0$ s are the starting equilibrium condition. For the step to high load, the initial wake, being the steady low-load case, shows wake velocities around $0.8\,u_0$ coloured in green tones for 0.2 to $1\,R$ radial positions. For the step to low load, the initial velocity field in the wake, being the steady high-load case, is around $0.5\,u_0$, coloured in blue tones. The dotted red line is the isoline of $0.9\,u_0$, which is used as an indication of the wake stream tube.

The contours for the following timestamps show the transition to the new steady state. These transitions seem at first glance different for the two pitch directions. For both pitch directions at $t = 0.4$ s and at around 1 to $1.25\,D$, there seems to be the transition line where old and new wake meet. The indicated wake radius shows that the dynamic wake streamtube is constricted at $1\,D$ for the step to high load, whereas it is widened up for the step to low load. This behaviour is opposite to what is expected for the new steady streamtubes, where for the step to high load, the wake widens, due to the higher thrust. Further, it narrows due to the lower thrust for the step to low load. For the time stamp at $t = 0.8$ s, a similar picture can be seen where this transition between old and new wake has progressed to around $1.75\,D$. The figure at the left bottom is very similar to the figure at the right top, and the same holds for the figure at the right bottom and left top. This indicates that the new equilibrium is approached at $t = 1.2$ s.

To further interpret this measurement, normalised velocity contours are presented to the new equilibrium steady state in Fig. 3.16. The normalised difference is defined as $\Delta u/u_0$, with $\Delta u = u_t - u_\infty$, where u_t is the velocity at the respective time at a measurement position, and u_∞ the velocity at the same point at the new steady condition after the pitch step.

Therefore, a value of 0.5 means that the wake has to adapt by $0.5\,u_0$ to reach the new equilibrium. The starting conditions for both pitch directions look alike, as they show the difference between the two steady states. At the timestamp of $t = 0.4$ s, a very similar shape of this potential like area is seen for both pitch directions. A widening of the wake for the step to low load is indicated when concentrating on the orange field near the tip radius, which is at a radial position of $1\,R$ for the step to high load and at $1.2\,R$ for the step to low load. For the step to low load, this orange maximum has travelled further than for the step to high load. At the timestamp at $t = 0.8$ s, the wake for the step to low load has adapted more to the new steady state than for the step to high load. At the timestamp of $t = 1.2$ s, for the step to low load, the equilibrium is reached. For the step to high load, the wake has not completely adapted to the new equilibrium with still a clear lighter blue area at $2\,D$.

Next, the deployment of the axial wake velocity as a response to the load steps is analysed. Six of the hot-wire signals used to make the contour plot are plotted over time for the step to high load for the radii of 0.2, 0.6 and $1\,R$ at 0.5 and $1.5\,D$ distance

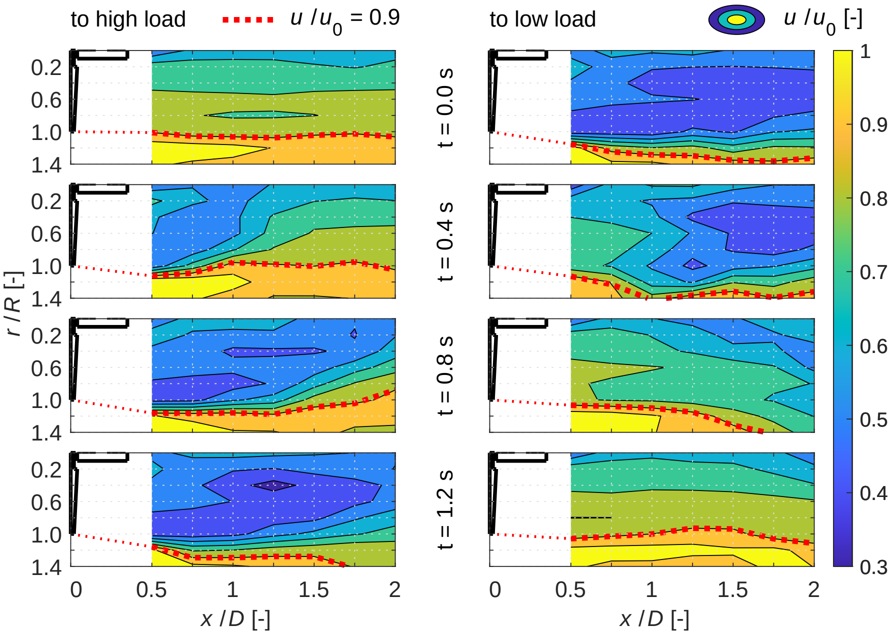

Figure 3.15: Top view on velocity contour in the horizontal plane at hub height of the wake at the four different time stamps, 0 s, 0.4 s, 0.8 s and 1.2 s after the pitch steps to high and to low load, normalised by the free stream velocity. The turbine dimensions are indicated in correct scale in the plots as a reference, with the x-axis being the axis of rotation.

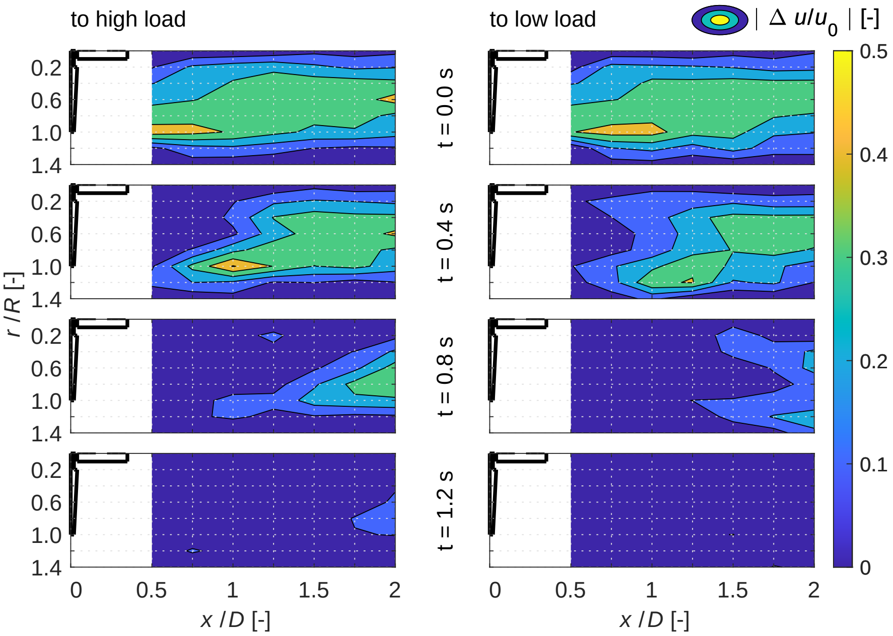

Figure 3.16: Top view on velocity contour in the horizontal plane at hub height of the difference to the new steady wake equilibrium at the four different time stamps, 0 s, 0.4 s, 0.8 s and 1.2 s after the pitch steps to high and to low load, normalised by the free stream velocity. The turbine dimensions are indicated in correct scale in the plots as a reference, with the x-axis being the axis of rotation.

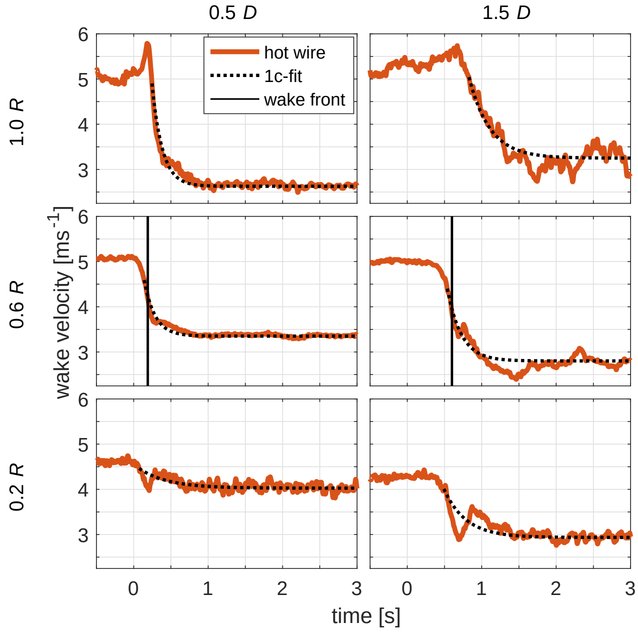

Figure 3.17: Ensemble averages of the axial wake velocity measured by hot wires for the three radii of $0.2R$, $0.6R$ and $1R$ at $0.5D$ and $1.5D$ distances behind the turbine for the step to high load.

behind the turbine are presented in Fig. 3.17.

For the radius at $0.6\,R$, a vertical line, called a wake front, marks a characteristic t_1 of the exponential decay, where the signal has adapted by 50 % to the new equilibrium value. For the radius of $0.2\,R$, the velocity transient shows a local structure, where the velocity quickly decreases and increases again to subsequently decrease to the new equilibrium for both shown distances. The effect of the nacelle is assessed as unlikely to be the reason for this structure, as the nacelle only has a radius of $0.1\,R$. At the radius of $0.6\,R$ the signal decays exponentially. At $1\,R$ the signal increases quickly to a peak at nearly free stream velocity before decreasing exponentially to the new steady value. The signals at $0.5\,D$ behind the turbine for the two higher radii, 0.6 and $1\,R$, show a better fit with the exponential decay function. For the farther distance at $1.5\,D$, the hot-wire signals show an overshoot to lower velocities than the new equilibrium at around 1.5 to 1.7 s for the two larger radii. The results for the indicated time constant fit are presented and discussed as an additional result in Appendix 3.5.

In the next step, the wake front velocity is analysed to measure how fast the transition point (the wake front) between the old wake and the new wake convects. This wake front can be thought of as being similar to a weather front. We define the wake front velocity by the time this characteristic wake front needs to travel from one considered downstream position to the next. So exemplarily in Fig. 3.17 at $0.6\,R$ there is the wake front for $0.5\,D$ at $t_{\mathrm{front},\,0.5\,\mathrm{D}} = 0.20\,\mathrm{s}$ and for $1.5\,D$ at $t_{\mathrm{front},\,1.5\,\mathrm{D}} = 0.56\,\mathrm{s}$. Within this time difference, the wake front thus has travelled by $1\,D$, giving a mean wake front velocity between these downstream distances.

In Fig. 3.18, this wake front velocity is shown for both pitch directions, normalised by the free stream velocity. The wake front velocity is obtained by considering a mean value of the hot-wire positions at the radii of 0.4, 0.6 and $0.8\,R$. These signals were weighted based on their position with the conservation of mass in mind. For that, each position was attributed an annulus reaching $\pm 0.1\,R$ from the radius of the position. This mean velocity signal at the different downstream distances, which is used to obtain the wake front velocity, represents in this definition (0.3 to $0.9\,R$) the major part of the swept area of the rotor.

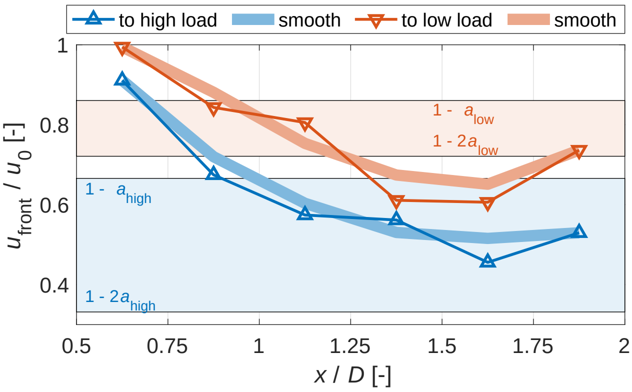

Figure 3.18: Velocity of the wake front for both pitch directions, normalised by the free wind velocity. For orientation also the theoretical normalised wind velocity in the rotor plane $(1-a)$ and in the far wake $(1-2a)$, based on the measured thrust coefficient, are indicated for both steady states.

Thus between every two considered downstream distances a mean velocity with which the wake front moved can be calculated. Between the two nearest distances to the rotor, 0.5 and $0.75\,D$, the wake front convects for both cases with $0.9\,u_0$ to u_0. This is faster than the expected velocity in the rotor plane for even the low loaded rotor. With increasing distance to the rotor for both cases, the wake front velocity decreases up to $1.5\,D$, whereas the velocity is higher for the step to low load. Based on this defined wake front velocity the wake convection is on average 26 % faster for the step to low load.

3.3.3 Load results

Next, the integral loads are compared as shown in Fig. 3.19. Two independent methods have been used: One measured directly with strain gauges (SGs) and one obtained

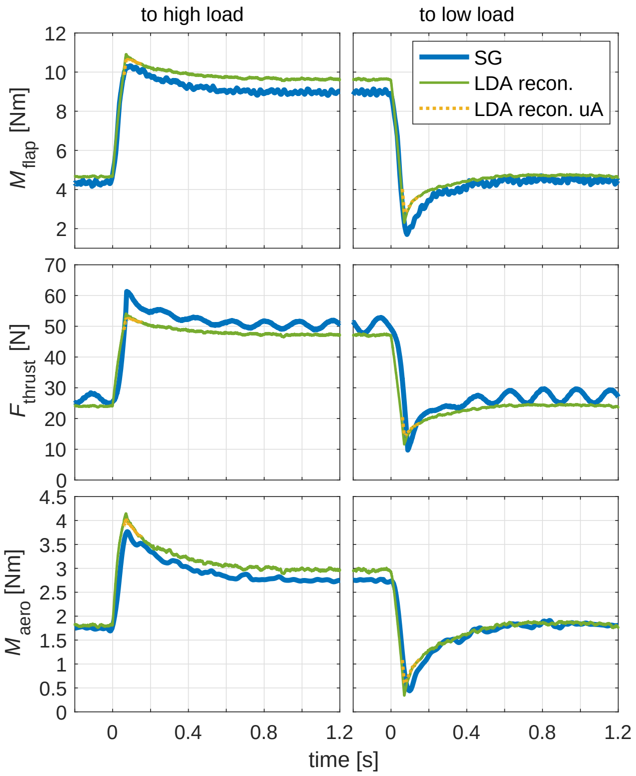

Figure 3.19: Integral turbine loads based on strain gauges with (SG) and without (SG no corr.) the dynamic corrections (as introduced in Sect. 3.2.1) and reconstructed loads based on Blade Element Theory from the LDA measurements without and with uA model.

indirectly from the LDA measurements in the rotor plane with the reconstruction procedure given in Sect. 3.2.3 (denoted LDA recon.). For the latter, it is distinguished between the use of the uA model and without it. For the strain-gauge measurements, additionally a version without the dynamic corrections for F_{thrust} and M_{aero} (denoted SG no corr.) as introduced in Sect. 3.2.1 is presented to show the raw data. For the reconstructed loads, the influence of unsteady airfoil aerodynamics (uA) effects is shown around the overshoot, where it differs from the case without the uA model.

Firstly, a clear overshooting behaviour of all load signals is apparent. Comparing the strain gauge measurements for M_{flap}, F_{thrust} and M_{aero} with the signals reconstructed from the LDA measurements indicates a good match of signals by means of steady values as well as the dynamic overshoot. Considering the uA model leads to a peak shaving of the overshoot. Also, the overshoot peak for the strain gauge signals, as well as for the reconstructed value with the uA model, is slightly shifted to higher t_0 values.

A more detailed comparison of the steady values at high and low loads between the strain-gauge-measured integral loads and the reconstructed loads is plotted in Fig. 3.20,

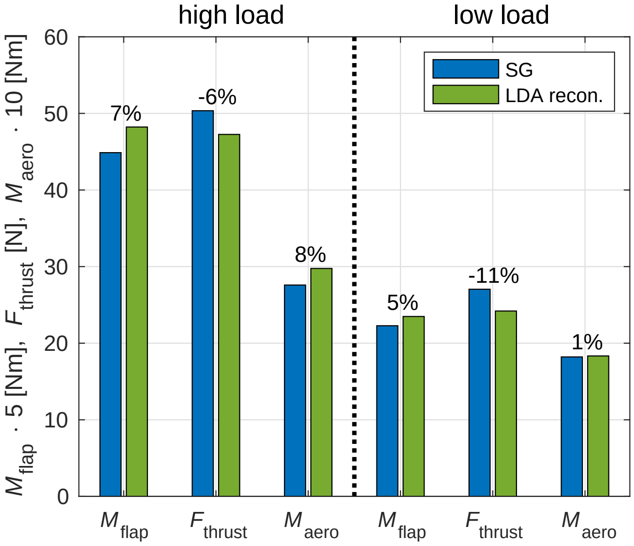

Figure 3.20: Comparison of the steady load levels for high and low load for the integral turbine loads M_{flap}, F_{thrust} and M_{aero} obtained by strain gauges and reconstructed from LDA measurements.

alongside the deviations of the reconstructed loads to the strain-gauge-measured loads. The two methods give similar load levels. Deviations differ between the load signals. The good agreement in terms of steady loads indicates good performance of this reconstruction approach with maximum deviations of 11 %.

The slight overprediction of reconstructed loads for the M_{flap} and M_{aero}, on the one hand, and the underprediction of F_{thrust} is attributed to a higher influence of the larger radii. For the first two signals, the blade acts as a lever arm for the sectional forces, thus giving them a higher weighting. In contrast, the sectional forces are added without considering a lever arm for F_{thrust}.

Further, the dynamics after the pitch step are compared. The amount of load overshoot, normalised by the difference between the steady values, is given for the load signals for both pitch directions in Fig. 3.21a.

The addition of the uA model reduces the amount of overshoot for all load channels. For M_{flap}, the reconstructed loads provide a good fit, whereas the values with uA model show differences. High deviations are seen for F_{thrust} between strain gauge measurement and reconstructed loads, especially with the uA model but also without the model, for both pitch directions. The torque M_{aero} shows a good match with the reconstructed loads for both pitch directions.

The amount of overshoot is higher for the step to low load, when comparing the amount of overshoot between the two pitch directions per load channel and method. Based on the LDA reconstructed loads, which are not subject to dynamic corrections

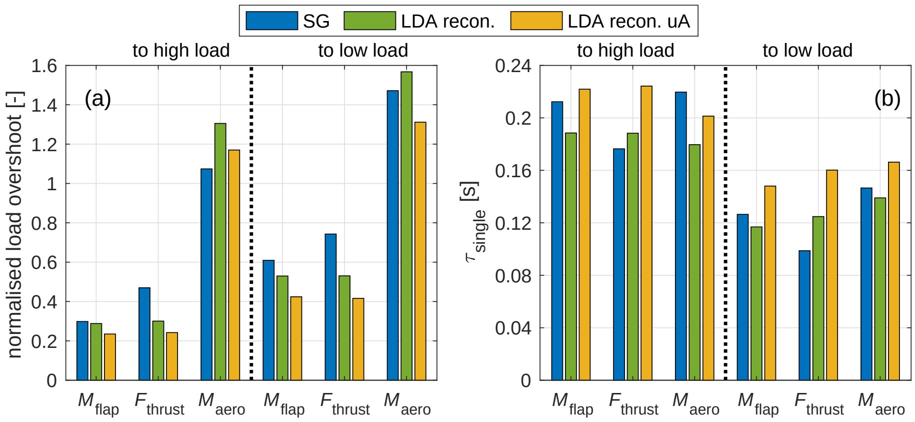

Figure 3.21: (a) Comparison of the amount of overshoot of the integral turbine loads M_{flap}, F_{thrust} and M_{aero}, obtained by strain gauges and reconstructed from LDA measurements without and with uA model for both pitch directions. (b) Comparison of the τ_{single} fit of the one-time-constant model to these integral loads.

that might introduce errors, the normalised overshoot for M_{flap} and F_{thrust} is similar per pitch direction, whereas the overshoot in M_{aero} is 3 to 4.5 times higher.

The fitted values for the one-time-constant model to the integral loads is presented in Fig. 3.21b for both pitch directions. The time constants for all load signals and methods are longer for the step to high load than to low load. This is consistent with what was found in the velocity results before. The time constant is in general increased by including the uA model. For the step to high load, M_{flap} and M_{aero} show a good match with the reconstructed uA method and an acceptable match for the step to low load. For F_{thrust}, there are higher deviations between the strain-gauge-based time constant and the time constant based on the reconstructed uA load.

In order to assess the reasons for the differences in load overshoot it is of interest to investigate the theoretical maximum load overshoot when changing from one operational point to the other. This can be estimated based on the steady states of the operational points and the theoretical dynamic maximum and minimum angle of attack distribution, as was introduced in Fig. 3.8. The steady integral loads for high and low loads are reconstructed as before for Fig. 3.19. For the maximum and minimum load, the maximum and minimum dynamic angle of attack distributions are used. The inflow to the segments is, however, defined by the inductions for the steady state just before the pitch step. An infinitely fast pitch step is assumed, where the geometrical change of the blade pitch already happened, but the flow did not start to adapt. This approach neglects uA effects that showed to reduce the overshoot. The derived theoretical maximum amount of overshoot based on the difference of maximum, respectively minimum, load

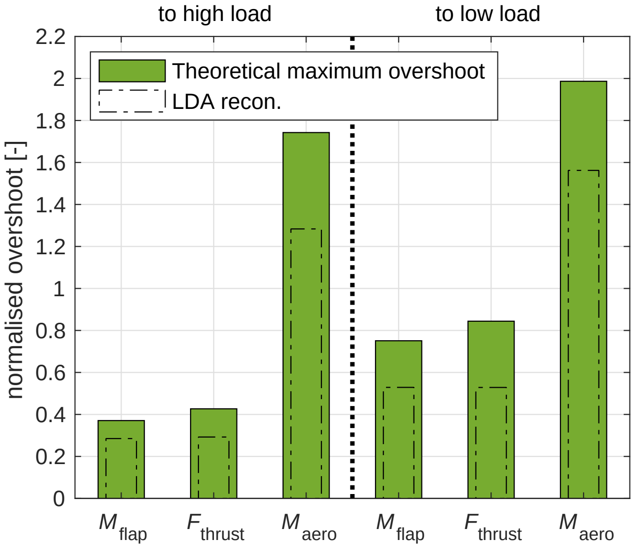

Figure 3.22: Theoretical dynamic overshoot for the step to high and low load for the integral turbine loads M_{flap}, F_{thrust} and M_{aero}, based on reconstruction from the LDA data, assuming an infinitely fast pitch step in comparison to the LDA recon. case from Fig. 3.21 a.

and the following steady load is plotted in Fig. 3.22.

A clear difference can be seen between the pitch directions for the axial loads M_{flap} and F_{thrust}, with about twice as high an amount of overshoot for the step to low load than for the step to high load. For the torque, the general trend is the same with 2.5 to 4.5 times the overshoot in comparison to the other signals. The trend is similar to the repeated LDA recon. values in the plot.

3.4 Discussion

In this section, the results for the inductions, wake flow and loads will be discussed. A focus for comparisons is on publications in connection to the NREL unsteady aerodynamics experiments phase VI (see *Hand et al., 2001*), later referred to as just phase VI, as this experiment is the most widely studied dynamic inflow dataset so far.

3.4.1 Induction transients

Dynamic inflow phenomena on wind turbines were already indirectly shown in experiments based on integral loads for the 2 MW Tjæreborg turbine (see *Øye, 1991*), based on pressure-sensor-derived sectional forces on the phase VI (see *Hand et al., 2001*) and MEXICO (see *Boorsma et al., 2018*) model turbines and in the wake measurements behind an actuator disc with dynamic thrust changes (see *Yu et al. 2017*). The presented axial induction transients in Fig. 3.9 based on the LDA measurements in the rotor plane are the first direct experimental evidence of dynamic inflow phenomena for wind turbines.

Pitch steps of the phase VI experiment were performed at $5\,\mathrm{m\,s^{-1}}$ wind speed and a tip speed ratio (TSR) of 7.5. The pitch step of 15.9° took place during approximately 1/3 rotor revolution (pitch rate of $57°\,s^{-1}$ over $0.28\,s$). This extreme pitch step is between a very highly loaded rotor at a rotor equivalent axial induction of 0.5 and 0 for the unloaded rotor. At the highly loaded rotor state, the turbine is in the turbulent wake state. This high induction state was later suspected to be responsible for problems in validation *(Sørensen and Madsen, 2006)*.

Pitch steps in this paper were performed at $6.1\,\mathrm{m\,s^{-1}}$ and a TSR of 7.4. The pitch step of 5.9° was performed during approximately 1/2 rotor revolution between rotor equivalent inductions of 0.34 and 0.14. The experiment thus is not operated in the turbulent wake state at the high load case.

The observed slight radial dependency for the single time constant (see Fig. 3.10), where the values slightly decrease towards the tip for the step to low load is in accordance with the observation by *Schepers (2007)* for the phase VI experiment, despite the more extreme change in rotor loading.

Pirrung and Madsen (2018) reproduced this behaviour for the phase VI experiment in a cylindrical wake model simulation. They explain this observation by the nature of the dynamic inflow process that cannot be described correctly by a one-time-constant model but by a two-time-constant model. They reason that the axial induction adapts by different amounts during the pitch step depending on pitch direction. This is governed by the wake velocity before the pitch step and thus influences the one-time-constant fit to the normal forces after the overshoot. In contrast, in the presented axial induction transients (see Fig. 3.9), it is seen that it adapts similarly during the pitch step for both pitch directions, by 28 % on average.

For the two-time-constant model fits to the axial wake inductions, two variants of time constants, one with a freely fitted weighting ratio k_{free} and one with a prescribed weighting ratio k_{fix}, are shown in Fig. 3.11. Using k_{fix} allows for a direct comparison of τ_{fast} and τ_{slow} between the pitch directions. The radial dependency of τ_{fast}, with high values towards the root, extends further into the blade for the step to low load. In their investigation of the normal force measurements on the phase VI experiment, *Sørensen and Madsen (2006)* also saw this high τ_{fast} values at the root nearest radius of $0.3\,R$ for the step to low load but not for the step to high load. In the present and the phase VI experiment, this high τ_{fast} near the root is of the order of τ_{slow}. In the present experiment, there is a difference in the τ_{fast} between pitch directions, with lower values for the step to low load from $0.5\,R$ to the tip. This difference between the pitch directions is not seen by *Sørensen and Madsen (2006)*. Furthermore a radial dependence can also be seen from the middle of the blade towards the tip with an increase for the step to high load (67 %) and a slight decrease for the step to low load (−14 %).

For τ_{slow}, a very slight radial dependency can be seen for the fit with k_{fix}, with slightly increasing values (11 %) towards the tip for the step to high load and slightly decreasing values (−16 %) for the step to low load, similar to the fit of τ_{single}.

The τ_{slow} values are on average about 28 % faster for the step to low load than for the step to high load. The same trend can be seen in *Sørensen and Madsen (2006)* but by a much higher value of around 100 %. The likely explanation is the higher difference in axial induction between the steady load levels for the phase VI experiment. *Sørensen and Madsen (2006)* and *Pirrung and Madsen (2018)* discuss this scaling of the time constants with the wake deficit and thus mean axial induction of the rotor. Also, the Øye dynamic inflow model (see *Schepers and Snel, 1995*) and other recent dynamic inflow models (e.g. *Madsen et al., 2020*) use the axial induction to scale the time constants. There the fast time constant represents the near-wake dynamics and decreases with radius and the slow time constant represents the far-wake dynamics.

Sørensen and Madsen (2006) and *Pirrung and Madsen (2018)* elaborated, based on measurements and simulations, that a two-time-constant model better describes the dynamic inflow process than a one-time-constant model. The two-time-constant approach also was implemented in the Øye dynamic inflow model (see *Schepers and Snel, 1995*). *Yu et al. (2019)* further showed, based on actuator disc vortex models, that a two-time-constant model describes the process better than a one or three-time-constant model. Comparing the fitting error of the 1c and 2c models to the axial wake induction measurements of the present experiment (see Fig. 3.12), this finding is verified based on the first direct measurements of dynamic inflow phenomena. However, the root region is an exception, as the process is defined by only one time constant.

The only minor differences in fitting error between the two variants with k_{free} and k_{fix} (see Fig. 3.11) illustrate the high sensitivity of the fitting process. Small changes in k have a noticeable impact on the τ_{fast} and τ_{slow} values, where one increases as the other decreases.

The overshooting behaviour of the tangential induction is a new finding. The time constants of the one-time-constant model have no clear radial dependency. They are lower for the step to low load and in general, slightly lower than those fitted for the axial induction. The overshoot also is more prominent for the step to low load. This behaviour is of interest for the physical understanding of the dynamic inflow effect, as the overshoot in the torque is directly counteracted by the change in wake rotation. We assume that the shed vortices due to the change in circulation introduce this instant overshoot in tangential induction. For the modelling of the dynamic inflow effect in BEM-based codes, this behaviour is only of secondary interest, as the influence of the tangential induction on the angle of attack is negligible, apart from the blade root.

3.4.2 Wake evolution

No relevant influence of the shear layer between the open jet wind tunnel and the surrounding air is seen in the wake snapshots (see Fig. 3.15). On that basis, it was decided to include these measurements in the paper. The main near-wake and beginning far-wake dynamics due to the pitch step should not be disturbed, despite the high blockage ratio of 0.28, as long as the wake and the shear layer of the open jet wind tunnel flow do not interact.

The velocity snapshots in the wake show differences in wake evolution between the pitch directions. The faster progression of the wake for the pitch step to low load supports the presumption made by *Schepers (2007)* of different convection velocities of the wake consisting of the old vorticity and new vorticity, depending on the pitch direction. We assume the faster convection of this mixed wake for the case of the step to low load, starting with a low wake velocity pushed by a higher wake velocity to be the main driver of the faster time constants (τ_{single} and τ_{slow}) of the axial wake induction.

The dynamic widening of the wake after the pitch step to low load, as drawn in Fig. 3.15, is a new finding. We attribute it to the sudden change in trailed vorticity shed from the blade tip region. Part of the slow old wake is then pushed outboard by the fast new wake. The wake is not accelerated by the fast new wake at these larger radii but by the even faster free stream wind velocity. This behaviour is a possible explanation for the decreasing time constants τ_{single}, also τ_{slow}, towards the tip for the pitch step to low load.

The overshoot in the velocity in the wake after a sudden change in thrust, as observed here for the radii at $1.0\,R$ for the step to high load (see Fig. 3.17), has been discussed by *Yu et al. (2017)* based on wind tunnel experiments with a variable porosity actuator disc. They attribute these overshoots to the shed vorticity at the actuator disc edge due to the fast thrust change. The local structure at $0.2\,R$, where the root transition towards the axis of rotation starts, is opposite to the overshoot at $1\,R$ for the step to high load. We assume this to be the counterpart, the shed vorticity at the blade root, due to the sudden change in trailed vorticity. A connection of this shed root vortex to the radial dependency of τ_{fast} near the root cannot be concluded from the data but seems possible.

The quantitative comparison of the wake front velocity (see Fig. 3.18), as a measure of the convection of the transition point between old and new wake, shows the faster velocity for the step to low load. On average, this wake convection velocity is 26 % faster for the step to low load than for the step to high load. This difference resembles the difference in τ_{single} and τ_{slow} from the induction investigation in Sect. 3.4.1.

A fast initial wake front velocity is seen between 0.5 and 0.75 D, which is near the free stream velocity and higher for both cases than the expected axial wind velocity in the rotor plane for the low loaded rotor. An obvious explanation is that in the near wake, the dynamic inflow process of the whole rotor is governed by the influence of the trailed tip vortex, which does convect at similar velocities.

In the further course, the wake front velocity slows down for both cases. For the step to low load, it even slows down between 1.25 and 1.75 D to a lower value than the far-wake velocity according to momentum theory for the new steady state. This behaviour can be explained by the mixed wake of both the old and new wake, which influence each other.

3.4.3 Load transients

The general comparison of the load signals obtained from strain gauges and reconstructed from the LDA measurements (see Fig. 3.19) shows a good agreement and thus proved the physical consistency of the induction measurements for these dynamic experimental cases.

For the steady equilibrium, the comparison between the strain gauge measurements and the reconstructed loads (see Fig. 3.20) yields in generally good agreement, apart from the thrust at low load. Especially the here relevant high angle of attack region for the root airfoil is suspected to have uncertainties related to the low Reynolds number and possible laminar separation bubbles that can significantly increase the local lift.

For the flapwise blade root bending moment and the thrust, the load overshoot is much more pronounced for the step to low load than for the step to high load, whereas the trend for the torque is the same but to a smaller extent. The magnitude of the overshoot depends on how much the axial induction has already adapted during the pitch process. As discussed in Sect. 3.4.1, they adapt a similar amount during the pitch step for both pitch directions, so this cannot explain the difference in overshoot between the pitch directions. The more pronounced overshoot of loads is also discussed for the phase VI measurements in *Schepers (2007)*. He suspected the high angles in the stall region at the highly loaded rotor blade to be a possible reason for that phenomenon. In contrast, the high load case is operating safe outside of the stall regime for the experiment presented here, apart from the very root.

The higher relative overshoot of the torque by a factor of 3 to 4.5 compared to the flapwise blade root bending moment and the rotor thrust can be related to the lag in inflow angle and thus angle of attack behind the quasi-steady value. M_{flap} and F_{thrust} feel the effect mainly due to the change in the magnitude of the lift force, while M_{aero} feels the change in magnitude and also the change of the projection of the lift force in the tangential direction due to the lag of the inflow angle (see Eq. 3.12). Because the F_{thrust} and mostly also M_{flap} are determined by the cosine of the inflow angle (see Eq. 3.11), the effect of the inflow angle lag is much smaller here.

The simplified approach to estimate the theoretical maximum overshoot for the load signals based on the steady inductions and the pitch angle change with the BET reconstruction (see Fig. 3.22), provides a solid reason for the different amount of load overshoot. It only depends on the turbine load characteristic, as the theoretical overshoot show a very similar ratio between load channels and pitch directions to the actual measured and reconstructed load overshoot. The angle of attack overshoot for both pitch directions is the same in this thought experiment; however, near the high load the turbine reaction is less sensitive to the angle of attack changes than at the low load state.

Further, in the overshoot analysis (see Fig. 3.21a) the large differences for the thrust between the strain gauge measurement and the reconstructed loads, both with and without the unsteady airfoil aerodynamics model, catches the eye. At closer investigation, the dynamic correction based on the estimated eigenfrequency and damping coefficient seems to be unsuited for very detailed comparisons. Therefore, this signal channel is omitted in the discussion of the detailed comparison. For the blade root bending moment and torque, the fit is good.

The 1c model investigation shows a good agreement between the strain-gauge-measurement-derived and reconstruction-based τ_{single} values. They are larger for the step to high load than for the step to low load, which is consistent with what was found before in the analysis of induction and wake results. They have a similar size to the fitted time constants to the axial inductions. The small changes in the overshoot of the reconstructed loads the uA model introduces demonstrate the sensitivity of the time constant fits to these small changes in the signal.

Structural interactions are assumed to be the main driver for the observed differences in overshoot and also for the differences in the fitted time constants between the strain gauge signals and reconstructed loads with and without the uA model.

3.5 Conclusions

The objective of the presented dynamic inflow measurements was to deepen the general physical understanding of the dynamic inflow effect for wind turbines.

Direct experimental evidence of dynamic inflow is given through a very clear delay of induction factors at different radial positions at the rotor plane in response to a pitch angle step. Until now, dynamic inflow effects were only proven indirectly through measurements of turbine loads or flow measurements in the wake. It is affirmed that a two-time-constant model is more suited than a one-time-constant model to describe the behaviour of the axial induction for such a pitch step. The fast time constant of this model, representing the near-wake influence, has a strong radial dependency near the root and a clear, respectively slight, dependency in the middle and tip region for the step to high, respectively low, load. The slow time constant, related to the close far wake, shows a slight decrease towards the outer part for the step to low load and a slight increase for the step to high load. The overshooting behaviour of the tangential induction is a novel finding of this work. It could be explained by the shed vorticity, which results from the circulation change during the pitch step. We expect that the radial dependency of the axial induction time constant is related to the observed dynamic wake expansion for the step to low load. With the wake measurement, it is affirmed that the formation of the mixed wake after the pitch step convects faster for the step to low load, than for the step to high load. We suppose that this is the reason for the lower slow time constants of the axial induction for the step to low load. It is found that the mixed wake after the pitch step initially travels at nearly free stream velocity for both pitch directions. We assume that the dynamic inflow effect in this near wake is governed by the tip vortex due to the fast change in trailed vorticity. These vortices travel at such high velocities. Another finding is that the initial decay of the axial inductions during the pitch step is similar for both pitch directions. Furthermore, the aerodynamic characteristics of the turbine is identified to be the reason for the higher load overshoot for the pitch step to low load.

This comprehensive pitch step measurement set allows for detailed validation of engineering models and simulations for two relevant operational states, as we performed with the induction data in *Berger et al. (2020)*.

Further investigations are recommended with high-fidelity models of induction effects, e.g. FVWM or actuator line CFD simulations, to support the interpretation of the data and improvement of models. Further planned steps to extend the understanding of the dynamic inflow process and enhance or develop models on the basis of this experimental setup are the generation of a wider database of pitch steps with varying parameters of inflow velocities, rotor speeds and rotor induction levels but also more realistic inflow conditions, including e.g. non-uniform inflow and gusts. With a wider database it can be tested whether, besides the axial induction, radial position and typical dynamic inflow time scaling factor $\frac{R}{u_0}$ have a significant influence on the time constants, as, for example, the operating TSR, background turbulence or non-uniform inflow. Due to the scaling of induction aerodynamics of this model turbine, based on the NREL 5 MW turbine, the general behaviour of the induced velocities and wake are very similar to that turbine. It thus enables non-dimensional comparisons with that reference turbine, a turbine that has been extensively used worldwide in validation studies.

Appendix

3.A Counterbalance of the blade induction at the bisectrix between consecutive blades

The detailed derivation based on the theorem of Biot–Savart is given in *Herráez et al. (2018)*, but the relevant formulas to produce the analytical solution in Fig. 3.5 a are given here.

Equation (A11) of *Herráez et al. (2018)* is reproduced in Eq. (3.13). The velocity induced by each of the N rotor blades (numbered $i \in [1, 2, \ldots, N]$) is given as a function of the azimuth angle of the blade ψ_i, the azimuth angle of the sampling point β and the coordinates along the blade spanwise direction l. The circulation along the blade span is given by $\Gamma_i(l)$ and the azimuth angle of all blades can be defined by $\psi_i = \psi_1 + (i-1)\Delta\psi$, where $\Delta\psi = \frac{2\pi}{N}$.

$$u_i(r) = \frac{1}{4\pi} \int_0^R \Gamma_i(l) \frac{r \sin(\psi_i - \beta)}{\left[r^2 + l^2 - 2lr\cos(\psi_i - \beta)\right]^{\frac{3}{2}}} \mathrm{d}l \tag{3.13}$$

Herráez et al. (2018) use a phase lock of the rotor for the simulations and compute the velocity along a circle for a specific radius. For the PIV validation in *Herráez et al. (2018)* and the application in this paper, a stationary probe is used and the rotor position is varied. The circulation $\Gamma_i(l)$ is obtained from the lift distribution calculated in Eq. (3.9) by the Kutta–Joukowski theorem.

The analytical solution of the axial probe $u_{\text{probe, analytical}}$ in Fig. 3.5a considers an axial velocity of $u_{\mathrm{ax}} = 4\,\mathrm{m\,s^{-1}}$ and the combined effect of all three blades according to Eq. (3.14). Note that Eq. (3.13) has a singularity for the probe position and a blade element being at the exact same position that are excluded from the plot (90, 210 and 330°).

$$u_{\mathrm{probe,\,analytical}}(r) = \sum_{i=1}^{N} u_i(r) + u_{\mathrm{ax}}(r) \tag{3.14}$$

3.B Unsteady aerodynamics model

The uA model as described in detail in *Pirrung et al. (2017)* Sect. 2.3 is reproduced with slightly altered variable names.

The model consists of two filter functions, Eqs. (3.16) and (3.17), which use the same time constant τ^j_{uA}, defined in Eq. (3.15). The index j denotes the time step, and the index QS the quasi-steady solution. The time step of the simulation, thus reconstruction, is defined by Δt. The effective angle of attack α^j_{eff}, which includes the uA effect, is obtained by Eq. (3.18).

$$\tau^j_{\mathrm{uA}} = \frac{c}{2u^j_{\mathrm{rel}}}, \tag{3.15}$$

$$\begin{aligned} x^j_1 =& x^{j-1}_1 \exp\left(-0.0455\frac{\Delta t}{\tau^j_{\mathrm{uA}}}\right) + \frac{1}{2}\left(\alpha^j_{\mathrm{QS}} + \alpha^{j-1}_{\mathrm{QS}}\right) \\ & 0.165u^j_{\mathrm{rel}}\left(1 - \exp\left(-0.0455\frac{\Delta t}{\tau^j_{\mathrm{uA}}}\right)\right), \end{aligned} \tag{3.16}$$

$$\begin{aligned} x^j_2 =& x^{j-1}_2 \exp\left(-0.3\frac{\Delta t}{\tau^j_{\mathrm{uA}}}\right) + \frac{1}{2}\left(\alpha^j_{\mathrm{QS}} + \alpha^{j-1}_{\mathrm{QS}}\right) \\ & 0.335u^j_{\mathrm{rel}}\left(1 - \exp\left(-0.3\frac{\Delta t}{\tau^j_{\mathrm{uA}}}\right)\right), \end{aligned} \tag{3.17}$$

$$\alpha^j_{\mathrm{eff}} = \frac{1}{2}\alpha^j_{\mathrm{QS}} + \left(x^j_1 + x^j_2\right)/u^j_{\mathrm{rel}}. \tag{3.18}$$

3.C Time constant analysis of wake

The 1c model fit is applied to the hot-wire signal shown in Fig. 3.17. The fit does start at t_0, which is defined at the point where the velocity has adjusted by 28 % to the new equilibrium. This definition is less accurate than the end of the pitch step, as for the axial induction transients. However, no direct fitting start time can be defined and

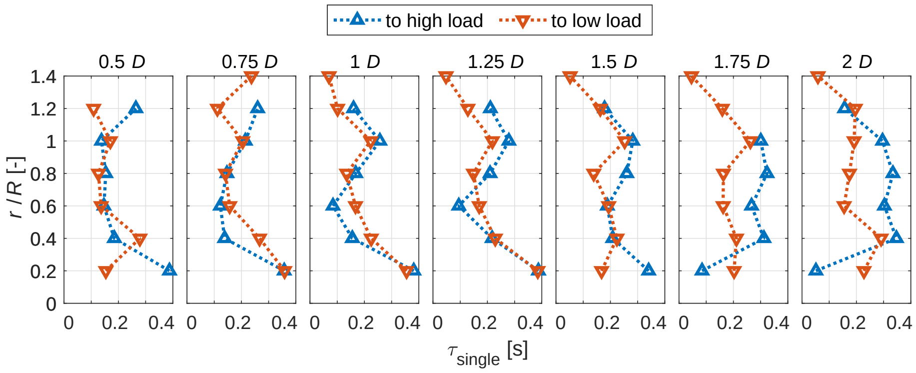

Figure 3.23: Spanwise evolvement of the axial wake velocity from $0.5\,D$ to $2\,D$ parametrized by the fitted time constant of the one-time-constant model for both pitch directions

this value is based on the mean value the axial inductions have adjusted during the pitch step. The aim of this definition is to make the time constants comparable to these time constants of the axial wake induction.

Further, the fitted τ_{single} values for the wake flow measurements are comparable for both pitch directions. They are presented in Fig. 3.23.

Between 0.5 and $1.5\,D$ no clear differences can be seen between pitch directions, apart from the root nearest radius of $0.2\,R$. The fitting of this radius is very sensitive due to the described local structure within the signal and should not be overinterpreted. For farther distances behind the turbine at 1.75 and $2\,D$, there is a clear difference between the pitch directions, with noticeable higher time constants for the step to high load for the radial range of 0.4 to $1\,R$, compared to both the time constants for the step in the same direction at rotor nearer distances and also in comparison to the step to low load at the same distances.

In the actuator disc experiments by *Yu et al. (2017)*, this trend also seems to be more prominent for the higher distances from the actuator disc.

Acknowledgements

This work was partially funded by the Ministry for Science and Culture of Lower Saxony through the funding initiative Niedersächsisches Vorab in the project “ventus efficiens” (reference no. ZN3024). We thank Iván Herráez and Elia Daniele for the discussions on the wake induction measurement method. We further thank Dominik Traphan and Tom Wester for their help with the LDA system. We would also like to thank the two reviewers Luca Greco and Georg Raimund Pirrung for their helpful comments.

Chapter 4

Comparison of a pitch step experiment to mid-fidelity simulations and BEM

The content of this chapter is identical to:

Berger, Frederik, Leo Höning, Iván Herráez and Martin Kühn (2020). 'Comparison of a radially resolved dynamic inflow pitch step experiment to mid-fidelity simulations and BEM'. In: *Journal of Physics: Conference Series* 1618, p. 052055. `DOI`: `10.1088/1742-6596/1618/5/052055`.

Abstract

In this paper a detailed comparison of the experimental and numerical results of a scaled wind turbine model in a wind tunnel subjected to fast pitching steps leading to the so-called dynamic inflow effect is presented. We compare results of an Actuator Line LES tool, a vortex code and four engineering models, to the experiment. We perform one and two-time-constant model analysis of axial wake induction and investigate the overshooting of integral loads. Our results show, that the effect is captured better by the two-time-constant models than by the one-time-constant models. Also the experiment and mid-fidelity simulations are best described by a two-time-constant fit. We identify the best dynamic inflow model to be the Øye model. Different possibilities for the improvement of dynamic inflow models are discussed.

4.1 Introduction

Dynamic inflow is an aerodynamic effect that describes the unsteady response of loads to fast changes in rotor loading. A main reason for dynamic inflow is fast pitching of the rotor blades. This leads to an overshooting of the loads, as the axial wake induction in the rotor plane is not changing instantaneously but only gradually. This effect is usually described in Blade Element Momentum (BEM) codes by engineering models.

For dynamic inflow only few experimental datasets, with limited information on the radial distribution of the induction transients, are available for validation. Within the Joule project (*Snel and Schepers, 1994*) engineering models were tested against pitch step measurements of integral turbine loads of the Tjæreborg turbine (*Øye, 1991*). For the NREL phase VI measurements also the force overshoot at five radial stations was investigated, based on measured pressure distributions *(Schepers, 2007)*. *Yu et al. (2016)* used an actuator disk (AD) which could change the porosity in the wind tunnel for a comparison of the wake flow dynamics to engineering and mid-fidelity models.

The objective of the present work is a comparison of the dynamic induction response after a fast pitch step of a scaled model turbine experiment to two mid-fidelity simulations and four engineering models, thus testing their accuracy and pointing out possible improvements.

4.2 Methods

4.2.1 Experimental data

The dataset of a pitch step experiment with the Model Wind Turbine Oldenburg with 1.8 m diameter (MoWiTO 1.8) (*Berger et al., 2018*), a scaled version of the NREL 5 MW reference turbine, in the large wind tunnel of ForWind - University of Oldenburg *(Kröger et al., 2018)*, is the basis for the comparison. The turbine operated at a wind velocity of $6.1\,\mathrm{ms}^{-1}$ and rotor speed of 480 rpm and was pitched in 70 ms, corresponding to about half a revolution, by 6° from high (thrust coefficient $C_{\mathrm{T,high}} = 0.90$) to low loading (thrust coefficient $C_{\mathrm{T,low}} = 0.48$) and vice versa. The wake inductions in the rotor plane have been obtained by the method proposed by *Herráez et al. (2018)*, based on a one point flow measurement with a 2D Laser Doppler Anemometer (LDA) in the bisectrix between two rotorblades, where blade induction is cancelled out for axisymmetric homogeneuos inflow conditions, as hinted in Fig. 4.1 a and b. A tolerance of ±3° around the bisectrix is assumed for a compromise between data samples and accuracy. These raw wake

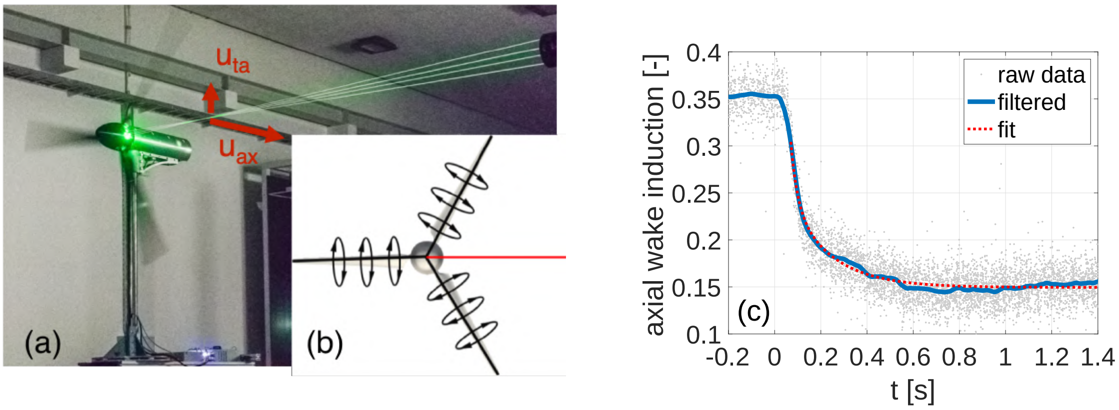

Figure 4.1: (a) Setup with MoWiTO and LDA. (b) Scheme of Herráez method *(Herráez et al., 2018)*. (c) Axial induction transient at $0.7R$ for pitch step from high to low load.

induction results of 100 repetitions of the pitch step from a high to a low turbine loading are plotted in Fig. 4.1 c alongside the filtered signal and an exemplary fit of the signal. These filtered axial induction transients are the basis for the comparison and they are further used as an input to a Blade Element Theory (BET) code, which is based on the also used BEM code described in Sect. 4.2.3. In this BET code the momentum part is deleted and the inductions are taken from the measurements. The geometrical inflow, consisting of axial and tangential velocity at different radii is fed into the BET code, which provides the integral loads used in our analysis. A detailed description and analysis of the experiment is available in *Berger et al. (2021a)*.

4.2.2 Mid-fidelity simulations

Two different kinds of mid-fidelity simulations, both modelling dynamic inflow phenomena intrinsically, are used within this work.

Actuator Line Large Eddy Simulation (AL)

The first simulation environment is the open-source CFD toolbox OpenFOAM and the actuator line method (AL) included in the Simulator fOr Wind Farm Application (SOWFA) by NREL (SOWFA *2019*). In this approach, the forces on the wind turbine rotor are distributed along rotating lines representing the blade loadings. The acting forces are determined using a blade-element approach based on airfoil polars, which are fed into the flow field of a three dimensional Navier-Stokes solver. The flow simulations were conducted using a cubic grid consisting of five different refinement levels as shown in Fig. 4.2 and 4.3 a and b alongside the dimensions, to obtain a higher resolution around the rotor plane and in the near wake in order to better resolve the vortices of the turbine. A total of approx. $19 \cdot 10^6$ cells are used. Three actuator lines replace the three rotor blades, neglecting the influence of the tower and nacelle. To account for the tip and root losses, the 'New Tip Loss Correction Model' presented in *Shen et al. (2005)* was applied to all CFD computations. The sides of the channel have been defined with slip conditions to not influence the flow field. To avoid unphysical oscillations in the force projection, *Sørensen and Shen (2002)* suggest to use a Gaussian approach for smoothing out the forces with increasing distance to the actuator line as:

$$f_i(r) = \frac{F_i}{\varepsilon^3 \pi^{3/2}} \exp\left(- \left(\frac{r}{\varepsilon} \right)^2 \right), \tag{4.1}$$

with f_i being the force field projected onto the CFD grid and F_i the load for each blade at the actuator line elements (in our case 40). The distance to the respective actuator line element is given by r, while ε controls the Gaussian width. The stability of the simulation is directly related to the ratio of the Gaussian width and the mesh resolution Δx in the area swept by the actuator lines. It was found, that $\frac{\varepsilon}{\Delta x} = 5$ provides a good compromise between stability of the simulation and physicality of the force distribution along the blades (in agreement to *Martínez-Tossas et al., 2015*).

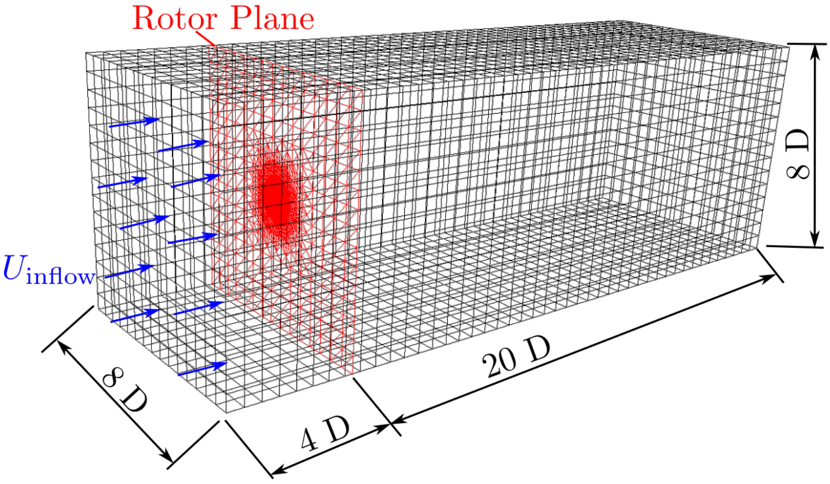

Figure 4.2: Dimensions of the cubic mesh (reduced cells).

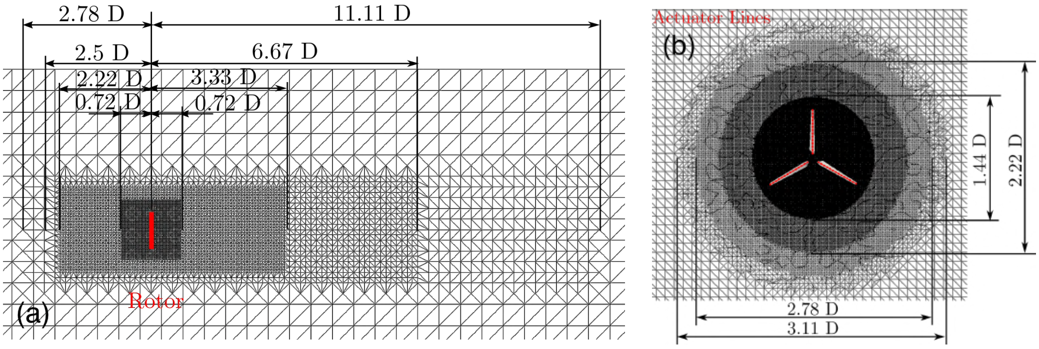

Figure 4.3: (a) Top view of refinement levels (reduced cells). (b) Front view (reduced cells).

Free Vortex Wake Method Lifting Line Theory (FVWM LLT)

The second simulation environment is a FVWM LLT (LLT) code implemented in QBlade *(Marten et al., 2016)*, based on the principles in reference (*Van Garrel, 2003*). The flowfield is assumed to be inviscid, incompressible and irrotational and is modelled as a potential flow. The blade is discretised in elements and modelled by a bound ring vortex per element, thus forming the lifting line. The circulation of the bound vortices is calculated iteratively based on the airfoil polars and relative velocity. The induced velocity is influenced by all present vortex elements. The vorticity is shed and trailed in each time step and convected, thus forming the wake. A first order method for forward integration of the wake convection is used. Twelve revolutions in the wake are considered, whereas the first six revolutions have a higher resolution than the last six, giving 6831 vortex elements at an azimuthal step of 10°. The initial core size is 4 mm, being 10 % of the chord length of the tip.

4.2.3 Engineering dynamic inflow models in Blade Element Momentum theory (BEM)

In addition to the mid-fildelity models also dynamic inflow engineering models are considered. These are the Øye (*Snel and Schepers, 1994*), ECN (*Snel and Schepers, 1994*) and recent DTU (*Madsen et al., 2020*) dynamic inflow models, implemented in an in-house MatLab BEM code. The BEM code is based on the steady implementation described in detail in *Hansen (2008)* with the 'high thrust' correction by Spera and the Prandtl tip loss correction model. The code is put in a time marching manner and three dynamic inflow models are implemented. Further the generalised dynamic wake model (GDWM), an extension of the Pitt-Peters dynamic inflow model, implemented in FAST v7 (*Jonkman and Buhl, 2005*) is considered. All simulations are purely aerodynamic. In the following the different engineering models are described.

ECN model

The dynamic inflow model developed by ECN is based on an integral relation derived from a simplified cylindrical vortex wake sheet model *(Snel and Schepers, 1994)*. For a constant inflow wind velocity v_0 the differential equation is shown in Eq. (4.2). C_t is the thrust force coefficient on a blade annulus at radius r. The term f_A is a function of the radial position and given by Eq. (4.3). The single time constant τ is adjusted to the turbine size by the rotor radius R.

$$\frac{R}{u_0} f_A(r) \frac{da(r)}{dt} + a(r)(1-a(r)) = \frac{C_t(r)}{4} \quad \text{where} \quad \tau(r) = \frac{R}{u_0} f_A(r) \tag{4.2}$$

$$f_A(r) = 2\pi / \int_0^{2\pi} \frac{[1-(r/R)\cos(\phi_r)]}{[1+(r/R)^2 - 2(r/R)\cos(\phi_r)]^{3/2}} d\phi_r \tag{4.3}$$

Generalised Dynamic Wake Model (GDWM)

The GDWM is an extension of the Pitt and Peter's model. The model is based on a potential flow solution to Laplace's equation, leading to a smooth distribution of the axial induction, based on polynomials (*Suzuki and Hansen, 1999*). The GDWM models the effect of tip losses, skewed wake and dynamic inflow effects. Dynamic inflow is considered by an apparent mass that leads to the time lag in the induced velocities. The model and implementation to AeroDyn v14, used in FAST v7 *(Jonkman and Buhl, 2005)*, is explained in detail in *Moriarty and Hansen (2005)*. The GDWM is no longer used in the current versions FAST v8 and openFAST.

Øye model

The Øye dynamic inflow model estimates the induced velocities in the rotor plane by filtering the steady values through two first order differential equations in Eq. (4.4) (*Snel and Schepers, 1994; Hansen, 2008*).

$$W_{int} + \tau_1 \frac{dW_{int}}{dt} = W_{qs} + k \cdot \tau_1 \frac{dW_{qs}}{dt} \quad , \quad W = \tau_2 \frac{dW}{dt} = W_{int} \tag{4.4}$$

W_{qs} is the quasi-steady induced velocity, W_{int} an intermediate and W the final filtered induced velocity. The time constants and ratio k were calibrated through an AD vortex ring model:

$$\tau_1 = \frac{1.1}{(1-1.3a)}\frac{R}{V} \quad , \quad \tau_2 = \left[0.39 - 0.26\left(\frac{r}{R}\right)^2\right]\tau_1 \quad , \quad k = 0.6 \tag{4.5}$$

DTU model

The most recent DTU dynamic inflow model is described in *Madsen et al. (2020)*. Similar to the Øye model two first order time constants are used (Eq. 4.6).

$$u_{av} = u - \Delta u\left[0.5847\cdot\exp\left(-t\frac{f_1}{\tau_1}\right) + 0.4153\cdot\exp\left(-t\frac{f_2}{\tau_2}\right)\right] \tag{4.6}$$

$$\text{with} \quad f_1 = 1 - 0.50802\cdot a_{Req} \quad , \quad f_2 = 1 - 1.9266\cdot a_{Req} \tag{4.7}$$

u is the axial velocity in the rotor plane at a specific radius. u_{av} is the filtered flow speed and f_1 and f_2 are functions to adapt the time constants to the local flow speed. The axial induction factor a_{Req} in (4.7) is the rotor equivalent induction in our implementation, following a discussion with an author of *Madsen et al. (2020)*. The time constants were tuned through an AD-CFD simulation:

$$\tau_1 = \left[-0.7048\left(\frac{r}{R}\right)^2 + 0.1819\frac{r}{R} + 0.7329\right]\,[\mathrm{s}] \tag{4.8}$$

$$\tau_2 = \left[-0.1667\left(\frac{r}{R}\right)^2 + 0.0881\frac{r}{R} + 2.0214\right]\,[\mathrm{s}] \tag{4.9}$$

4.2.4 Time constant analysis

The induction transients are investigated by a one-time-constant analysis as used by *Schepers (2007)*. The exponential function Eq. (4.10) is fitted to the induction transient with the start point $t_0 = 70\,\mathrm{ms}$ directly after the pitch step is terminated. a_{t0} is the axial induction at time t_0 and $\Delta a = a_{t0} - a_\infty$, with a_∞ beeing the new steady value of the axial induction. The time constant τ is obtained by a least square error fit of the function to the signal $([t_0, 0.8\,\mathrm{s}])$.

$$a(t) = a_{t_0} - \Delta a\cdot\left(1 - \exp\frac{(t_0 - t)}{\tau}\right) \tag{4.10}$$

Further the axial induction transients of the experiment, mid-fidelity simulations and the Øye and DTU engineering models are assessed by time constant investigations with a two-time-constant fit (Eq. 4.11), with the ratio k, to the axial induction a, as proposed in *Sørensen and Madsen (2006)*.

$$a(t) = a_{t_0} - \Delta a \cdot \left((1-k) \cdot (1 - \exp \frac{(t_0 - t)}{\tau_{fast}}) + k \cdot (1 - \exp \frac{(t_0 - t)}{\tau_{slow}}) \right) \tag{4.11}$$

4.3 Results

4.3.1 Steady induction

In Fig. 4.4 the annulus averaged axial induction is plotted over the radius for the stationary cases at high load (left) and low load (right) for the described models. Referring to the method of Herráez et al. *Herráez et al. (2018)* the measurement points at 0.3 R and 0.95 R should be treated with care because of their proximity to the blade root and tip, but we decided to still include them in the investigation. The BEM, AL and LLT simulations are very similar for radii 0.3 R to 0.9 R with some differences, especially of the LLT, in the tip and root region for both and the AL at the tip for the low load case. The experimental measurement is in good agreement with these from 0.6 R to 0.9 R and has a higher induction for both cases for 0.4 R - 0.5 R. For the GDWM implemented in the outdated FAST v7 the axial inductions were converted to annulus averaged inductions in post processing for better comparability by multiplying the inductions by the respective Prandtl tip loss factor. The induction for the high load case shows significant differences to the experiment and the other simulation cases. The values at low radii up to 0.6 R are lower, whilst the values from 0.6 R to the tip are higher. For the low load case, the match is good, apart from the root region up to 0.3 R, where the inductions are estimated to be lower.

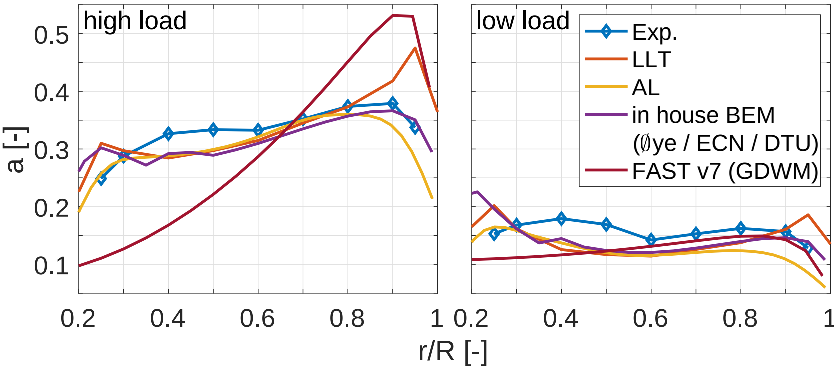

Figure 4.4: Axial induction over radius for the experiment and numerical models.

4.3.2 One-time-constant analysis of induction transients

The axial induction transients for the pitch step to low load are plotted in Fig. 4.5 for the three radii at 0.3 R, 0.6 R and 0.9 R in a non-dimensioned form, where equalling to 1 before the transient (induction a_1) and equalling to 0 after the transient (induction a_2). For the case of the GDWM this form is slightly altered to a_1 being the maximum axial induction, as this model models a clear overshooting of induction in contrast to the other models. For the experiment and the mid-fidelity models a clear difference is obvious between the non-dimensioned induction transients at 0.3 R and those at 0.6 R and 0.9 R, where the 0.3 R case has an initially slower decay indicating a radial dependence. Also differences between the decay time are already obvious by visual inspection, when comparing the GDWM to the LLT.

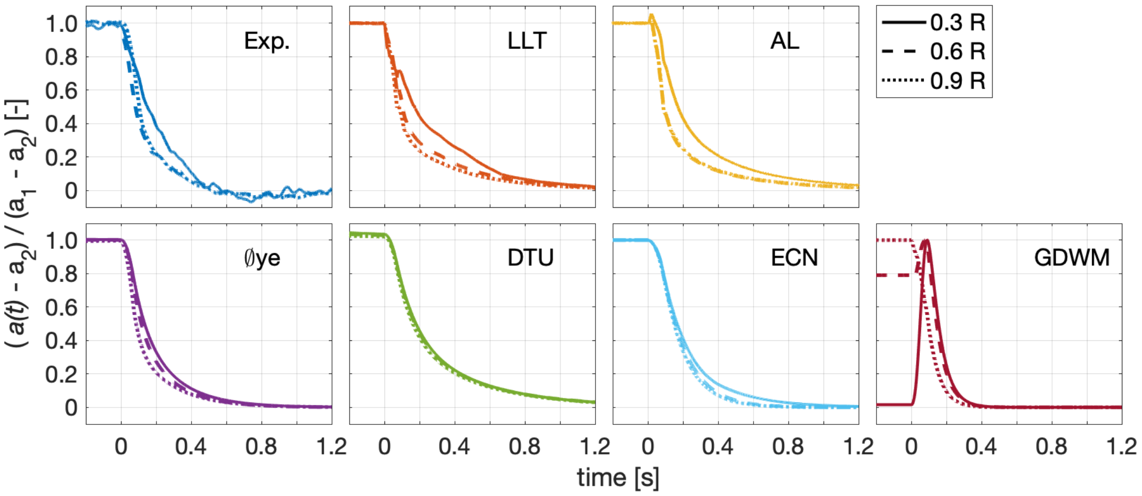

Figure 4.5: Induction for step to low load: experiment, LLT, AL and Øye at different radii.

In Fig. 4.6, the fitted time constant τ for the one-time-constant approach is plotted over the radius for the different cases for the pitch step to high (left) and low (right) loads.

For both pitch directions the AL and Øye model give results very close to the experiment. The LLT and DTU model have higher values than the experiment for both step directions, with similar results for the step to low load and the LLT also having higher values than the DTU model for the step to high load. The LLT, AL and experiment have no linear radial trend along the radius for the step to high load and a slight trend to lower time constants towards the tip for the step to low load. The LLT and AL show an increase of the time constant at the very tip for both pitch directions. The

ECN model has for both pitch directions a similar time constant course with strongly decreasing values towards the tip. For the step to high loads the time constant is lower than the experiment over the whole blade with increasing difference towards the tip. For the step to low load the ECN model fits the experiment well for radii up to 0.7 R and then the difference is increasing due to the strong decrease of the ECN time constant towards the tip. The GDWM shows the lowest time constants with an increase towards higher radii for the step to high loads and the opposite behaviour for the step to low load.

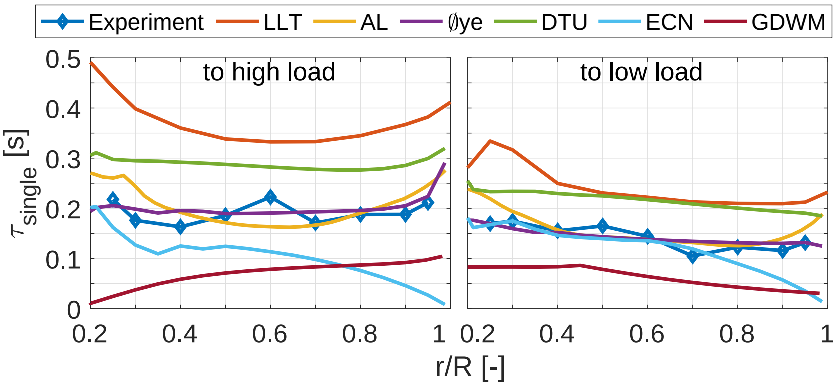

Figure 4.6: Single time constant over radius for the experiment, two mid-fidelity models and four engineering models. Pitch step to high load (left) and to low load (right).

4.3.3 Two-time-constant analysis of induction transients

In Fig. 4.7 the fitting results for the two-time-constant analysis are presented for the experiment, the two mid-fidelity codes (AL and LLT) and the two engineering models based on two time constants (Øye and DTU) for the step to high load (top) and to low load (bottom). Additionally the analytical values used for the Øye model in the BEM code are pesented as a measure of accuracy for the fitting approach. Comparing the k-value present a wide spread of the values between models for both pitch directions. The experiment gives a generally higher k-ratio than the simulations, with higher values towards the root. The AL and DTU model show values around $k \approx 0.5$ for both pitch directions, thus having a similar contribution of fast to slow time constant for the decay process. The LLT model seems to be closest to the experiment but generally at lower k values followed by the Øye model. For τ_{fast} the experiment has higher values near the root and then between 0.4 R while for the tip lower values than all simulations for both pitch directions are observed. The AL and LLT models also show an increase of

τ_{fast} towards the root for the step to low loads, similar in trend to the experiment. The engineering models of Øye and DTU both have a decreasing trend towards the tip, apart from the very tip for the Øye at the step to high load, at generally higher τ_{fast} than the experiment. There is no clear general difference of τ_{fast} obvious in Fig. 4.7 between the pitch directions for the experiment and the mid-fidelity models, whereas the engineering models are by design slightly faster for the step to low load. The slow time constant τ_{slow} has no clear radial dependence for the experiment with a slightly lower value for the step to low load. The LLT and DTU model show also a flat trend at about three times the value for the step to high load and two times for the step to low load compared to the experiment. The AL also has a flat trend and its values are between the LLT and experiment, also showing a lower value for the step to low load. The Øye model is similar to the experiment apart from the step to high load towards the tip, where τ_{slow} increases due to the local high axial induction (before applying the tip correction). The analytical values of the Øye model indicate a good quality of the fit for the time constants and slightly higher deviations for the k-ratio.

In Fig. 4.8, the same fitting results are plotted, however here the k-ratio is set to 0.79, which is the mean value of the experiment considering both pitch directions, for all cases. This approach increases the comparability between the cases on the cost of the fitting accuracy. The general behaviour of the experiment matches that of the fitting with a fitted k-ratio as in Fig. 4.7. For τ_{fast} the LLT matches the experiment with slightly higher values for the step to high load, but also capturing the increase torwards the root, especially for the step to low load. The AL also has an increase towards the root but general lower values than the experiment, especially near the root for the step to low load. The Øye and DTU models do not have the increase towards the root and decrease in a linear fashion towards the tip, with the exception of the very tip of the Øye model for the step to high load. For the step to low loads, the two engineering models are nearly coincident for the step to low load, whereas the Øye model has higher values than the DTU model for the step to high load. For τ_{slow} for all cases, the step to low load gives lower values than the one to high loads. Further all cases for both pitch directions show no clear radial dependency, but especially for the LLT for the step to high load and also for the AL for both step directions τ_{slow} increases towards the tip and root. The Øye model is in good agreement with the experiment for both pitch directions and so is the AL, apart from the very root region. The DTU model gives higher time constants and the LLT even higher ones, especially for the step to high load.

In Fig. 4.9 the root mean square error (RMSE) for the fitting of the section at $0.6\ R$, describing how good the fit represents the data it is fitted to, is plotted for the single

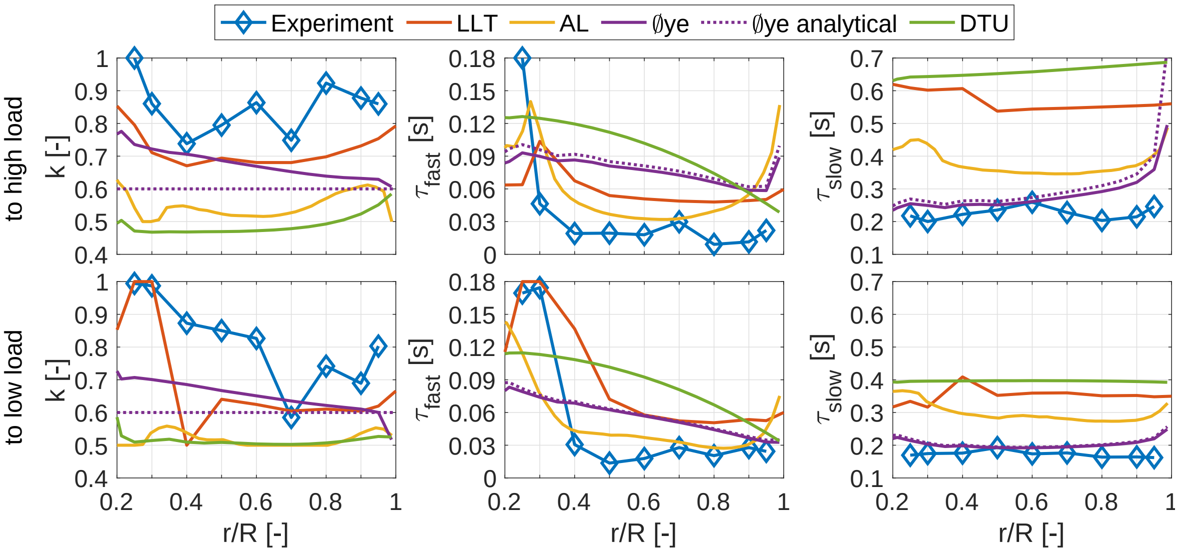

Figure 4.7: Comparison of two-time-constant fit τ_{fast} and τ_{slow} of the axial induction between experiment, LLT, AL, Øye and DTU. The k-value is also a free variable in the fitting.

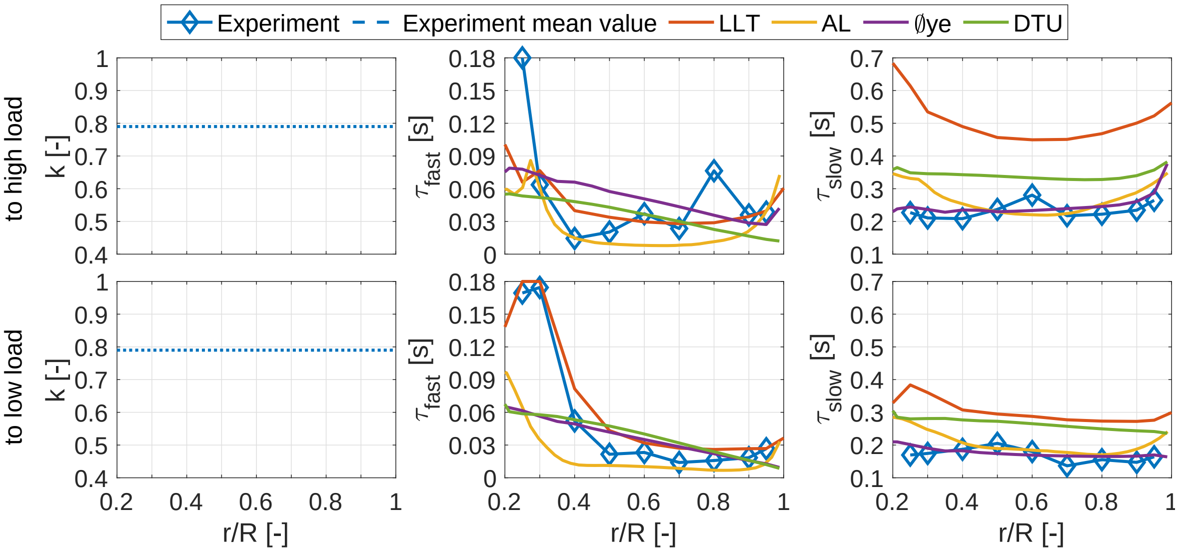

Figure 4.8: Comparison of two-time-constant fit τ_{fast} and τ_{slow} between experiment, LLT, AL, Øye and DTU model for a prescribed k-value.

(τ_{single}) and the two variants of the two-time-constant analysis ($\tau_{2c,k=var}$ and $\tau_{2c,k=0.79}$) for the experiment, mid-fidelity models (AL and LLT) and two-time-constant engineering models (Øye and DTU). The error for the experiment is highest for the τ_{single} fit and lowest for the $\tau_{2c,k=var}$ fit, with the $\tau_{2c,k=0.79}$ case being slightly higher than the former. It should be noted that the RMSE of the experiment is also influenced by noise, which is not the case for the simulations and engineering models. The same holds true for the AL and LLT, however with a bigger difference between the two variable fits. For the Øye and DTU model, the error for $\tau_{2c,k=var}$ approaches zero as should be by design on these models. The error for the described k-value for the Øye model still is very low whereas it is higher for the DTU model.

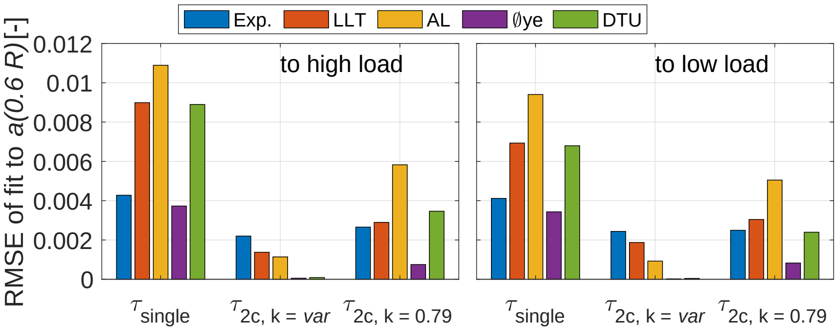

Figure 4.9: Comparison of root mean square error of the one and two component fits to the respective axial wake inductions at 0.6 R for experiment, simulations and models from t_0 to 0.8 s.

4.3.4 Load overshoot analysis

The aerodynamic rotor torque, flapwise blade root bending moment and thrust are plotted for the experiment and the simulations for the step to low load in Fig. 4.10. The overshoot is defined as the difference between the maximum peak for pitch to high load, respectively minimum peak for pitch to low load, at $t_0 = 70\ ms$ and the new steady value long after the pitch step at t_∞. The steady values of these loads of the simulations generally are close to the experiment with relative deviations to it by 3 % to 11 % for the LLT, 1 % to 7 % for the AL, −4 % to 4 % for the in-house BEM (Øye, DTU and ECN) but considerably higher deviations for the FAST v7 model with −13 % to 16 %. Similar to the pure axial induction plot (Fig. 4.4), a clear difference can be seen between the GDWM model and e.g. the LLT. The GDWM adapts much faster to the new steady value, but also shows a lower overshoot.

The overshoot is plotted in Fig. 4.11 normalised with the value of the experiment

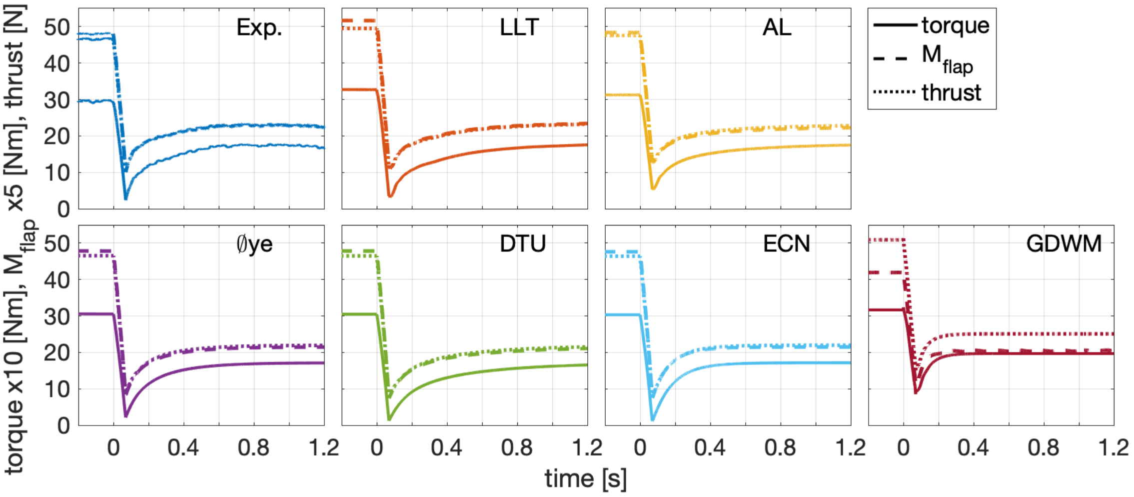

Figure 4.10: Loads for experiment (BET based), LLT, AL and engineering models Øye, DTU and ECN implemented in an own BEM code and the GDWM in FAST v7.

for the simulations for both pitch directions. Considering all three load sensors, AL and DTU predict the overshoot for the step to high load best, whereas the first slightly underpredicts and the second slightly overpredicts. The Øye model is similar to the DTU model and only marginally worse. The LLT and GDWM overpredict the overshoot for single loads by more than 20 %, whereas the ECN model underpredicts single loads by nearly 20 %. For the step to low load the LLT performs best, closely followed by the Øye model. DTU and ECN model perform similar and overpredict slightly by 9 % to 15 %. The AL underpredicts the overshoot by up to 20 % and the GDWM even by up to 23 %. Overall the Øye model estimates the overshoot closest to the experiment, closely followed by the DTU model.

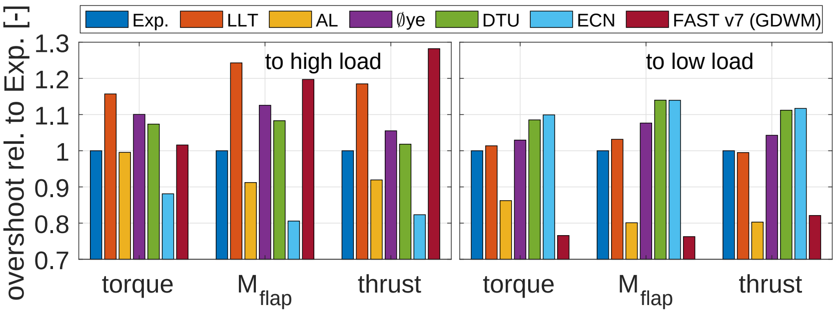

Figure 4.11: Absolute overshoot of simulations and model normalised by the absolute overshoot of the experiment for both pitch directions.

4.4 Discussion

The good agreement of the steady axial inductions for the high and low load cases between the experiment, obtained with the Herráez method (*Herráez et al., 2018*), the mid fidelity simulations and the in house BEM code allows for the further detailed comparison of the dynamic behaviour between those two load states due to pitch steps. The GDWM implemented in the FAST v7 version does not match well for the stationary high load case, being a general issue with this model as discussed in *Suzuki and Hansen (1999)*.

The faster decay for the step to low load as observed by *Schepers (2007)* for the NASA Ames experiment is also seen in the one-time-constant investigation of the experiment, LLT and AL and caught by the Øye and DTU models but not the GDWM and ECN model.

The two-time-constant comparison with a free k-ratio of time constants indicates the difficulty of comparing the different models with three parameters. The choice of fixing the ratio k of the time constants enabled us to compare these at a justifiable cost in fitting error. The high τ_{fast} values for experiment, LLT and AL towards the root for the step to low load are not mapped by the Øye and DTU model. The LLT predicts the τ_{fast} value close to the experiment, while the τ_{slow} value is overestimated, especially for the step to high load. We do suspect that tuning of the wake convection is a possible improvevement here. The AL simulation does show a good agreement with the experiment for the one-time-constant investigation and the τ_{slow} value of the two-time-constant investigation with prescribed k-value, but the τ_{fast} values are underestimated. A tuning of the Gaussian width in the swept area of the AL could be an improvement here. Further we also see considerable room for improvement in the modelling of tip losses. The error comparison for the experiment, LLT and AL fits showed, that the dynamic inflow effect should be described by two-time-constants, as discussed by *Sørensen and Madsen (2006)*. The radial dependence obvious by visual inspection for the inductions in Fig. 4.5 of experiment and mid-fidelity models was not captured in the one-time-constant analysis but in the two-time-constant analysis in τ_{fast}.

In the load study the LLT, Øye and DTU model overpredict the overshoot whereas the AL underpredicts it. The one-time-constant models however both overpredict one direction and underpredict the other, thus seeming less reliable. The differences also are connected to the two time constants, e.g. the underestimated τ_{fast} of the AL leading to the underprediction of the step to low load and the strongly overestimated τ_{slow} value of the LLT leading to the overprediction of the overshoot for the step to high loads, as the overshoot at t_0 depends on the axial velocity in the rotor plane and by how much it has already adapted to the new equilibrium.

4.5 Conclusions

The investigation showed, that of all the engineering models, the Øye model performed overall closest to the experimental pitch case, followed by the DTU model. The Øye model is currently implemented in OpenFAST 2.0 and GH Bladed and the DTU model in HAWC2 12.8. The tested models based on a single time constant cannot be recommended. The comparison of the mid-fidelity models with the experiment indicated general good performance but also specific weaknesses, which should be considered for simulations with such tools where dynamic inflow phenomena or the wake dynamics due to load changes are of importance.

Acknowledgement

This work was partially funded by the Ministry for Science and Culture of Lower Saxony through the funding initiative Niedersächsisches Vorab (ventus efficiens). We thank Olga Belenda Álvarez for a pre-study on the Øye and GDWM model. We further thank Georg Raimund Pirrung for the discussion on the new DTU dynamic inflow model.

Chapter 5

Experimental analysis of the dynamic inflow effect due to coherent gusts

The content of this chapter is identical to:

Berger, Frederik, Lars Neuhaus, David Onnen, Michael Hölling, Gerard Schepers and Martin Kühn (2022). 'Wind tunnel analysis of dynamic inflow effects due to rotor uniform gusts'. In: *Wind Energy Science* 7.5, pp. 1827–1846. `DOI`: `10.5194/wes-7-1827-2022`.

Abstract

The dynamic inflow effect describes the unsteady aerodynamic response to fast changes in rotor loading due to the inertia of the wake. Fast changes in turbine loading due to pitch actuation or rotor speed transients lead to load overshoots. The phenomenon is suspected to be also relevant for gust situations; however, this was never shown, and thus the actual load response is also unknown. The paper's objectives are to prove and explain the dynamic inflow effect due to gusts, and compare and subsequently improve a typical dynamic inflow engineering model to the measurements. An active grid is used to impress a 1.8 m diameter model turbine with rotor uniform gusts of the wind tunnel flow. The influence attributed to the dynamic inflow effect is isolated from the comparison of two experimental cases. Firstly, dynamic measurements of loads and radially resolved axial velocities in the rotor plane during a gust situation are performed.

Secondly, corresponding quantities are linearly interpolated for the gust wind speed from lookup tables with steady operational points. Furthermore, simulations with a typical blade element momentum code and a higher-fidelity free-vortex wake model are performed. Both the experiment and higher-fidelity model show a dynamic inflow effect due to gusts in the loads and axial velocities. An amplification of induced velocities causes reduced load amplitudes. Consequently, fatigue loading would be lower. This amplification originates from wake inertia. It is influenced by the coherent gust pushed through the rotor like a turbulent box. The wake is superimposed on that coherent gust box, and thus the inertia of the wake and consequently also the flow in the rotor plane is affected. Contemporary dynamic inflow models inherently assume a constant wind velocity. They filter the induced velocity and thus cannot predict the observed amplification of the induced velocity. The commonly used Øye engineering model predicts increased gust load amplitudes and thus higher fatigue loads. With an extra filter term on the quasi-steady wind velocity, the qualitative behaviour observed experimentally and numerically can be caught. In conclusion, these new experimental findings on dynamic inflow due to gusts and improvements to the Øye model enable improvements in wind turbine design by less conservative fatigue loads.

5.1 Introduction

The dynamic inflow phenomenon is an unsteady aerodynamic effect relevant for helicopters *(Peters, 2009)* and wind turbines *(Snel and Schepers, 1994)*. It is considered for a fast load variation through a blade pitch step or fast change in rotor speed. Due to the inertia of the wake, the induced velocity cannot change instantaneously but only gradually to a fast load event in the rotor plane. This dynamic transition in the wake leads to load and power overshoots between the two steady states. For wind turbines, *Snel and Schepers (1994)* also suspect variations in inflow velocity, especially due to coherent wind gusts, to lead to relevant dynamic inflow effects.

Aeroservoelastic simulations are used to obtain relevant turbine loads in the design and certification process of wind turbines. The aerodynamic part of these simulations is based on the blade element momentum (BEM) theory that gives the aerodynamic forces acting on the rotor blade segments. BEM, however, is inherently based on steady-flow assumptions, and engineering models are needed to catch dynamic phenomena, like the dynamic inflow effect. Widely used examples are the ECN model *(Snel and Schepers, 1994)* in Phatas and the ECN (now TNO) Aero-Module, the recent DTU model (*Madsen et al., 2020*) in HAWC2, and the Øye model *(Øye, 1986; Øye, 1990; Snel and Schepers, 1994)* in GH Bladed and OpenFAST. They all have the main working mechanism that they filter the induced velocity based on time constants. One time constant is used for the ECN model and two time constants for the DTU and Øye model.

In addition to the need of engineering models for dynamic inflow effects, blade element momentum (BEM) theory is based on the assumption of axial and uniform inflow. Free-vortex wake methods (FVWMs) on the other hand model dynamic inflow effects and also non-uniform inflow intrinsically. *Boorsma et al. (2020)* looked at the influence of turbulent wind fields with shear on the loading of wind turbines. They found relevant lower fatigue loading for the out-of-plane blade root bending moments and tower bottom fore–aft bending moment for the higher-fidelity FVWM-type simulations, compared to BEM-type simulations. The implementation of how non-uniform inflow influences the induced velocities over one rotation in BEM was identified as one relevant contribution to this behaviour; however, they also suspected the dynamic inflow effect to be responsible for some of the differences between BEM and FVWM in turbulent inflow.

Within two historic EU projects on dynamic inflow *(Snel and Schepers, 1994; Schepers and Snel, 1995)* a 1.2 m diameter model wind turbine was exposed to a step change in wind velocity generated by a manually operated gust generator in a wind tunnel. This experiment did not observe a dynamic inflow effect due to gusts. *Snel and Schepers (1994)* related this to the slow step change in wind velocity, compared to the typical dynamic inflow time constant. BEM-based simulations with engineering models suggested a slight load overshoot for the investigated case. *Shirzadeh et al. (2021)* investigated dynamic load and power characteristics due to extreme shear and gusts based on tower base force and power measurements. They used a 2.2 m diameter model wind turbine with very low design tip speed ratio and constant generator resistance in the WindEEE Dome. They exposed it to a gust, where the wind velocity increased from 5 to 9 $\mathrm{m\,s^{-1}}$ and back again within 5 s. They did not look specifically into the dynamic inflow phenomenon, and an effect is also not clearly indicated in the presented plots.

Until now, there is no conclusive information on the relevance or even existence of dynamic inflow effects due to gusts. Consequently, it is also not known if current engineering models can model this expected effect.

The objective of this work is to experimentally prove and quantify the dynamic inflow effect due to gusts and to investigate the behaviour in engineering models. The work continues and builds on the methods of the radially resolved induction factor measurements of a pitch step experiment in *Berger et al. (2021a)* and the comparison of that experiment to engineering models in *Berger et al. (2020)* but here for gusts. An active

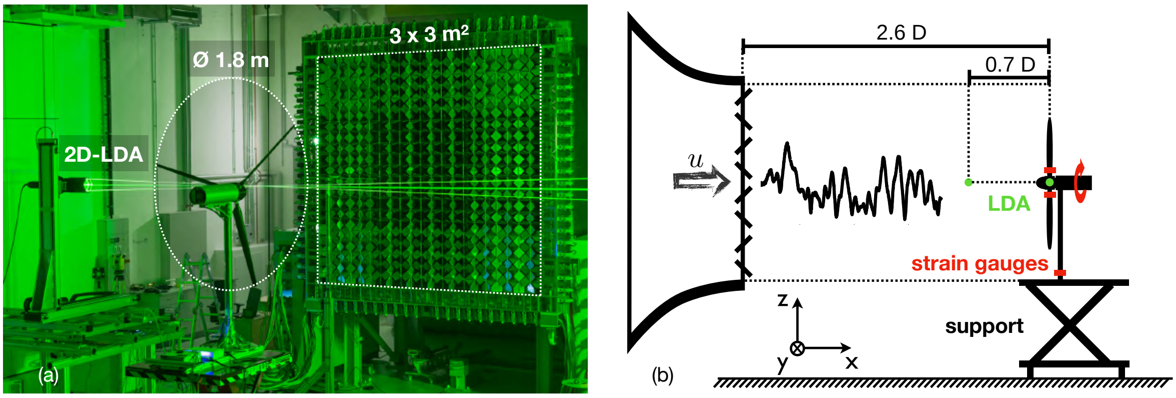

Figure 5.1: (a) Picture of MoWiTO 1.8 and 2D-LDA in a wind tunnel with active grid. Note the visible shift of grid flap angles between the centred inner square and outer compensating axes, demonstrated in the picture for a smaller inner square part than used in the investigation. (b) Schematic of setup with coordinate system in the wind tunnel.

grid is used in the wind tunnel to create coherent gust situations. Two experimental cases are compared to extract the dynamic inflow effect due to a gust, as the difference between those cases. The first case is a dynamic measurement of loads and axial velocity in the rotor plane. Secondly, a quasi-steady measurement is emulated by interpolation from a detailed experimental characterisation of loads and axial velocity, based on the gust velocity. An enhancement for gusts is proposed based on analytical assumptions for engineering models and implemented for the Øye dynamic inflow model. The dynamic inflow behaviour due to gusts of the original and the gust-improved Øye dynamic inflow model and a FVWM are compared to the experimental behaviour.

5.2 Methods

Within this study various methods are combined, and a short overview of the methods is given as a guideline. Firstly the experimental setup is introduced (Sect. 5.2.1). In the following the gusts are quantified (Sect. 5.2.2). In the measurement matrix, all measurement cases, positions and repetitions are outlined (Sect. 5.2.3). Moving forward, the wake induction measurements and the additional load reconstruction from the flow measurements are introduced (Sect. 5.2.4). The construction of the dynamic (Sect. 5.2.5) and the quasi-steady (Sect. 5.2.5) case is described in the next step. Next, the concept of dynamic inflow engineering models is outlined, and an enhancement for gust situations is proposed (Sect. 5.2.6). In the last part, the simulation models for BEM and FVWM are presented (Sect. 5.2.7).

5.2.1 Experimental setup

Wind tunnel

The experiments were performed in the large wind tunnel of ForWind – University of Oldenburg. The Göttingen-type wind tunnel has an outlet section of 3 m by 3 m. The wind tunnel was operated in an open-jet test section configuration with a test section length of 30 m (maximum wind velocity of $32\,\mathrm{m\,s^{-1}}$). The wind tunnel is described in more detail in *Kröger et al. (2018)*.

Active grid

An active grid is attached to the wind tunnel nozzle to manipulate the flow *(Kröger et al., 2018; Neuhaus et al., 2021)*. The grid consists of 80 individually controllable shafts with rectangular flaps to control the distribution of blockage of the flow. Thus, wind variations can be repeatedly generated, as shown by *Kröger et al. (2018)*. The active grid is shown in Fig. 5.1a.

Model turbine

The Model Wind Turbine Oldenburg with a diameter (D) of 1.8 m (MoWiTO 1.8) is used for the investigation (see Fig. 5.1a). The turbine is aerodynamically scaled based on the NREL 5 MW reference turbine *(Jonkman et al., 2009)* and maintains the design tip speed ratio (TSR; 7.5), thrust and power characteristics, and the non-dimensional lift and thus induction distribution. The turbine blades are scaled by a geometrical factor of $n_{\text{length}} = \frac{1}{70}$. Influenced by structural constraints, the time scaling of the design is $n_{\text{time}} = 50$. This leads to n_{time}-times-faster rotor speeds, $\frac{1}{n_{\text{time}}}$-times-shorter gust length, and a factor of $n_{\text{time}} \cdot n_{\text{length}}$ on the wind velocity. Low Reynolds number profiles are used for the stiff carbon-fibre-made blades. The blades have an estimated maximum tip deflection of less than 0.015 m at the maximum wind velocity ($8.6\,\mathrm{m\,s^{-1}}$) in this study and a first eigenfrequency of 32 Hz. The turbine has no rotor tilt or blade coning. It features individual pitch motors, torque control, and encoders for rotor rotation and position. Further, strain gauges for flapwise blade root bending moment, rotor torque and tower bottom bending moment (to derive the rotor thrust) are used. The turbine position in the wind tunnel is shown in Fig. 5.1b. Along the distance of 2.6 D behind the wind tunnel nozzle, the induction zone of the turbine can freely develop (see *Medici et al., 2011*). The turbine control and data acquisition are handled by a National Instruments CompactRIO system. The turbine scaling and design are described in detail in *Berger et al. (2018)*.

Laser Doppler anemometer

A 2D laser Doppler anemometer (LDA) by TSI Inc., with a beam expander with a focus length of 2.1 m, is used. The optical measurement device is placed well outside of the wind flow. It is mounted on a motor-driven three-directional traverse with 1.5 m travel distance in each direction (see Fig. 5.1a). A LDA has no fixed sampling frequency but depends on various parameters, including the seeding of the wind flow with small oil particles. Typical LDA sampling frequencies in this experiment are 2 kHz.

5.2.2 Wind fields

In this research the active grid is controlled by an overall constant blockage approach, where the inner square part (2 m by 2 m) of the grid impresses the desired gust conditions. The outer axes are used to keep the mean blockage of the grid constant. This way, fast velocity fluctuations with a high amplitude and degree of coherence can be achieved *(Neuhaus et al., 2021)*. Two different types of transient wind fields with a high coherence over the swept area of the turbine are designed for this study. The wind tunnel fans are operated at constant speed, and the velocity patterns are impressed by the flaps of the active grid. The first wind field is based on a continuous sinusoidal wind velocity variation (sine) with a frequency of 1 Hz, mean wind velocity of $6.4\,\mathrm{m\,s^{-1}}$ and an amplitude of $1.8\,\mathrm{m\,s^{-1}}$. The second wind field has effectively 20 s of stochastic variations (stochastic), with a mean wind velocity of $6.2\,\mathrm{m\,s^{-1}}$, maximum value of $8.6\,\mathrm{m\,s^{-1}}$ and minimum value of $4.4\,\mathrm{m\,s^{-1}}$.

The wind fields are quantified based on LDA measurements at 15 positions $0.7\,D$ upstream of the turbine at standstill. The streamwise position of the measurements is indicated in Fig. 5.1b. The positions are located in a y–z plane (parallel to rotor plane). We measure on a horizontal ($-y$ direction) and diagonal line ($-y$ and $-z$ direction) starting from the centreline of the wind tunnel in steps of 0.2 to $0.8\,R$ and finer step width of $0.1\,R$ from 0.8 to $1.1\,R$, where R is half of the rotor diameter D. Due to the symmetry of the square grid, the measurement points within the considered quarter of the rotor give a good representation of the whole swept area. For the sine variation 40 repetitions are considered, and for the stochastic variation 10 repetitions per position are considered.

These measurements are synchronised with the grid movement. For each wind field, a spatial mean wind velocity is defined by firstly binning all time series of the positions

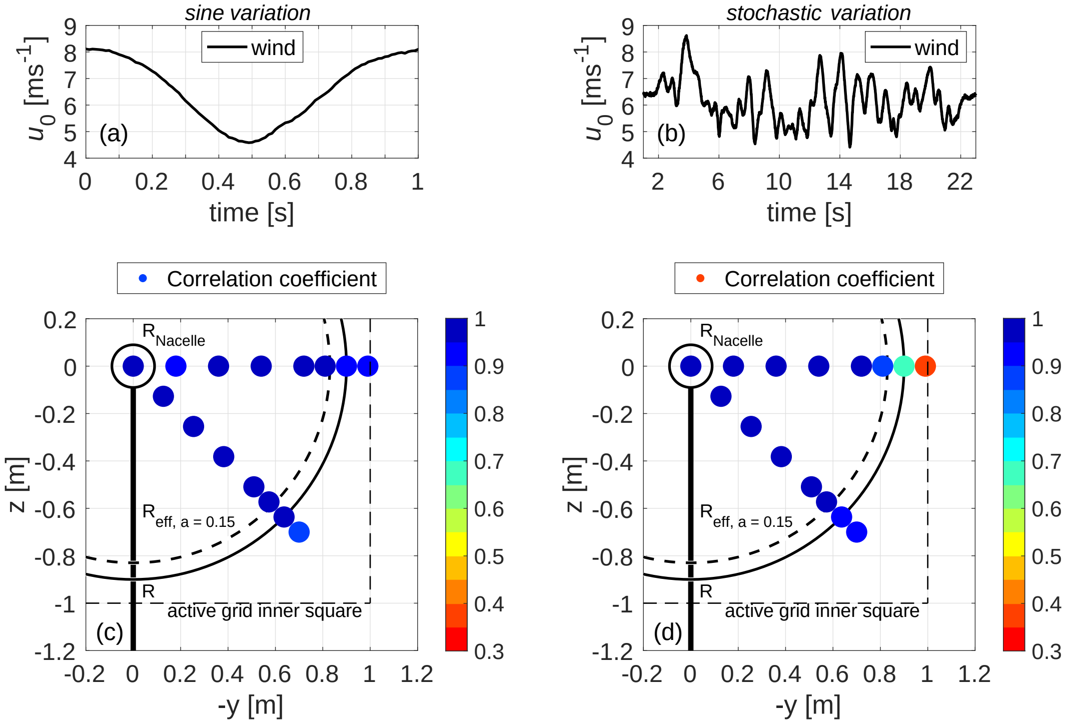

Figure 5.2: Undisturbed mean wind field of the sine (a) and stochastic (b) variation. Front view on the lower-right-hand-side quarter of the swept area of the turbine looking downstream. The colour-coded measurement positions show the Pearson correlation coefficient of the local measurement position wind velocity to the mean wind velocity for the sine (c) and stochastic (d) variation.

up to 0.9 R from the rotor axis to bins of 0.01 s and then averaging each bin. This gives a 100 Hz sampled spatial mean wind signal, as shown in Fig. 5.2a and b.

The level of uniformity over the swept area is assessed based on the Pearson correlation coefficient, as a measure of correlation of the wind velocity at single positions to the mean wind signal. It is calculated for the separately binned and averaged different positions in comparison to the spatial mean wind signal. These values are plotted colour coded at the measurement positions alongside relevant turbine dimensions in Fig. 5.2c and d. Additionally, a local stream-tube radius (R_{eff}) is plotted that takes into account the widening of the stream tube due to the induction zone at a rotor-averaged axial induction of $a = 0.15$ for the running turbine.

Correlation coefficients within the local stream-tube radius are very high for both wind fields and for the sine variation for all measured positions, as expected based on the investigation by *Neuhaus et al. (2021)*. For the stochastic variation the correlation decreases towards the edge of the active grid inner square, with still high values within R_{eff}. The level of uniformity over the rotor swept area is evaluated as sufficient for the planned investigation. In the later analyses, 95 % CIs (confidence intervals) are determined for various measured quantities. They are based on the binned data of all measurements within R_{eff}.

Cross-correlation between the mean velocity 0.7 D upstream of the turbine and the spatial mean velocity of three standstill (locked rotor) measurements in the rotor plane (0.4, 0.6 and 0.8 R) is used to obtain the time delay the wind field needs to reach the turbine from the upstream characterisation point. This time delay is needed later to align the dynamic and quasi-steady measurement signals. Comparing the measurements 0.7 D upstream of the turbine and in the rotor plane, we only see minor differences between signals. To account for possible small changes in the wind field while travelling from 0.7 D upstream of the turbine to the rotor plane, the uncertainty band will be altered in later analyses at few single instances, in order to always encase the spatial mean velocity measured in the rotor plane.

5.2.3 Measurement matrix

Aerodynamic rotor torque, thrust and flapwise blade root bending moments are obtained based on strain gauge measurements.

Additionally to the two wind fields, a staircase variation with 12 steps with a length of 25 s each and velocity range from 4.6 to 9.0 $\mathrm{m\,s^{-1}}$ is performed for a turbine characterisation. For this wind field, the speed of the wind tunnel fans is changed, and the grid flaps are at the constant open position, acting as a passive grid. The turbine is operated at a steady rotational speed of 480 $\mathrm{min^{-1}}$ and a constant pitch setting of 1° (towards feather) for all measurements with operating turbine.

The staircase wind field is characterised at five horizontal positions between 0.1 and 0.9 R at 0.7 D upstream of the turbine. LDA measurements of the streamwise velocity are performed in the rotor plane at nine radial (along x axis) positions (for the range 0.3 to 0.9 R in steps of 0.1 R and additionally at 0.25 and 0.95 R) for the operational sine and staircase variation. An overview of the test matrix with additional information on the repetitions for each wind field is given in Table 5.1.

5.2.4 Wake inductions

Measurement

The method by *Herráez et al. (2018)* is used to derive the wake induction factors. These are equal to the induction factors of a ring of an actuator disk and do not consider the

Table 5.1: Experimental test cases including number of measurement positions of the LDA and repetitions.

Turbine state	**Wind**		
	sine	*stochastic*	*staircase*
standstill	LDA 0.7 D / 0 D	LDA 0.7 D / 0 D	LDA 0.7 D
	15 pos. / 3 pos.	15 pos. / 3 pos.	5 pos.
	40 rep. per pos.	10 rep. per pos.	1 rep. per pos.
operation	LDA 0 D	no LDA	LDA 0 D
	9 pos.	-	9 pos.
	40 rep. per pos.	200 rep.	1 rep. per pos.

pos. = position; rep. = repetition

induction contribution from the individual blades. The method is derived based on the theorem of Biot–Savart. For axial and uniform flow, the rotor blades have identical loading and circulation distribution at all azimuth positions. The velocity is probed in the bisectrix of two blades. Each blade's influence on the induced velocity due to its bound circulation is counterbalanced and thus cancels out, apart from the tip and root region due to the tip and root vortex, respectively. For the main part of the blade, however, *Herráez et al. (2018)* demonstrate the good applicability to derive the actual angle-of-attack distribution and thus velocity triangles at the blade segments from the measurement-derived wake induction factors. The method was developed for steady operation; however, it was shown in a prior study in *Berger et al. (2021a)* to be also applicable to study the transient changes in induction factors, maintaining axial and uniform conditions.

In Fig. 5.3a the turbine is shown with the LDA laser beams and the probed axial (u_{ax}) and tangential (u_{ta}) velocity components at a specific radius. In Fig. 5.3b the concept of the counterbalanced bound circulation of the evenly loaded blades is sketched. At the indicated line of measurement, the downwash of the blade ahead of the indicated line counteracts the upwash of the blade behind it, and they cancel each other out. The blade at the 9 o'clock position has no influence on the measurement. *Herráez et al. (2018)* outline that the trailed vorticity cannot be captured well due to the high distance between the measurement position and the blade tip. Therefore, this method is less suited for the root and tip region of the blade. The results at 0.25 and 0.95 R should therefore be interpreted with care. The application of this method with the same 2D LDA setup on MoWiTO is presented in detail and validated for an axial velocity probe

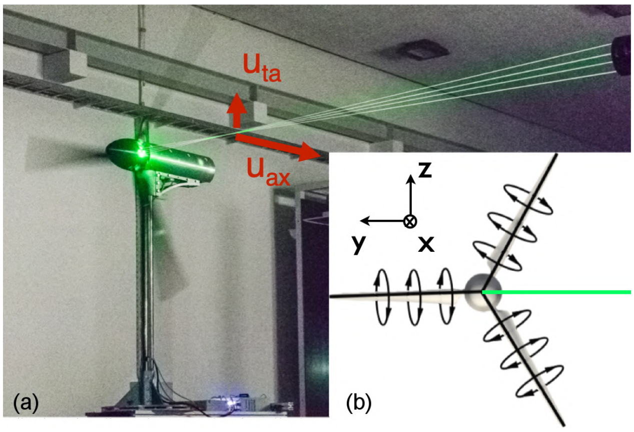

Figure 5.3: (a) MoWiTO 1.8 with 2D-LDA measurement in the bisectrix of two blades of axial and tangential velocity. (b) Counterbalancing of bound circulation for the evenly loaded blades (modified from *Herráez et al., 2018*).

over all azimuth angles at operation near design conditions in *Berger et al. (2021a)* (Sect. 2.1.3 and Appendix A). The same threshold value for the bisectrix position of the rotor azimuth angle of ±3° was applied, as this was shown to be a good compromise between data samples and quality.

The axial and tangential wake induction factors are defined by Eqs. (5.1) and (5.2), respectively. The undisturbed inflow velocity is u_0 and the rotor angular velocity Ω. With the geometrical angle of the blade segment γ, consisting of twist and pitch, the local angle of attack α at radius r can be calculated by Eq. (5.3).

$$a = 1 - \frac{u_{\mathrm{ax}}}{u_0} \tag{5.1}$$

$$a' = \frac{u_{\mathrm{ta}}}{\Omega \cdot r} \tag{5.2}$$

$$\alpha = \arctan\left(\frac{u_{\mathrm{ax}}}{u_{\mathrm{ta}} + \Omega \cdot r}\right) - \gamma \tag{5.3}$$

Load reconstruction from inductions

The measurements of u_{ax} and u_{ta} are further used to reconstruct the turbine loads. The approach is based on the blade element theory (BET), usually used within a BEM code as outlined in detail by *Hansen (2008)* to obtain the aerodynamic forces from the flow information. The relative velocity at the blade segments is defined by Eq. (5.4). The angle of attack along the span is derived from the experiment through Eq. (5.3). The aerodynamic forces for single blade elements are calculated in the normal direction (F_{N}) by Eq. (5.7) and in the tangential direction (F_{T}) by Eq. (5.8). The inflow angle is the sum of α and γ and defined by θ. The lift and drag forces of the segment are given by Eqs. (5.5) and (5.6), respectively.

$$u_{\mathrm{rel}} = \sqrt{u_{\mathrm{ax}}^2 + (u_{\mathrm{ta}} + \Omega r)^2} \tag{5.4}$$

$$F_{\mathrm{L}} = \frac{1}{2} \cdot C_{\mathrm{L}}(\alpha) \cdot \rho \cdot \Delta r \cdot c \cdot u_{\mathrm{rel}}^2 \cdot F \tag{5.5}$$

$$F_{\mathrm{D}} = \frac{1}{2} \cdot C_{\mathrm{D}}(\alpha) \cdot \rho \cdot \Delta r \cdot c \cdot u_{\mathrm{rel}}^2 \cdot F \tag{5.6}$$

$$F_{\mathrm{N}} = F_{\mathrm{L}} \cos\theta + F_{\mathrm{D}} \sin\theta \tag{5.7}$$

$$F_{\mathrm{T}} = F_{\mathrm{L}} \sin\theta - F_{\mathrm{D}} \cos\theta \tag{5.8}$$

The lift and drag coefficients are given by $C_{\mathrm{L}}(\alpha)$ and $C_{\mathrm{D}}(\alpha)$, respectively, and obtained from XFoil *(Drela, 1989)* simulations for the respective Reynolds numbers. Three-dimensional effects are accounted for through the correction model for the lift coefficient at high angles of attack by *Snel et al. (1993)*, which is mainly relevant for the root sections. The width of a blade segment is defined by Δr and the chord length by c. The tip losses are accounted for by the tip loss model by *Shen et al. (2005)* with the factor F. The segmented aerodynamic loads are integrated along the blade span to obtain the integral load signals.

5.2.5 Dynamic and quasi-steady cases

The dynamic and quasi-steady case during a gust is compared for different load and rotor flow signals. The difference between both cases results from the dynamic inflow effect. The dynamic measurement is denoted as the dynamic case. The quasi-steady case is the respective signal during the same gust without dynamic effects. They are interpolated from lookup tables based on the instantaneous gust wind speed. These lookup tables are based on a quasi-steady characterisation experiment. The processing of both the dynamic and quasi-steady signals is introduced in this subsection.

Dynamic experiment

Ensemble averages are calculated for each of the loads from the various repetitions of the two dynamic cases. For the sine gust the ensemble average of the flapwise blade root bending moment (M_{flap}) is thus based on the $N = 360$ repetitions of the sine movement, according to Eq. (5.9).

$$M_{\text{flap}}(t) = \frac{1}{N} \sum_{i=1}^{N} M^{(i)}_{\text{flap,single cycle,all blades}}(t) \tag{5.9}$$

With this approach, noise and non-deterministic variations can be reduced. Even some deterministic fluctuations, like the blade–tower interaction, are smoothed out as the start of the active grid wind protocols and the rotor azimuth position are not synchronised.

The LDA-based induction measurement data for the sine variation are processed with a similar approach. The data points within the threshold in the bisectrix of the single repetitions are synchronised with the wind field and combined to one single signal. As the rotational frequency of 8 Hz of the rotor is a multiple of the frequency of the sine at 1 Hz, there are 24 data point clusters for this three-bladed turbine over one sine period (in Sect. 5.3.2 and Fig. 5.9a to c). These data are binned to clusters, and the mean value of each bin is taken as a representative value.

Corrections are applied to the torque and thrust signals based on the strain gauge measurements. To obtain the aerodynamic rotor torque, the measurement signal is corrected for two effects. Firstly, the friction in the main shaft bearings and slip ring is added to the measured torque. This correction increases the torque by 3 % at the mean velocity of the wind fields. Secondly, there is an inertial effect of the rotor due to slight changes in the rotor speed up to ±3 %, as the controller cannot keep the rotor perfectly constant for the fast changes in wind velocity. Equation (5.10) is used to correct the torque signal by the contribution $\Delta M(t)$ associated with the angular acceleration of the rotor $\dot{\Omega}$ and inertia of the rotor and drivetrain I_{rot}.

$$\Delta M(t) = I_{\text{rot}} \cdot \dot{\Omega}(t) \tag{5.10}$$

As introduced, dynamic inflow effects can also be triggered by fast changes in rotor speed. The influence of the slight changes in rotor speed in the presented experiment are investigated with a BEM tool with the Øye dynamic inflow engineering model (see Sect. 5.2.6). As a result the influence of the dynamic inflow effect due to the rotor speed changes is considered negligible in the context of this work.

The thrust is derived from the tower bottom bending moment in fore–aft direction. The measurement is corrected for the influence of tower and nacelle drag. This drag was estimated based on a quadratic fit to a measurement of the tower bottom bending moment at various wind speeds with the turbine without installed blades.

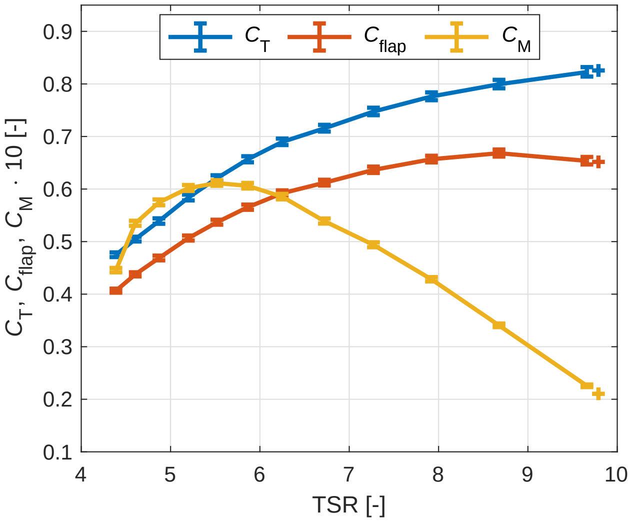

Figure 5.4: Turbine characteristics for construction of the quasi-steady case. Relevant TSR range for the sine and stochastic wind variation is TSR 5.6 to 9.5 and 5.4 to 9.8, respectively.

Quasi-steady behaviour

Quasi-steady turbine loads and rotor flow are obtained based on linear interpolation from non-dimensional lookup tables for a range of TSR and dimensionalised again. These lookup tables are based on a detailed characterisation of the turbine with the staircase wind protocol. The uncommon blade root bending moment coefficient C_{flap} is defined in Eq. (5.11). The reference bending moment is the denominator of the thrust coefficient multiplied with an additional characteristic length of $\frac{2}{3}R$, based on the representative attack point of the load for an idealised triangular normal force distribution, and the reciprocal of the number of blades n_{b}. C_{flap} and the common thrust coefficient C_{T} and torque moment coefficient C_{M} are presented over TSR in Fig. 5.4.

$$C_{\mathrm{flap}} = \frac{n_{\mathrm{b}} M_{\mathrm{flap}}}{\frac{\rho}{2} u_0^2 \pi R^2 \frac{2}{3} R} \tag{5.11}$$

Error bars indicate the quadratically added up uncertainty of inflow wind velocity and the 95 % CI of the load measurement for the 20 s long considered measurement length per wind velocity step. The additional plus sign represents an extrapolated value slightly outside of the staircase wind protocol. This extra value is needed to construct the quasi-steady loads at a single negative wind gust for the stochastic wind variation case.

The axial (see Eq. (5.1)) and tangential (see Eq. (5.2)) induction factors are obtained with the same staircase wind protocol. Based on these also the angle of attack (see

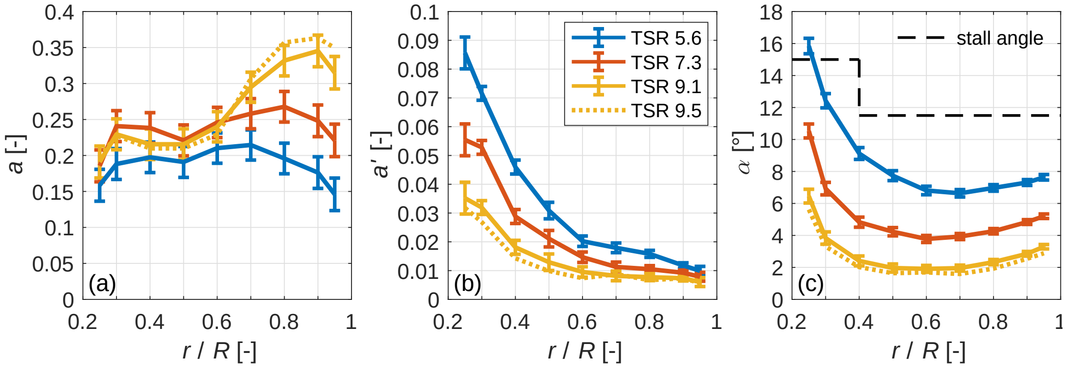

Figure 5.5: Distributions of (a) axial induction factor, (b) tangential induction factor and (c) angle of attack for different TSR. The dotted line represents a linear extrapolation.

Eq. (5.3)) is obtained. The lookup tables for the quasi-steady rotor flow are constructed for the nine considered radii and nine different TSR values (in TSR range 5.6 to 9.5). For clarity only three representative measured distributions over radius are shown in Fig. 5.5a–c.

The solid lines represent the highest, lowest and middle operational TSR configurations for the needed range of the sine case within the staircase characterisation. The error bars indicate the quadratic error of the inflow uncertainty and the 95 % CI of the induction measurement for the inductions and the propagated error for the angle of attack. Another high-TSR state is extrapolated and shown in dashed lines. This extrapolation, however, is only minor. At the highest TSR operational point in the characterisation, the rotor speed dropped due to the chosen controller settings. This led to a lower TSR value than needed for the construction of the quasi-steady signals. For the load characterisation, additional characterisations at higher rotor speed were recorded. Therefore, the highest recorded TSR in the characterisations of loads and inductions differs.

The trends for the axial and tangential induction and angle of attack are as expected. The axial induction factor (Fig. 5.5a) for the low and middle TSR setting shows a uniform spanwise distribution. We see higher values of a for higher TSR. For the high-TSR settings these values in the inner rotor half decrease again, whereas the axial induction factor is increased in the outer rotor half, compared to the TSR 7.3 case. Axial induction factors are below the design induction factor for optimal power extraction of $1/3$, apart from the tip region at the high-TSR settings where the maximum value is found at 0.36. Thus, the turbine is not operating within the turbulent wake state throughout the experiments, as can also be seen at the maximum C_T value of 0.83.

The tangential induction factor (Fig. 5.5b) has high values near the root, which decrease towards the outer part. Also, the tangential induction values generally decrease with increasing TSR for the respective radii, as expected from the decreasing momentum coefficient from the low to high TSR (see Fig. 5.4).

The angle of attack (Fig. 5.5c) is higher towards the root and similar for the range from $0.5\,R$ to the tip. The general distributions show the highest radius-dependent angles of attack for the low-TSR setting and decrease with increasing TSR. The stall angle is estimated to be at the highest lift coefficient at 15° for the root airfoil up to $0.4\,R$ and at 11.5° for the airfoil used from $0.5\,R$ to the tip. This limit is exceeded at the lowest TSR setting for the radius at $0.25\,R$. For the remaining radii at this TSR and higher TSR in general, the angles of attack are within the stall limits.

The quasi-steady turbine loads and inductions, lacking the dynamic inflow effects, are obtained for the dynamic wind field by interpolation from this characterisation. The reference wind speed of the gust at the rotor plane position is used for the construction. This reference speed is the mean of the measured 15 positions in front of the turbine, and a time delay was obtained based on minimising the root mean square error in the cross-correlation of the mean wind to the mean velocity of the three reference wind measurements in the rotor plane.

5.2.6 Øye dynamic inflow model and improved formulation for gusts

In BEM simulations, engineering models are needed to catch the dynamic inflow effect. By filtering the induced velocity, the inertia of the wake is considered, leading to a load overshoot for a sudden change in rotor load, e.g. by a fast pitch step.

The dynamic inflow effect due to a pitch step should be described by two time constants (*Pirrung and Madsen, 2018; Yu et al. 2019; Berger et al., 2021a*). The faster time constant τ_{fast} can be attributed to the sudden change in the trailed vorticity near the rotor plane and has relevant radial dependency. When that change in trailed vorticity is convected downstream with the wake, it has a more global effect and slower rate of change, described by the slower time constant τ_{slow} with little radial dependency.

A gust can also lead to fast changes in u_{ind} within relevant timescales to the dynamic inflow effect ($\tau_{\text{typ}} = R/u_0$, see *Snel and Schepers, 1994*). Such gust cases differ physically from the more classic dynamic inflow cases of a fast pitch step or rotor speed change. Considering a turbine model without any dynamic effects at constant rotational speed, a fast increase in u_0 due to a gust leads to a decrease in a (due to the reduced TSR). With the induced velocity being $u_{\text{ind}} = a \cdot u_0$, the effect of increase in u_0 on u_{ind} is partly compensated for by the decrease in a. Therefore, the dynamic inflow effect is expected to be less significant than for a pitch step (only changes a), as outlined in *Snel and Schepers (1994)*.

In the following are the formulations of the Øye dynamic inflow model and a suggested improvement to the model.

Øye model

In the Øye dynamic inflow model the steady induced velocities are filtered through two first-order differential equations as in Eqs. (5.12) and (5.13) *(Snel and Schepers, 1994; Hansen, 2008)*.

$$u_{\text{ind,int}}(t) + \tau_{\text{slow}} \frac{\mathrm{d}u_{\text{ind,int}}(t)}{\mathrm{d}t} = u_{\text{ind,qs}}(t) + k \cdot \tau_{\text{slow}} \frac{\mathrm{d}u_{\text{ind,qs}}(t)}{\mathrm{d}t} \tag{5.12}$$

$$u_{\text{ind}}(t) + \tau_{\text{fast}} \frac{\mathrm{d}u_{\text{ind}}(t)}{\mathrm{d}t} = u_{\text{ind,int}}(t) \tag{5.13}$$

$u_{\text{ind,qs}}$ is the quasi-steady induced velocity, $u_{\text{ind,int}}$ is an intermediate and u_{ind} is the final filtered induced velocity. The time constants τ_{slow} and τ_{fast} are defined by Eqs. (5.14) and (5.15), respectively, and their weighting ratio k by Eq. (5.16).

$$\tau_{\text{slow}} = \frac{1.1}{(1-1.3a)} \frac{R}{u_0(t)} \tag{5.14}$$

$$\tau_{\text{fast}} = \left[0.39 - 0.26\left(\frac{r}{R}\right)^2\right] \tau_{\text{slow}} \tag{5.15}$$

$$k = 0.6 \tag{5.16}$$

Improved formulation of Øye model for gusts

The Øye model is developed for the assumption of constant wind velocity and filters the induced velocity through two first-order differential equations. In *Schepers (2007)* the dynamic inflow effect is described for a fast change in thrust alongside the reproduced Fig. 5.6a. The trailed vorticity is formed at the blade and convected with the total local velocity, which is in parts induced by the wake. A change in bound vorticity through a pitch step modifies that vorticity, trailed into the wake. Due to the convection with a finite velocity, a mixed wake forms that consists of "old" and "new" vorticity. This mixed wake influences then the induced velocities.

Schepers (2007) estimates that the effect of this mixed wake influences the rotor flow until it has travelled 2 to 4 D, before the induced velocity has reached a new equilibrium.

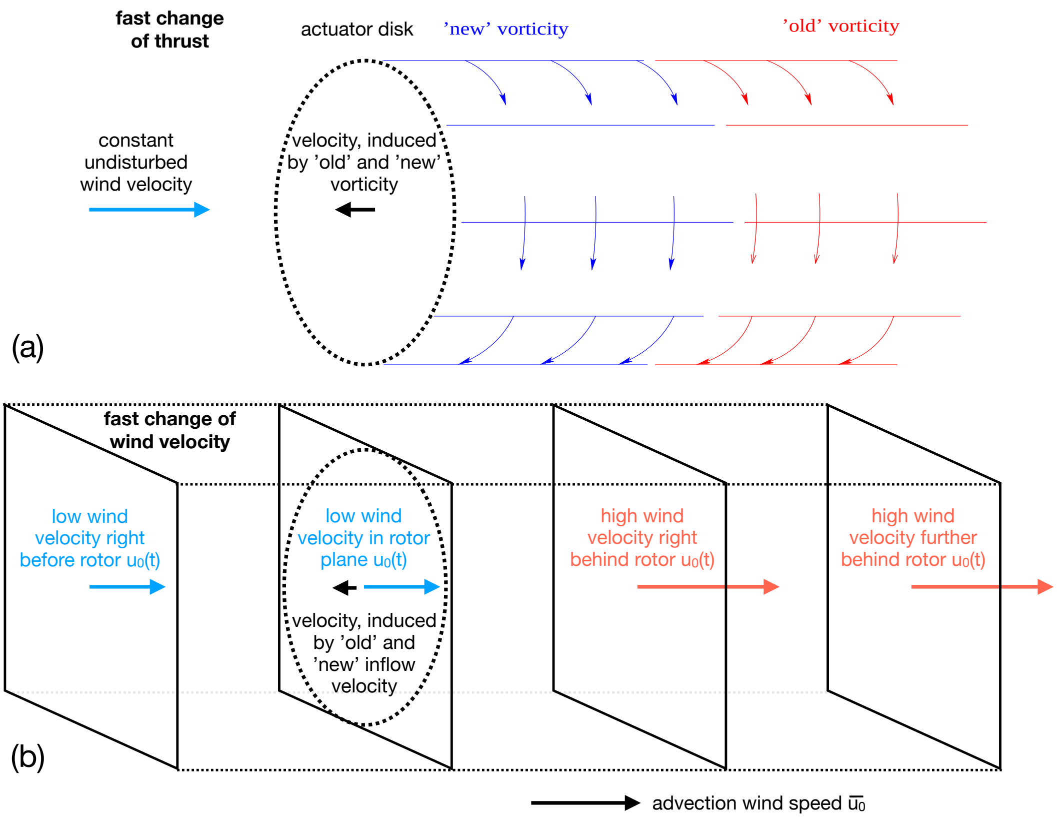

Figure 5.6: Wake with mixed vorticity as a result of a fast change in thrust (modified from *Schepers, 2007*) (a) and simplified turbulent box with coherent gust-like sudden drop in wind velocity (b).

In *Berger et al. (2021a)* a relevant distance of 2 D is estimated based on a comparison of wake measurements and dynamic turbine loads.

In Fig. 5.6b a coherent gust, in this case a rapid decrease in wind velocity, is sketched as a turbulent box with only one grid point. When this box is pushed through the wind turbine above (e.g. with the mean wind velocity of the seed as is done in BEM and FVWM simulations) in Fig. 5.6a, it also causes a change in bound vorticity that is trailed into the wake. This is covered by the original Øye model.

However, the wake with the old and new vorticity is convected by the local wind velocity, partly wake induced. For the shown case, this local wind velocity in the relevant wake distance is in parts higher than in the rotor plane. The wake is convected faster than in the assumption for the Øye model. This effect is expected to increase the axial velocity as additional air volume is pulled through the rotor by the inertia of the wake. This increases the angle of attack during the step change to lower wind velocity and thus leads to a more gradual change in the turbine load.

To include this effect in the dynamic inflow model, an additional time derivative on the undisturbed wind velocity $u_0(t)$ is added to the computation of the intermediate induced velocity ($u_{\mathrm{ind,int}}(t)$) in the Øye dynamic inflow model to the right-hand side of Eq. (5.12), which is then written as Eq. (5.17). With this extra term ($k_u \cdot \tau_{\mathrm{slow}} \frac{\mathrm{d}u_0(t)}{\mathrm{d}t}$) any change in wind velocity drives the time filter of $u_{\mathrm{ind,int}}(t)$. For constant wind velocity, the extra term has no impact and the model is essentially the original Øye dynamic inflow model.

$$u_{\mathrm{ind,int}}(t) + \tau_{\mathrm{slow}} \frac{\mathrm{d}u_{\mathrm{ind,int}}(t)}{\mathrm{d}t} = u_{\mathrm{ind,qs}}(t) + \cdot \tau_{\mathrm{slow}} \left(k \cdot \frac{\mathrm{d}u_{\mathrm{ind,qs}}(t)}{\mathrm{d}t} + k_u \cdot \frac{\mathrm{d}u_0(t)}{\mathrm{d}t} \right) \tag{5.17}$$

A good initial fit to the experiment was found with the slow time constant τ_{slow} and the factor $k_u = 0.2$.

5.2.7 Comparing simulations

Two different kinds of simulations, a BEM and a FVWM based, are used for comparison with the experimental data. For the BEM simulation the dynamic inflow engineering model is disabled to get the steady case. For the FVWM the quasi-steady cases are generated similar to the experiment. A lookup table with relevant quantities is generated based on a staircase wind input, and the quasi-steady case is obtained from linear interpolation by the respective wind field. The same airfoil polars as in Sect. 5.2.4 are used.

The first simulation environment is a BEM model programmed in MATLAB and based on *Hansen (2008)*. The BEM program considers axial and uniform inflow, considers equal loading for all blades, and features a Shen tip loss model and high thrust correction *(Buhl, 2005)*. The Øye dynamic inflow engineering model and the improved version for gusts (see Sect. 5.2.6) are implemented.

The second simulation environment is the FVWM model implemented in QBlade *(Marten et al., 2016)*. It is based on the principles of *Van Garrel (2003)*. The flow field is modelled as a potential flow. The MoWiTO blade is discretised in 15 elements, which are each modelled by a bound ring vortex, thus forming a lifting line. The circulation of these vortices is calculated iteratively based on the airfoil polars and relative velocity. The vorticity is shed and trailed at each time step. The wake convection is obtained by forward integration with a first-order method. A turbulent wind field is handled as a turbulent box that is moved through the wind turbine domain with the hub height mean wind velocity of the turbulence seed. The turbulent wind field is also used for the convection of the wake vortices. The induced velocity is influenced by the physical representation of the convecting wake, thus intrinsically modelling the dynamic inflow effect. The wake of 12 revolutions is considered, and the azimuthal discretisation is 10°.

Both model setups were already used in *Berger et al. (2020)* and showed a good match to an experimental dynamic inflow focused pitch step experiment (*Berger et al., 2021a*) with MoWiTO. For both models neither unsteady profile aerodynamics nor structural flexibility are considered, but only the aerodynamic degrees of freedom at constant rotation.

5.3 Results

At first, the integral loads for sine and stochastic wind fields are presented, comparing the quasi-steady experiment and dynamic experiment. Next, the radially resolved axial velocity and induced velocity of the sine gust is investigated. The thrust force is reconstructed based on these induction measurements. Lastly, a comparison of thrust and induced velocity for the sine gust of BEM and FVWM simulations to the experiment is presented.

5.3.1 Loads

Sine inflow variation

In Fig. 5.7, the sine wind field (Fig. 5.7a) and loads for flapwise blade root bending moment M_{flap} (Fig. 5.7b), thrust F_{thrust} (Fig. 5.7c), and aerodynamic rotor torque M_{aero} (Fig. 5.7d) of the quasi-steady experiment case and dynamic experiment case are plotted over time. The uncertainty band around the wind field shows the 95 % CI of the sine wind field altered to higher error at few positions to enclose the mean wind vector based on the three standstill measurements in the rotor plane (see Sect. 5.2.2). These alterations are mainly in the range $t = 0.1$ to $t = 0.2$ s and $t = 0.6$ to $t = 0.7$ s. The uncertainty band around the quasi-steady loads accounts for the quadratically added uncertainty in the wind velocity and the estimated error in the load characterisation (see Fig. 5.4). The uncertainty of the dynamic experiment shows the 95 % CI of the load measurement.

In the comparison of the quasi-steady case with the experiment case, the three considered load channels show similar behaviour. At the positive gust peak at $t = 0$ s, the steady case and experiment case show similar values, but they differ at the negative gust peak at $t = 0.5$ s. Here the experiment shows higher absolute loads than the quasi-steady case, thus leading to a reduction in load amplitude of the dynamic experiment by 20 % to 23 %, based on the amplitude of the quasi-steady case.

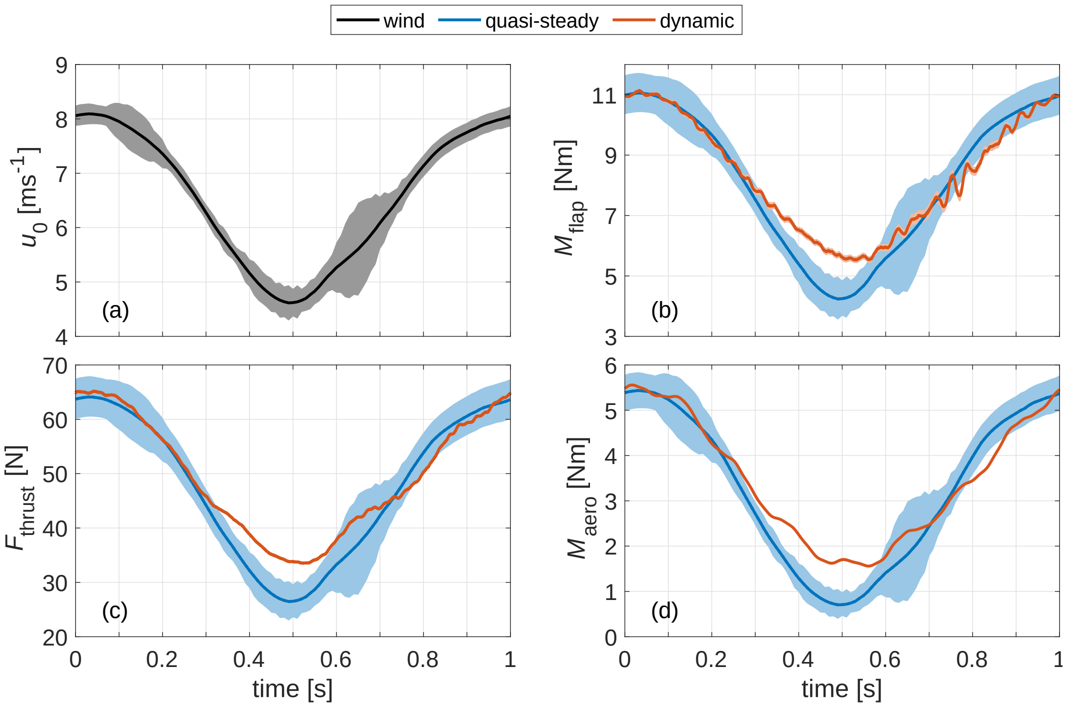

Figure 5.7: Sine wind field (a) and quasi-steady and dynamic experiment loads for flapwise blade root bending moment (b), thrust (c) and aerodynamic torque (d). The wind uncertainty shows the degree of uniformity. The uncertainty for the quasi-steady loads accounts for this non-uniformity and the uncertainty in the aerodynamic characterisation. The dynamic loads are shown along the 95 % CI.

The steady and dynamic curves differ mainly for the range of $t = 0.3$ to $t = 0.6\,\text{s}$, where the wind velocity decreases quickly and the turbine operates at high TSR and thus thrust coefficients. The dynamic loads react with a reduced change in load from $t = 0.3\,\text{s}$ on and reach the quasi-steady curve again after the wind velocity increases at $t = 0.6\,\text{s}$. For the torque, this behaviour can also be seen less pronounced for the increasing wind velocity slope around $t = 0.8\,\text{s}$.

Stochastic inflow variation

Figure 5.8 shows the wind velocity of the stochastic wind variation in Fig. 5.8a, the difference quotient of the rotor equivalent induced velocity to a relevant dynamic inflow time constant τ in Fig. 5.8b, and M_{aero} for the quasi-steady case and dynamic case in Fig. 5.8c. The uncertainty for the wind and $M_{\text{aero}}(t)$ is shown as for the sine gust. The induced velocity is estimated based on the quasi-steady thrust coefficient via the momentum balance ($C_{\text{T}} = 4a(a-1)$). The reference time constant ($\tau = \frac{1}{2}\tau_{\text{typ}}$) was chosen to be half of the typical dynamic inflow value ($\tau_{\text{typ}} = \frac{R}{u_0}$) as introduced in

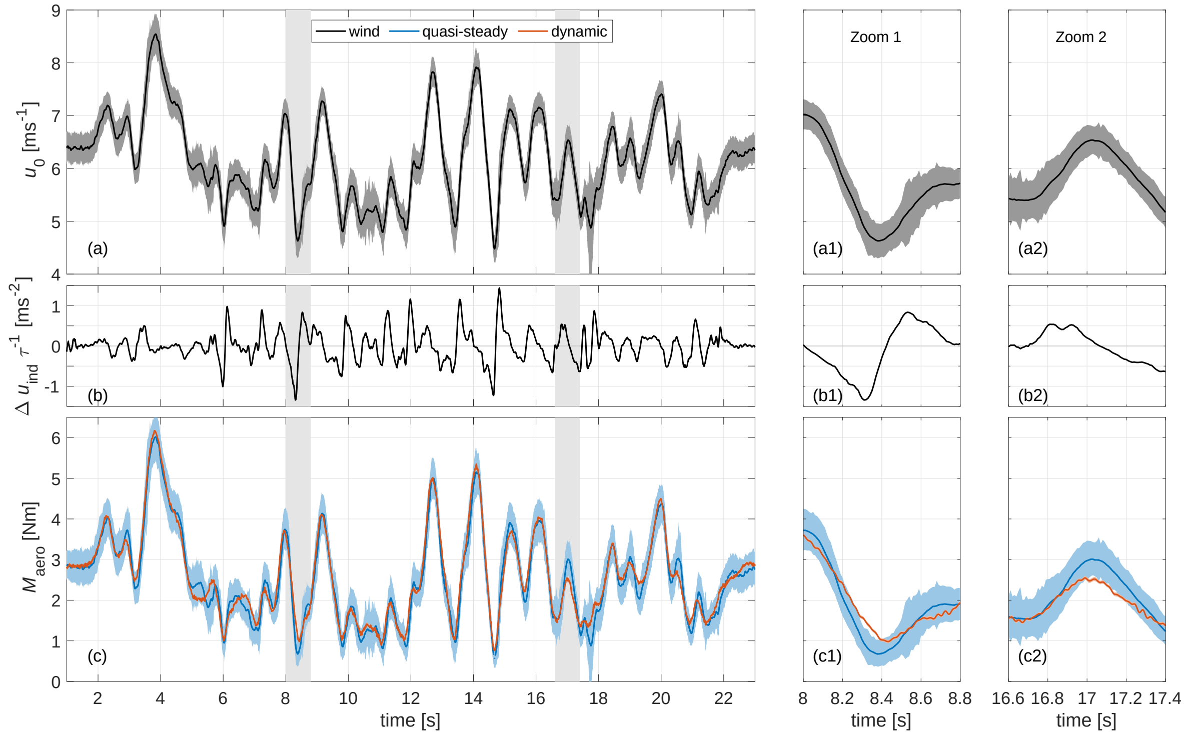

Figure 5.8: Stochastic wind variation (a), difference quotient of velocity with τ to obtain the instances of largest relevant velocity change (b), and flapwise blade root bending moment (c) for the steady case and dynamic case. Furthermore, two zoomed-in views (marked in grey in the whole time series) of situations of interest of the same data series are presented (a1, a2, b1, b2, c1, c2).

Schepers and Snel (1995)) for a simple evaluation of the dynamic inflow effect with a single time constant. This $\tau = 0.07\,\mathrm{s}$ also equals the duration of the fast pitch step in *Berger et al. (2021a)* with MoWiTO, thus giving a relatable time frame for a change in turbine loading that can lead to a clear dynamic inflow effect with this similar MoWiTO setup. The typical time constant is also commonly used as a scaling parameter in two-time-constant dynamic inflow models as can be seen in Eq. (5.14). With the difference in induced velocity $\Delta u_{\mathrm{ind}}(t) = u_{\mathrm{ind}}(t) - u_{\mathrm{ind}}(t - \tau)$, the difference quotient is $\frac{\Delta u_{\mathrm{ind}}(t)}{\tau}$. A high amount shows a fast change in induced velocity and thus indicates instances where dynamic inflow effects are to be expected based on current engineering models. Additionally, two zoomed-in views of interest, based on relevant differences between steady $M_{\mathrm{aero}}(t)$ and dynamic $M_{\mathrm{aero}}(t)$, are shown.

The comparison of the quasi-steady and dynamic $M_{\mathrm{aero}}(t)$ shows a good fit, with only two instances where the dynamic values are outside of the quasi-steady range. The first instance is shown in zoom 1. The wind velocity (Fig. 5.8a1) decreases quickly from $t = 8\,\mathrm{s}$ to $t = 8.4\,\mathrm{s}$, and the dynamic torque (Fig. 5.8c1) shows a less pronounced response, similar to the negative gust for the sine variation. The difference quotient of the induced velocity (Fig. 5.8b1) shows the absolute minimum at $t = 8.3\,\mathrm{s}$, coinciding with the maximum difference between experiment and quasi-steady case.

The second instance is around $t = 17\,\mathrm{s}$. There is a fast increase in wind velocity (Fig. 5.8a2), and the dynamic $M_{\mathrm{aero}}(t)$ (Fig. 5.8c2) does not increase as fast as for the quasi-steady case, thus leading to a less pronounced load peak for the dynamic case. The difference quotient of the induced velocity (Fig. 5.8b2), in contrast to Fig. 5.8b1, does not show an extreme value here. In general there is a slightly reduced variation of $M_{\mathrm{aero}}(t)$ of the dynamic case in comparison to the steady case, especially at the lower tipping points. Apart from the two introduced instances, these differences are all within the uncertainty range. For the two described instances, no extrapolated values were needed for the quasi-steady $M_{\mathrm{aero}}(t)$ signal.

5.3.2 Radially resolved measurement

For the sine wind field, quasi-steady and dynamic $u_{\mathrm{ax}}(t)$ and $u_{\mathrm{ind}}(t)$ are directly compared for three radii. In the next step all considered radii are used to reconstruct the rotor thrust based on the flow measurement (see Sect. 5.2.4). This way, the radial measurements are combined to a global signal, reducing uncertainty and noise.

Axial and induced velocity

In Fig. 5.9a–c, the axial velocity $u_{\mathrm{ax}}(t)$ values for three radii for the dynamic and quasi-steady cases for the sine wind field are shown. For the dynamic case the raw data samples are additionally plotted. The 95 % CI is given for both signals. For the quasi-steady case this is again altered by the mean wind velocity in the rotor plane at single instances. The dotted line for the quasi-steady case indicates the extrapolated range of the characterisation.

The steady and dynamic axial velocity shows similar behaviour for the three chosen radii. However, differences are evident at the lower tipping points. For all three radii the dynamic case shows higher $u_{\mathrm{ax}}(t)$ values here. At all radii but especially 0.4 and $0.6\,R$, a plateau can be seen in the dynamic case around $t = 0.7\,\mathrm{s}$. This effect is also indicated in the uncertainty band of the quasi-steady case but not in the dynamic load measurements. This indicates a local flow pattern that is smoothed out globally.

In Fig. 5.9d–f, the induced velocity $u_{\mathrm{ind}}(t) = u_0(t) - u_{\mathrm{ax}}(t)$ values for the steady case and dynamic case are plotted for the three radii. The reference velocity values for the steady case and dynamic case are the wind velocity $u_0(t)$ as shown in Fig. 5.7a and the

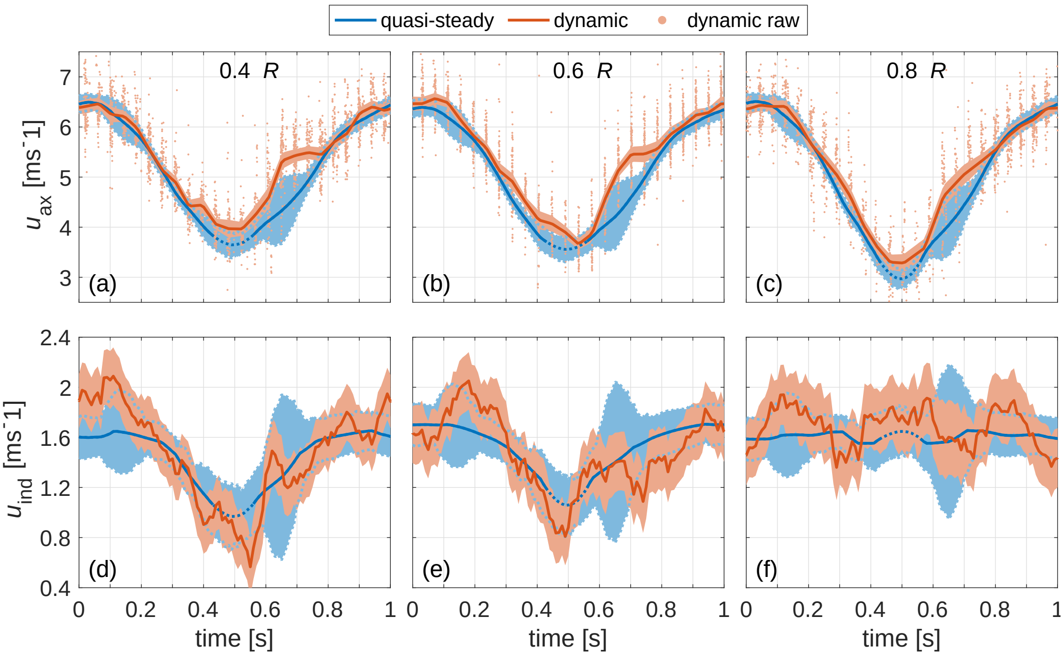

Figure 5.9: Quasi-steady and dynamic axial velocity and induced velocity for sine wind field at radii 0.4 R (a, d), 0.6 R (b, e) and 0.8 R (c, f). The 95 % CIs are given, and errors for the quasi-steady case and the induced velocity of the dynamic case were quadratically added. Note that the reference velocity values for the quasi-steady and dynamic induced velocity slightly differ.

corresponding local in-plane standstill measurement $u_{0,\text{local}}(t)$, respectively. The local reference velocity is used for a smoother representation of the sensitive induced velocity, as the local reference velocity also contains the described local flow patterns.

The quasi-steady values show a dip by $0.4\,\text{m}\,\text{s}^{-1}$ between $t = 0.3$ and $t = 0.5$ s for the radii 0.4 and 0.6 R. For 0.8 R the induced velocity is nearly constant for the whole sine wind variation.

In general the dynamic $u_{\text{ind}}(t)$ has a high level of signal noise. This can be related on the one hand to the combination of small values for $u_{\text{ind}}(t)$ and the noise in the signals $u_{0,\text{local}}(t)$ and $u_{\text{ax}}(t)$. On the other hand $u_{0,\text{local}}(t)$ and $u_{\text{ax}}(t)$ consider the same position; however, the effect of the widening stream tube around the rotor is not considered, leading to some possible mismatches in $u_{0,\text{local}}(t)$. Still the comparison gives valuable insights in the phenomenon.

At 0.8 R the dynamic $u_{\text{ind}}(t)$ does indicate a steady value but with a higher noise level. For the radius at 0.6 R, steady $u_{\text{ind}}(t)$ and dynamic $u_{\text{ind}}(t)$ start at the same level, whereas the dynamic $u_{\text{ind}}(t)$ increases from $t = 0.1$ to $t = 0.2$ s and the quasi-steady signal stays levelled. In the further course the dynamic signal decreases quicker and further from $t = 0.3$ to $t = 0.5$ s below the quasi-steady value. From there, the dynamic $u_{\text{ind}}(t)$ does

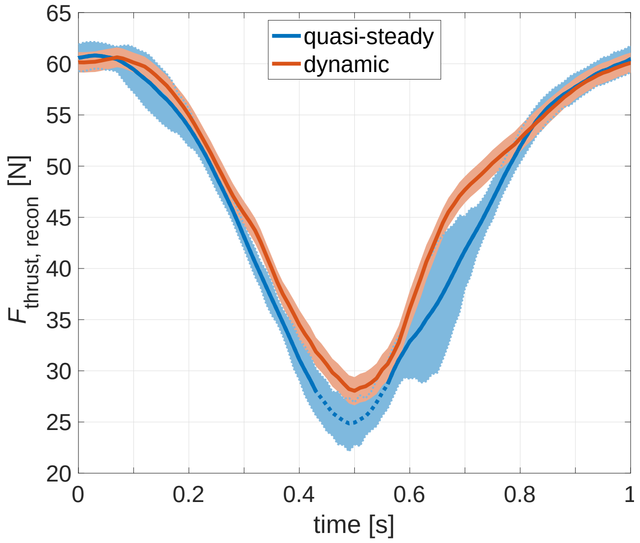

Figure 5.10: Thrust force reconstructed for the quasi-steady experiment and dynamic experiment from $u_{\mathrm{ax}}(t)$ and $u_{\mathrm{ta}}(t)$ for the sine wind variation. Quasi-steady $u_{\mathrm{ta}}(t)$ is used for both cases due to the low impact. Error bars are based on the quadratically added 95 % confidence intervals. Dotted values indicate the extrapolated characterisation.

increase to the steady value and again below it around $t = 0.7$ s, before reaching the steady level again at the end of the sine wind variation. The $0.4\,R$ case is similar, with the exception that the dynamic signal already starts at a higher value than the quasi-steady one. The differences between steady $u_{\mathrm{ind}}(t)$ and dynamic $u_{\mathrm{ind}}(t)$ are indications, as the uncertainty range of the quasi-steady case and experiment overlay. However, for some instances, e.g. for $0.4\,R$ at $t = 0$ to $t = 0.2$ s around $t = 0.55$ and $t = 1$ s, as well as for $0.6\,R$ around $t = 0.2$ and $t = 0.75$ s, there are more clear indications, as the experimental mean values are outside the uncertainty range of the quasi-steady case.

Reconstructed load

In Fig. 5.10, the thrust $F_{\text{thrust,recon}}$, reconstructed from the measured axial and tangential velocities by blade element theory (see Sect. 5.2.4), is presented. This reconstructed thrust signal essentially is a spanwise weighted representation of all the axial velocity measurements in one signal, which also can be directly compared to the strain gauge measurement and thus makes both measurements directly comparable. The steady case is based on the spatial mean wind field, as shown in Fig. 5.7. The qualitatively same effect between the quasi-steady experiment and dynamic experiment and also the general steady values as for the direct load measurements in Fig. 5.7 can be seen. The load levels at the top tipping point between the dynamic case and the quasi-steady

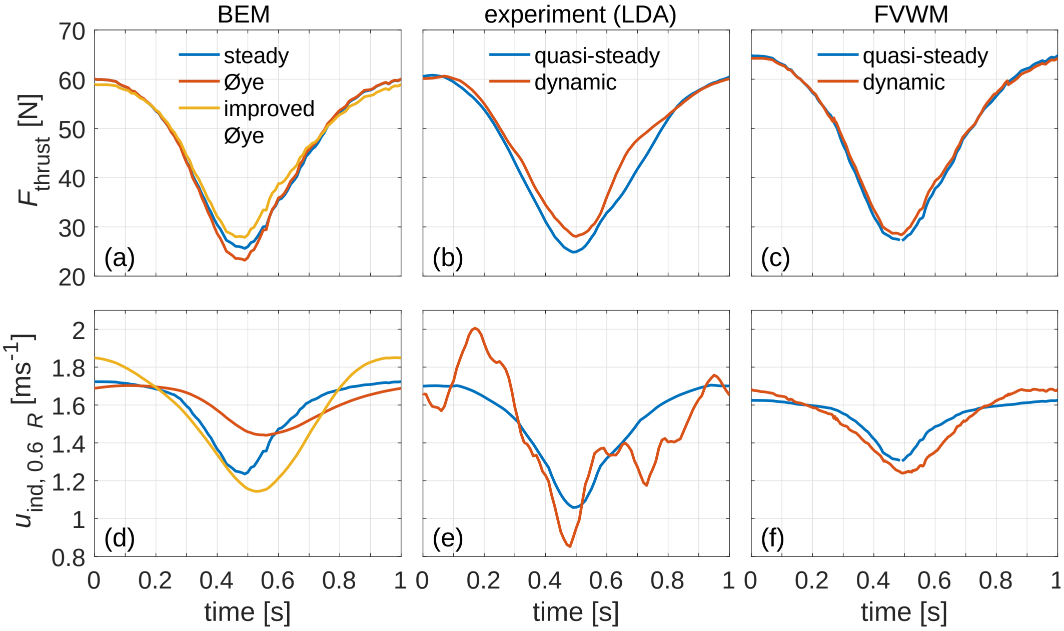

Figure 5.11: Steady and dynamic thrust (a) and induced velocity (d) at $0.6\,R$ for the sine gust for BEM simulation with the original and improved Øye dynamic inflow model and correspondingly for the experiment (b, e) and the FVWM simulation (c, f). Note that (quasi-)steady cases relate to the specific experimental/simulation setup of the dynamic case.

case are similar. At the bottom tipping point the dynamic case suggests a higher load, leading to lower load amplitude for the dynamic experiment. Due to the uncertainty range of the cases the effect is just clear around $t = 0.45\,\text{s}$. The difference at $t = 0.7\,\text{s}$ can be linked to the plateau in the axial velocity that partially is also indicated by the high uncertainty in the quasi-steady case just before that instance. In comparison to the local dynamic measurements shown in Fig. 5.9a and b, this plateau is smoothened, supporting the assumption of this plateau being a local phenomenon.

5.3.3 Sine gust in BEM and FVWM

In Fig. 5.11a $F_{\text{thrust}}(t)$ is shown for the sine wind field in BEM for steady operation without an engineering model and for dynamic operation with the Øye and the improved Øye dynamic inflow model (see Sect. 5.2.6). A clear difference can be seen between the Øye and the improved Øye model. In relation to the steady case, the Øye model leads to an increase in the load amplitude and the improved Øye model to a decrease. The difference is seen mainly at the lower tipping point.

In Fig. 5.11b and c, F_{thrust} is shown for the quasi-steady case and experimental/dynamic case for the experiment (reconstructed from the LDA measurements;

reproduced from Fig. 5.10) and the FVWM simulation, respectively. In comparison to the steady BEM simulation, quasi-steady values are similar for the experiment and overall slightly higher (about 10 %) for the FVWM simulation. These differences are negligible here, as the analysis is based on the comparison of different cases of the same simulation environment and experiment.

For experiment and FVWM, the behaviour of the dynamic case shows a reduced load amplitude in relation to the respective quasi-steady case, with the main difference at the lower tipping point at $t = 0.5$ s. The dynamic inflow effect modelled by the improved Øye implementation for BEM performs similar to the experiment, whereas the effect is less prominent but qualitatively similar in the FVWM simulation. In contrast to the experiment and FVWM, the original Øye model suggests the dynamic effect to increase the load amplitude.

In Fig. 5.11d the induced velocity $u_{\text{ind}}(t)$ at the radius of $0.6\,R$ is presented for the steady and dynamic BEM simulation – once with the original and once the improved Øye dynamic inflow model. As by design, the course of the dynamic Øye case is the filtered steady signal, reducing the amplitude of $u_{\text{ind}}(t)$ compared to the steady case. In contrast, the improved Øye model leads to a higher amplitude in $u_{\text{ind}}(t)$ compared to the steady case.

In Fig. 5.11e and f, the different quasi-steady and dynamic cases of induced velocity $u_{\text{ind}}(t)$ at the radius of $0.6\,R$ are presented for the experiment (smoothed; reproduced from Fig. 5.9e) and FVWM simulation, respectively. The quasi-steady cases of experiment and FVWM have a similar course as for the BEM simulation, with similar $u_{\text{ind}}(t)$ values at $t = 0$ s and some differences at the lower tipping point at $t = 0.5$ s. As for the thrust these differences are of secondary relevance in this analysis.

The dynamic $u_{\text{ind}}(t)$ of the FVWM simulation shows a very similar course to the improved Øye dynamic inflow model, compared to the respective (quasi-)steady case. This leads to an increased amplitude of the dynamic $u_{\text{ind}}(t)$ compared to the quasi-steady case, with slightly higher values at the high tipping point of $F_{\text{thrust}}(t)$ at $t = 1$ s and lower values at the lower tipping point at $t = 0.5$ s. The course of the experimental $u_{\text{ind}}(t)$, compared to the respective quasi-steady case, is less explicit due to the signal noise (see Sect. 5.3.2). However, the global comparison still shows similarity to the FVWM and improved Øye, leading to an increase in the experimental signal amplitude with lower values at $t = 0.5$ s.

In Appendix 5.5 two further comparison cases between the BEM simulations and FVWM are presented for validation. In the first comparison, the sine frequency is once doubled and once halved. In the second comparison the stochastic wind field is used as a case with different gust amplitudes. For both comparisons, the improved Øye model shows a similar performance to the here presented sine case.

5.4 Discussion

5.4.1 Turbine loads

The comparison of the steady and dynamic loads of the sine wind variation (see Fig. 5.7) shows a clear unsteady aerodynamic effect with a reduction in load and rotor torque amplitude for the dynamic case. The main difference is seen around the lower wind tipping point with high TSR and thus also high C_T.

The dynamic and quasi-steady loads differ for a duration of $\Delta t = 0.3\,\mathrm{s}$ between $t = 0.3$ and $t = 0.6\,\mathrm{s}$ (see Fig. 5.7). In contrast, time constants for unsteady aerodynamic effects on the profile level, like dynamic stall and the Theodorsen effect, range from 1 to 10 ms here, estimated by the ratio of chord length to relative wind velocity. The exceeding of the stall level at the root (up to $0.25\,R$) at the high wind velocity tipping point further does not coincide with the phase of interest of the sine gust. As Δt is at least 30 times higher than the typical time constant for unsteady aerodynamic effects on the profile level, a relevant contribution of unsteady profile aerodynamics on the observed effect can be ruled out.

For the stochastic wind variation (see Fig. 5.8) the same reduction in load amplitude as for the sine gust is seen. The difference quotient in mean rotor induced velocity $\left(\frac{\Delta u_\mathrm{ind}(t)}{\tau}\right)$ indicated this reduced response during a fast negative gust.

For the observed reduced load peak due to a positive gust, the $\frac{\Delta u_\mathrm{ind}(t)}{\tau}$ does not give a clear indication. Similar and higher values are seen for other instances without a clear effect in $M_\mathrm{aero}(t)$. In contrast to other positive gust peaks, the wind tipping point at $t = 17\,\mathrm{s}$ is at a lower wind speed of $6.5\,\mathrm{m\,s^{-1}}$, corresponding to a C_T value of 0.75 in contrast to 0.65 for the highest wind peaks and 0.83 for the lowest wind tipping points. Load variations at high C_T lead to more prominent dynamic inflow effects for the classic case of pitch steps.

5.4.2 Velocities in the rotor plane in experiment

The described differences between the steady and dynamic axial velocity (see Fig. 5.9) at the lower wind tipping point for the sine gust correspond to the effect seen in the load measurements. The lower drop of the axial velocity for the dynamic case at the lower load tipping point corresponds to a smaller reduction of the angle of attack at the respective radius and thus lower fluctuations in both local lift forces and integral load. This lower drop in axial velocity translates to a higher drop in induced velocity.

For $0.8\,R$, the steady case experiences a nearly constant induced velocity. Also, the dynamic case does not show strong deviations from that level. The levelled behaviour of the steady case and dynamic case at this radius is in line with current dynamic inflow modelling, which only reacts on changes in induced velocity. Amplification of the induced velocity is seen for the inner two radii for the dynamic case in comparison to the steady case for the decrease in induced velocity up to the lower tipping point.

The reconstructed steady thrust (see Fig. 5.10) based on these axial velocity measurements (see Sect. 5.2.4) shows a good match to the one based on the strain gauge measurement (see Fig. 5.7). The slight differences in the absolute levels at the tipping points (lower $-1\,\%$; upper $-5\,\%$) can be attributed to a wide range of influencing parameters including airfoil polars, tip loss model and low numbers of radii where the inductions from the experiment are available. For the direct comparison of the steady case and dynamic case, these influences cancel out as the same model is used.

For the reconstructed thrust, qualitatively the same effect as for the direct load measurement at the lower tipping point is seen, leading to a lower load amplitude for the dynamic case. The difference at the lower tipping point between the steady case and the dynamic case here is smaller, with 8 % compared to 20 % for the strain gauge measured load, each normalised by the respective quasi-steady maximum-to-minimum load difference. Considering the 95 % CI, these differences range from $-2\,\%$ to 20 % for the LDA reconstructed thrust and from 10 % to 29 % for the strain gauge measured load and do show some overlap.

For the steady and dynamic axial velocity, induced velocity, and reconstructed thrust from the rotor flow, a consistent picture to the independent load measurement is given. Therefore, despite the noticeable uncertainty range of these measurements and derived flow quantities, these data give a strong indication of the dynamic inflow effect due to gusts directly in the flow.

5.4.3 Comparison to simulations

The Øye dynamic inflow model was experimentally validated several times, showing accurate predictions for pitch steps, e.g. for integral turbine loads in *Snel and Schepers (1994)*, for the flow field transients in the wake by *Yu et al. (2016)* and for axial induction transients by *Berger et al. (2020)*. For the investigated sine gust, an increase in dynamic load amplitude is modelled (see Fig. 5.11a). In contrast to the BEM simulation with the Øye dynamic inflow model, the experiment and FVWM simulation (see Fig. 5.11b and c) suggest a decrease in dynamic load amplitude.

The increase in dynamic load within the Øye dynamic inflow model is due to the filtering of the induced velocity. Approaching the lower load tipping point in the sine gust, the lower drop in induced velocity is equivalent to a higher drop of the dynamic axial velocity. This leads to a higher drop of the angle of attack and thus lower load. This general trend of an increase in load amplitude is therefore present for all engineering models that are based on solely filtering the induced velocities (see *Schepers and Snel, 1995*, for the Øye and ECN models; *Yu et al., 2019*, for the Yu model; and *Madsen et al., 2020*, for the new DTU model).

The improved Øye dynamic inflow model (see Sect. 5.2.6) shows the same trend of a decrease in load amplitude as the experiment and the FVWM simulation. Quantitatively the difference between steady load and dynamic load at the lower wind tipping point is at 7 %, close to the difference in thrust force based on the reconstructed thrust at 8 %. The very slightly lower dynamic load at the higher wind tipping point is seen for both the improved Øye model and the FVWM simulations.

The general trend of the induced wind velocity in the improved Øye is similar to the FVWM simulation; however, the amplification of the dynamic signal is more pronounced. In comparison, the experiment also indicates a more pronounced amplification of the induced velocity than the FVWM simulations.

This lower amplification in induced velocity of FVWM is in line with the less prominent dynamic load reduction of the FVWM compared to the experiment and the BEM simulation with the improved Øye dynamic inflow model. Together, the FVWM simulations and the experiment give a first validation of the analytically motivated improvements to the Øye dynamic inflow model.

As expected, the dynamic inflow effect due to gusts is caught by the FVWM modelling approach. The less pronounced effect on the loads is suspected to be connected to the non-perfect wake convection method, which was observed in a pitch step comparison with the same FVWM model in *Berger et al. (2020)*. Well-tuned FVWM simulations, however, are expected to be a perfect basis for the development, tuning and validation of dynamic inflow models for gusts.

Given a wider experimental and numerical data basis, the additional term ($k_u \cdot \tau_{\text{slow}} \frac{\mathrm{d}u_0(t)}{\mathrm{d}t}$) for the Øye model can be further tuned. Options are to use a dedicated time constant τ_{gust} instead of τ_{slow} and to tune the parameter k_u.

5.4.4 Normalised comparison to Joule experiment and free field

In contrast to our findings, *Snel and Schepers (1994)* found no dynamic inflow effect due to gusts in their wind tunnel study with a 1.2 m diameter model wind turbine and a gust generator for approximating stepwise changes in wind velocity. Starting at an initial wind speed of $5.7\,\mathrm{m\,s^{-1}}$ they reduced the wind velocity by $0.8\,\mathrm{m\,s^{-1}}$ within 0.4 s, leading to a nearly linear decrease in induced velocity for the step to lower wind velocity by a maximum amount of $0.3\,\mathrm{m\,s^{-1}}$, estimated from simulations. Divided with the respective representative dynamic inflow time constant $\tau = \frac{1}{2}\frac{R}{u_0}$ (see Sect. 5.3.1), the maximum difference quotient of the induced velocity accounts to $\frac{\Delta u_{\mathrm{ind}}(t)}{\tau} = 0.34\,\mathrm{m\,s^{-2}}$.

For the presented experiment, there are nearly 4 times higher values at $\frac{\Delta u_{\mathrm{ind}}(t)}{\tau} = 1.28\,\mathrm{m\,s^{-2}}$, with $\Delta u_{\mathrm{ind}}(t) = 0.4\,\mathrm{m\,s^{-1}}$ within 0.2 s for $0.6\,R$ at approximately $t = 0.4$ s for the sine variation. *Snel and Schepers (1994)* already concluded that their change in wind velocity is not sufficiently fast to trigger clear dynamic inflow effects. This nearly 4 times higher $\frac{\Delta u_{\mathrm{ind}}(t)}{\tau}$ is a plausible explanation for why the effect can be seen in the present study.

Using scaling (see Sect. 5.2.1) the corresponding gust events for multi MW turbines can be estimated. This would result in a sine gust with a mean wind velocity of $9.0\,\mathrm{m\,s^{-1}}$ and amplitude of $2.5\,\mathrm{m\,s^{-1}}$ for the NREL 5 MW reference turbine with a gust length of 50 s. This is a realistic value for a gust in the open field.

5.5 Conclusions

We experimentally proved the dynamic inflow effect due to gusts for wind turbines. We tested if the Øye dynamic inflow engineering model is able to predict the effect and proposed an improvement.

Firstly, experiments under reproducible gust conditions and highly resolved measurements of the longitudinal wind field proved a dynamic inflow effect due to gusts. The effect leads to damped load amplitudes and thus reduced fatigue loads. This was observed most clearly for negative gust cases at high thrust coefficients and attributed to high changes in induced velocity. For positive gusts, the effect was less pronounced and only seen for one high-thrust-coefficient configuration.

The dynamic inflow effect is also seen in the measurements of axial flow and induced velocity in the rotor plane. The effect leads to an amplification of the induced velocities. The effect is also seen in FVWM simulations for the loads and induced velocity but with slightly lower amplitudes for the induced velocity than in the experiment. Widely applied engineering models filter the induced velocities, e.g. the Øye model *(Snel and Schepers, 1994)* in GH Bladed and OpenFAST, the new DTU model (*Madsen et al., 2020*) in HAWC2, and the ECN model *(Snel and Schepers, 1994)* in Phatas. Exemplified by the Øye model and by analytical considerations, it was shown that such an approach cannot adequately catch the dynamic inflow phenomenon due to gusts. The filtering damps the induced velocity, thus leading to higher fatigue loads. As an initial attempt to tackle the dynamic inflow effect due to gusts, we proposed an improvement in the implementation of the Øye model, adding an additional term with a time derivative filter on the wind velocity.

Now that the effect is known further, pinpointed wind tunnel experiments are needed for the development, tuning and validation of dynamic inflow models for gusts. One focus should be to further reduce uncertainties, especially in the inflow. Furthermore, the typical operation of variable-speed-controlled wind turbine in the free field is more complex than the presented wind tunnel test. Comparisons between FVWM and BEM simulations similar to *Boorsma et al., 2020* and *Perez-Becker et al. (2020)* but without sheared inflow can further shed light on the effect, and they can help to quantify the actual reduction in fatigue loads in realistic turbine operation for new dynamic inflow models. These new findings of dynamic inflow due to gusts are a major step to improved dynamic inflow modelling of gusts. The proposed improvement to the Øye dynamic inflow model already provides a possible first-generation dynamic inflow model to catch the general effect in BEM simulations. As this effect leads to lower fatigue loading of wind turbines, a proper and validated model opens up new design opportunities. For this aim, further coordinated research work is proposed, consisting of wind tunnel experiments and FVWM simulations.

Appendix

5.A Additional numerical validation cases

Two additional comparisons between the BEM model variants (steady, Øye and improved Øye model) are presented to demonstrate the applicability of the suggested approach for varying gust scenarios. The comparison is based on $u_{\text{ind}}(t)$ at a radius of $0.6\,R$.

The first comparison is designed to qualitatively relate the reaction on a sine gust case with three different frequencies. Therefore, the time period T of one sine is doubled and halved, leading to frequencies of 0.5 and 2 Hz, respectively. The results are shown in Fig. 5.12a and b for the BEM variants and the FVWM simulations, respectively. The steady BEM and quasi-steady FVWM curves as well as the solid curves at $T = 1\,\text{s}$ are identical to the ones on Fig. 5.11d and f. These curves and the differences in the (quasi-)steady values have been discussed in the context of Fig. 5.11. Here the focus is on the comparison of the additional curves in relation to the dynamic curve at $T = 1\,\text{s}$. For the BEM model with the Øye dynamic inflow model, $T = 2\,\text{s}$ leads to a larger amplitude in $u_{\text{ind}}(t)$ and $T = 0.5\,\text{s}$ to a reduced amplitude, as is expected. For the improved Øye model, the change to $T = 2\,\text{s}$ does not impact the minimum level at $0.5\,T$ but just shifts it to a slightly earlier instance. For the maximum level these are slightly below the dynamic reference case. The same qualitative observations are made for the corresponding FVWM curve. For $T = 0.5\,\text{s}$, the improved Øye model and FVWM predict similar maximum values as for their respective dynamic reference case and higher minimum values closer to the minimum values of the respective (quasi-)steady curves but both with a time delay that is most obvious in the rise from the minimum to the maximum $u_{\text{ind}}(t)$.

The qualitative changes for doubling and halving the sine frequency are caught by the improved Øye model as suggested by the FVWM.

In Fig. 5.13a and b a similar comparison is shown for the stochastic (see Fig. 5.8a) wind variation, providing various gust amplitudes starting from different wind velocities.

For the BEM case the original Øye dynamic inflow model gives a reduction in amplitude through the filtering approach, as is expected. The improved Øye model as well as the dynamic FVWM lead to higher amplitudes, compared to the respective (quasi-)steady cases. In general the behaviour in relation to the respective (quasi-)steady

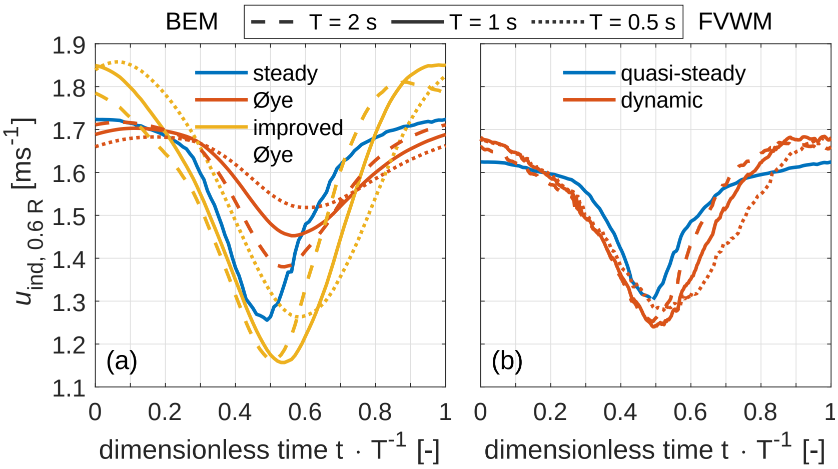

Figure 5.12: Steady and dynamic induced velocity at $0.6\,R$ for the sine gust with variations in time periods for BEM simulation with the original and improved Øye dynamic inflow model (a) and FVWM simulation (b).

case of the improved Øye model and the FVWM are similar. However, amplitudes for the dynamic FVWM are lower than estimated by the improved Øye model, especially when the induced velocity increases. In parts these differences also reflect the difference in the respective steady signal, which shows higher amplitudes for the BEM model than for the FVWM. Also, in the comparison of a pitch step experiment in *Berger et al. (2020)* with this FVWM simulation setup, an offset for the fitted slow time constant, mainly for the pitch step to high load, was seen. There it was reckoned that this is related to the wake convection in the simulation model. For a further dynamic inflow gust model development based on this FVWM setup, these differences should be further investigated.

For a quantitative comparison, the difference between the (quasi-)steady and dynamic induced velocity at each time point is compared in a scatter plot in Fig. 5.14a and b, where the y axis refers to the FVWM and the x axis to the original Øye model in Fig. 5.14a and to the improved Øye model in Fig. 5.14b.

Based on the Pearson correlation coefficient (ρ_{xy}), the improvements in the Øye model lead from a low negative correlation to a high positive correlation, showing the good match of improved Øye and FVWM. This trend is similar for other radii. The lower y slope ($0.47\,x$) is related to the mentioned general differences in amplitude of $u_{\text{ind}}(t)$ between the models.

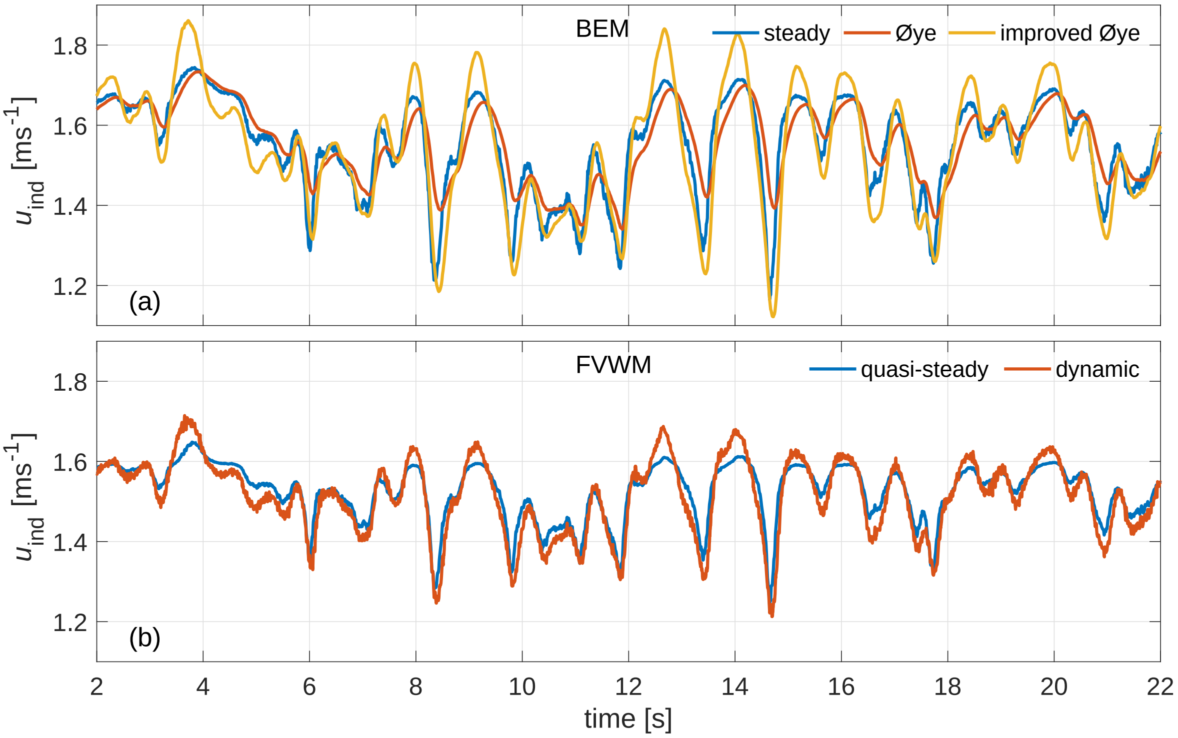

Figure 5.13: Steady and dynamic induced velocity at $0.6R$ for the stochastic gust for BEM simulation with the original and improved Øye dynamic inflow model (a) and FVWM simulation (b).

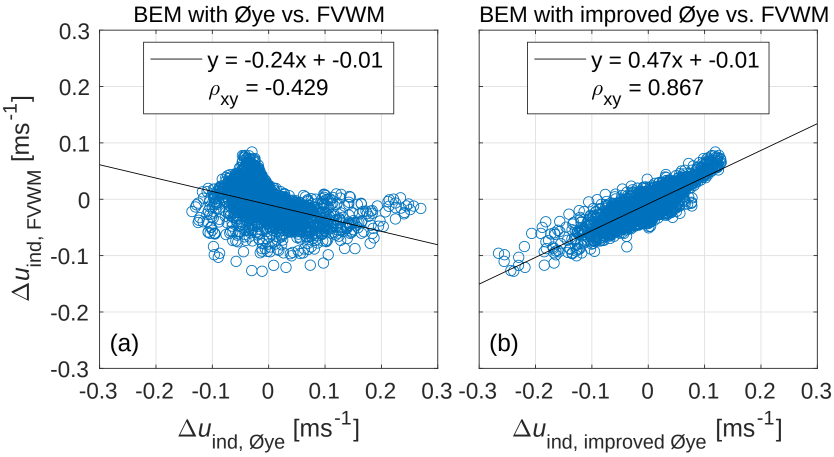

Figure 5.14: Scatter plot with correlation coefficients of the differences in u_{ind} between the (quasi-)steady and dynamic cases of the stochastic gust at $0.6R$. Comparison of FVWM and Øye in panel (a) and FVWM and improved Øye in panel (b).

Acknowledgements

This work was partially funded by the Ministry for Science and Culture of Lower Saxony through the funding initiative Niedersächsisches Vorab in the project "ventus efficiens" (reference no. ZN3024). We thank Apostolos Langidis for the help in the wind tunnel experiment; Andreas Rott for the discussions on the model improvement part; and Lars Kröger, Lisa Rademacher and Tom Wester for their help with the LDA. We would also like to thank the two reviewers, Georg Raimund Pirrung and Wei Yu, for their helpful comments and suggestions.

Chapter 6

Conclusions and Outlook

In this chapter, the main results and conclusions answering the research questions from the introduction of this thesis are summarised. In the second part, suggestions for further research questions are given.

6.1 Main results and conclusions

The dynamic inflow effect leads to an unsteady response of the induction (induced velocity and induction factors) in the rotor plane due to fast changes in rotor loading. This leads to a dynamic response of the turbine loads and thus is of importance for simulating aerodynamic wind turbine loads within the design, certification and control development process.

The main goal of this thesis was to increase the physical understanding of that effect based on a new generation of wind tunnel experiments, significantly improving on the shortcomings of prior experiments. Three main shortcomings were overcome in the present experiments. Firstly, the scaling approach of the aerodynamics of the wind tunnel model from a contemporary and representative 5 MW reference turbine on the one hand, and the realistic thrust coefficients during pitch step and gust events on the other hand, provided significantly more realistic and relevant test cases than priorly available. Secondly, with the direct probing of the axial flow and thus obtained axial and tangential induction and induced velocity, one of the main reported shortcomings of indirect measures of the phenomenon is overcome. Lastly, the large wind tunnel with an active grid enabled the creation of reproducable coherent gust situations with a sufficient amplitude and time scale to investigate the dynamic inflow effect due to gusts. Furthermore, engineering models and mid-fidelity free vortex wake methods and actuator line CFD simulations were compared to these experiments.

In the following, the main results and conclusions of the thesis are summarised, grouped into the four research questions stated in the introduction:

1. *How can a contemporary wind turbine be scaled in the wind tunnel size for experiments focused on induction aerodynamics?*
   A scaled model turbine with a diameter of 1.8 m was designed and tested (Chap. 2). This 'Model Wind Turbine Oldenburg' (MoWiTO) was scaled down based on the NREL 5MW reference wind turbine *(Jonkman et al., 2009)*. In the first step, the blades were scaled down geometrically to a diameter of 1.8 m, which is considered the maximum sensible diameter for the large wind tunnel of ForWind - University of Oldenburg. In the next step, the profiles were exchanged with two low Reynolds number profiles where the main aerodynamic airfoil is also a low lift airfoil. The chord length was increased based on the assumption of maintaining the non-dimensional lift at design conditions. This additional chord length scaling benefitted the operational chord-based Re, ranging from $50 \cdot 10^3$ at the most inner root section to $100 \cdot 10^3$ at higher radii and $75 \cdot 10^3$ to $150 \cdot 10^3$ for operation at the lowest operational speed of 400 rpm and highest operational speed of 600 rpm, respectively. The limited deflection of the stiff carbon fibre made blades is favourable for induction aerodynamic research to limit the effect of blade dynamics on the measurements. The model features individual pitch and torque control and strain gauges for integral load measurements of rotor torque, flapwise blade root bending moments and tower foot bending moments to derive the thrust.

   The aerodynamic forces and loading of the MoWiTO were compared to those of the reference turbine by means of aeroelastic simulations in a perfectly scaled turbulent wind field. This comparison showed a good match between the reference and the scaled turbine, verifying the scaling approach for induction driven experiments.

   The model was further characterised in the wind tunnel. The thrust and trend for power coefficient match the aeroelastic simulation-based ones of the reference turbine, indicating the applicability of the scaling approach again.

2. *What insights on the dynamic inflow process can be obtained from a radially resolved induction measurement of a pitch step experiment in combination with load and near wake measurements?*

   A pitch step experiment with MoWiTO was performed and analysed (Chap. 3). The thrust level was varied between a loading near the Betz optimum of $C_\mathrm{T} = 0.9$ and nearly half that value at $C_\mathrm{T} = 0.48$. This load range on the one hand is within the typical operational range of a modern wind turbine. On the other hand the difference between the load levels is large enough, and the pitch step within half a rotor revolution is fast enough to trigger a dynamic inflow effect, suitable for time-constant analysis. A recent method for the extraction of the wake induction by a one-point flow measurement in the rotor plane per radial position by *Herráez et al. (2018)* was applied for the first time to a dynamic situation by means of a 2D LDA system. The measurements of wake induction, turbine loads and flow in the near and close far wake give a comprehensive picture of the relevant quantities during a fast pitch step, at representative conditions for a modern pitch regulated wind turbine. For the first time, a clear direct experimental evidence of the dynamic inflow effect for wind turbines is presented with the shown delay of the induction factors after the pitch step. Priorly this was only shown indirectly in the wake, forces and loads.

   The time-constant analysis based on a one- and a two-time-constant model experimentally confirmed the prevalent assumption that the dynamic inflow process is better described by two time constants. The fast time constant is related to the near wake influence and the slow time constant to the close far wake. Near the blade root however, the process is similarily well defined by the one time constant model. In the two-time-constant model this can be seen by the high radial dependence near the root of the fast time constant. For the region from the mid of the blade to the tip, the fitted fast time constant indicates a slight increase for the step to high load and decreases for the step to low load, respectively. The same trend is indicated for the slow time constant.

   A dynamic wake expansion for the step to low load is observed and expected to be the reason for the radial dependency of the slow time constant. The wake measurements further experimentally confirm a common assumption that the mixed wake, consisting of old vorticity before the pitch step and new vorticity after the pitch step, convects faster for the step to low load than to high load. This is an obvious explanation for the lower time constants for the step to low load. The initial convection of the wake is found to be at nearly free stream wind velocity, indicating the strong influence of the tip vortex due to the fast change in trailed vorticity on the effect just after the pitch step.

An unexpected overshooting behaviour of the tangential induction factor was observed in the experiment. It is explained by the shed vorticity, which results from the circulation change during the pitch step. It was further found that the initial decay of the axial induction factor during the pitch step is similar for both pitch directions. Previously it was assumed that they differ significantly and are the reason for the differences in load overshoot between the pitch directions. However, within this experiment, it was shown that the turbine sensitivity to angle of attack changes at different thrust levels is the reason for the difference in load overhoot.

3. *How well do common engineering models and FVWM and CFD based AL simulation setups catch the induction and load overshoot characteristic of an experimental pitch step case?*
   The pitch step experiment has been compared to a variety of engineering models (ECN and Øye see *Snel and Schepers, 1994*, DTU see *Madsen, Larsen et al., 2020* and GDWM see *Suzuki and Hansen, 1999*) and mid fidelity AL CFD and FVWM simulations (Chap. 4). The focus was on comparison of the fitted time constants with the one- and two-time-constant model (as used in Chap. 3) on the radially resolved axial induction factor and the load overshoot. The general behaviour is caught by the engineering models and higher fidelity models, as expected.

   From the engineering models the performance of the Øye model, based on two time constants, is very close to the experiment in terms of time constants on axial induction factor, their radial trends and the load overshoot characteristic. The new DTU engineering model that is also based on two time constants also showed a close performance for the load overshoot, however more differences for the slow time constant than the Øye model. The models based on one time constant cannot be recommended.

   The mid-fidelity simulations showed in general a good performance with specific shortcomings. For the AL CFD simulation, the slow time constant is caught very accurate, however the fast time constant is underestimated, leading to reduced load overshoots. In the FVWM simulation, the picture is opposite with a good match of the fast time constant and an overestimation of the slow time constant, still leading to a very close load overshoot characteristic. In contrast to the engineering models, the radial dependency of the fast time constant for the fitted two-time-constant model near the root, as observed in the experiment, is also seen in both these simulation types.

4. *What are the characteristics of the dynamic inflow effect due to gusts and how can it be modelled by engineering models?*
   A gust experiment with MoWiTO was performed and analysed (Chap. 5). In the beginning, the reproducible and coherent gusts produced with the active grid were quantified. The dynamic inflow effect due to gusts was investigated by comparing two experimental cases. Firstly, measurements during rotor coherent gust situations were performed. Secondly, based on the gust wind speed, the quasi-steady loads and indcuced velocities were reconstructed by interpolation from a steady characterisation experiment. By comparing both cases, the dynamic inflow effect was isolated. FVWM and BEM simulations with the Øye dynamic inflow engineering model were performed with the same approach for the dynamic and a quasi-steady case.

   A clear dynamic inflow effect is observed in the turbine loads. The effect leads to reduced load amplitudes, mainly due to less pronounced response during a negative gust and at higher thrust coefficients. This effect thus leads to reduced fatigue loading compared to a quasi-steady base case.

   The axial and induced velocity measurements also strongly indicate a dynamic inflow effect. During a negative gust the axial velocity response of the dynamic case is damped in comparison to the quasi-steady base case. The induced velocity shows an amplified signal response in comparison to the quasi-steady case. The same behaviour is seen for the FVWM simulations. In contrast, the BEM simulation with the Øye dynamic inflow engineering model leads to a damped response of the dynamic induced velocity, compared to the quasi-steady case. This leads to increased load amplitudes and thus fatigue loads, contrary to the experiment and FVWM. The same is true for other engineering models that are based on a decay on exclusively the induced velocity (e.g. ECN, DTU).

   A new implementation of the Øye dynamic inflow model is proposed. There the fast and slow time constant filter the induced velocity as before, but an additional filter with the slow time constant on the inflow velocity is introduced. This leads to an unchanged pitch step performance but improves the effect of the investigated gust situations.

The conducted research within this thesis improves the general physical understanding of the dynamic inflow effect for wind turbines. The sophisticated experimental setup consisting of MoWiTO, large wind tunnel of ForWind - University of Oldenburg with active grid and 2D LDA and hot wire systems along new methods to extract the wake induction enabled a new quality of aerodynamic wind tunnel experiments for dynamic inflow investigations. These were used to test and question current assumptions and provide completely new insights to the dynamic inflow effect due to pitch steps and gust situations.

In conclusion the statement by *Peters (2009)*, that main advances in the understanding and modelling of dynamic inflow effects for helicopters have always been triggered by experimental data that did not fit the current models can also be transferred to wind turbine applications. The evolvement of the understanding and modelling of dynamic inflow effects for wind turbines in the past was heavily triggered by the experiments with the Tjæereborg turbine *(Øye, 1991)*, NREL phase VI *(Hand et al., 2001)* and MEXICO *(Schepers and Snel, 2008)* cases. In this thesis, the physical understanding of the dynamic inflow effect due to a pitch step is significantly improved. The radial trends near the root and tangential inductions do not fit current engineering models. Still, the applicability of the Øye dynamic inflow model is shown, as these are only minor influences. Furthermore, the gust experiments present a case that clearly does not fit the current engineering models. The proposed new implementation of the Øye dynamic inflow model gives a first model to catch the effect of gusts and thus to improve the quality of aeroelastic simulations based on BEM.

6.2 Suggestions for further research

Continuing the research path of this thesis and building on the findings further worthwhile research questions can be identified. There are two main points to consider to move the understanding and subsequently the modelling of the dynamic inflow effect for wind turbines to a new next level, namely non-uniform loading and combinations of dynamic inflow triggering situations.

In the presented research, the focus is on two general cases, a collective pitch step and a rotor coherent gust. Both cases are dynamic in time but not in space. The cases feature uniform blade loading for all azimuth positions of the rotor blade (neglecting tower effects). In reality, wind turbines operate in sheared and turbulent inflow due to the atmospheric boundary layer. The dynamic inflow effect in parts is due to the inertia of the wake, which is assumed axial symmetric for engineering model developments, which is not true for sheared inflow cases. Additionally, care has to be taken that dynamic inflow models do not artificially dampen the variations in induced velocity due to sheared inflow *(Madsen et al., 2012)*. For these sheared cases already the definition of the reference velocity in a BEM model is uncertain *(Boorsma et al., 2020)* and has to be investigated. Partial gusts further seem like a challenging case for current dynamic inflow models and their implementation. Lastly, non-collective pitch steps (e.g. due to pitch system faults or for advanced IPC based induction control like in *Frederik et al., 2020*) or non-cyclic flap actuations of future smart blades can be considered challenging situations for dynamic inflow models and their implementation.

The second point is the combination of pitch actuation, gusts and subsequent changes in rotor speed. In reality, the turbine reacts to an increase in wind velocity with the pitching of the rotor blades or with a change in rotor speed. Thus more than one classic trigger for dynamic inflow effects is present and the combined effect is relevant. Here no experimental studies are available until now.

Another case of interest is the dynamic inflow effect on turbines with non-uniform aerodynamic loading along the span. Here also the starting point for the design of dynamic inflow engineering models of an evenly loaded rotor disk is violated. Examples for such cases are gusts and pitch actuations at very high wind velocities and significantly pitched blades or potential future rotor concepts with an uneven blade loading by design.

Some of these tasks can be studied with a similar experimental setup as in this thesis. Flow measurements in the rotor plane with the method of *Herráez et al. (2018)* can be valuable for (axial and uniform) combined cases of coherent gusts and collective pitch steps. Further approaches, motivated from CFD, to extract the axial induction at radial positions can allow to obtain radius and azimuth resolved information of the axial induction for simple cases with non-axial inflow conditions. A promising option would be the three-point method by *Rahimi et al. (2018)*. Using the tilt option of the 2D LDA probe head and two positions for the traverse system, located to both sides of the turbine (normal to the wind direction), each point in the rotor plane can be probed. Instead of instantaneous measurements at three close measurement points (within one chord length close up- or downstream of a blade element) these could be obtained at one measurement position and a small time delay to get the same relative positions of blade element and probing point. The main challenge is the synchronisation of the blade position of the model turbine and the 2D LDA system.

FVWM, calibrated with the existing measurements presented in Chap. 3 and Chap. 5, can be further used to study more complicated scenarios. The highest outcome is expected for a combined investigation based on continued wind tunnel experiments and numerical work based on FVWM to improve the understanding of the dynamic inflow effect and the modelling and implementation in BEM based aeroelastic simulation environments. Lastly, the relevance of the dynamic inflow effect with respect to the changes in wind turbine design but also size is of interest. As the rotor diameter increases and wind conditions stay the same, the typical dynamic inflow time constant ($\tau = \frac{R}{u_o}$) increases. Blade flexibilty and typical tip deflections have also increased with increasing rotor size. Using either improved and validated BEM simulations or FVWM, compared to a quasi-steady case, the impact of the dynamic inflow effect on the different turbine scales and designs can be assessed.

References

Bastankhah, M. and F. Porté-Agel (2019). 'Wind farm power optimization via yaw angle control: A wind tunnel study'. In: *Journal of Renewable and Sustainable Energy* 11.2, p. 023301. DOI: `10.1063/1.5077038`.

Bayati, I., M. Belloli, L. Bernini, R. Mikkelsen and A. Zasso (2016). 'On the aero-elastic design of the DTU 10MW wind turbine blade for the LIFES50+ wind tunnel scale model'. In: *Journal of Physics: Conference Series* 753.2, p. 022028. DOI: `10.1088/1742-6596/753/2/022028`.

Berger, F., L. Höning, I. Herráez and M. Kühn (2020). 'Comparison of a radially resolved dynamic inflow pitch step experiment to mid-fidelity simulations and BEM'. In: *Journal of Physics: Conference Series* 1618.5, p. 052055. DOI: `10.1088/1742-6596/1618/5/052055`.

Berger, F., L. Kröger, D. Onnen, V. Petrović and M. Kühn (2018). 'Scaled wind turbine setup in a turbulent wind tunnel'. In: *Journal of Physics: Conference Series* 1104.1, p. 012026. DOI: `10.1088/1742-6596/1104/1/012026`.

Berger, F. and M. Kühn (2018). 'Experimental investigation of dynamic inflow effects with a scaled wind turbine in a controlled wind tunnel environment'. In: *Journal of Physics: Conference Series* 1037.5. DOI: `10.1088/1742-6596/1037/5/052017`.

Berger, F., D. Onnen, G. Schepers and M. Kühn (2021a). 'Experimental analysis of radially resolved dynamic inflow effects due to pitch steps'. In: *Wind Energy Science* 6.6, pp. 1341–1361. DOI: `10.5194/wes-6-1341-2021`.

Berger, Frederik, Lars Neuhaus, David Onnen, Michael Hölling, Gerard Schepers and Martin Kühn (2022). 'Experimental analysis of the dynamic inflow effect due to coherent gusts'. In: *Wind Energy Science* 7.5, pp. 1827–1846. DOI: `10.5194/wes-7-1827-2022`.

Berger, Frederik, David Onnen, Gerard Schepers and Martin Kühn (2021b). *Dataset – Radially resolved dynamic inflow pitch step experiment in wind tunnel*. Zenodo [data set]. DOI: `10.5281/zenodo.5552171`.

Boorsma, K., J. G. Schepers, S. Gomez-Iradi, I. Herraez, T. Lutz, P. Weihing, L. Oggiano, G. Pirrung, H. A. Madsen, H. Rahimi and P. Schaffarczyk (2018). *Final report of IEA Task 29, Mexnext (Phase 3)*. Tech. rep. ECN-E-18-003. Energy research Center of the Netherlands (ECN), Petten.

Boorsma, K. and J.G. Schepers (2014). *New MEXICO experiment*. Tech. rep. ECN-E-14-048. Energy research Center of the Netherlands (ECN), Petten.

Boorsma, K., F. Wenz, K. Lindenburg, M. Aman and M. Kloosterman (2020). 'Validation and accommodation of vortex wake codes for wind turbine design load calculations'. In: *Wind Energy Science* 5.2, pp. 699–719. DOI: `10.5194/wes-5-699-2020`.

Bottasso, C.L., F. Campagnolo and V. Petrović (2014). 'Wind tunnel testing of scaled wind turbine models: Beyond aerodynamics'. In: *Journal of Wind Engineering and Industrial Aerodynamics* 127, pp. 11–28. DOI: `10.1016/j.jweia.2014.01.009`.

Buhl, M.L.Jr. (2005). *A New Empirical Relationship between Thrust Coefficient and Induction Factor for the Turbulent Windmill State*. Tech. rep. NREL/TP-500-36834. National Renewable Energy Laboratory, Golden.

Campagnolo, F., C.L. Bottasso and P. Bettini (2014). 'Design, manufacturing and characterization of aero-elastically scaled wind turbine blades for testing active and passive load alleviation techniques within a ABL wind tunnel'. In: *Journal of Physics: Conference Series* 524.1, p. 012061. DOI: `10.1088/1742-6596/524/1/012061`.

Campagnolo, F., V. Petrović, J. Schreiber, E.M. Nanos, A. Croce and C.L. Bottasso (2016). 'Wind tunnel testing of a closed-loop wake deflection controller for wind farm power maximization'. In: *Journal of Physics: Conference Series* 753.3, p. 032006. DOI: `10.1088/1742-6596/753/3/032006`.

Canet, H., P. Bortolotti and C.L. Bottasso (2021). 'On the scaling of wind turbine rotors'. In: *Wind Energy Science* 6.3, pp. 601–626. DOI: `10.5194/wes-6-601-2021`.

Carpenter, P. and B. Fridovich (1953). *Effect of a Rapid Blade-Pitch Increase on the Thrust and Induced-Velocity Response of a Full-Scale Helicopter Rotor*. Tech. rep. NACA TN 3044. National Advisory Committee for Aeronautics (NACA), Washington.

Chamorro, L.P., R.E..A. Arndt and F. Sotiropoulos (2012). 'Reynolds number dependence of turbulence statistics in the wake of wind turbines'. In: *Wind Energy* 15.5, pp. 733–742. DOI: `10.1002/we.501`.

Chamorro, L.P. and F. Porté-Agel (2011). 'Turbulent flow inside and above awind farm: A wind-tunnel study'. In: *Energies* 4.11, pp. 1916–1936. DOI: `10.3390/en4111916`.

Dose, B., H. Rahimi, B. Stoevesandt and J. Peinke (2020). 'Fluid-structure coupled investigations of the NREL 5 MW wind turbine for two downwind configurations'.

In: *Renewable Energy* 146, pp. 1113–1123. DOI: `https://doi.org/10.1016/j.renene.2019.06.110`.

Drela, M. (1989). 'An Analysis and Design System for Low Reynolds Number Airfoils'. In: *Low Reynolds Number Aerodynamics*. Vol. 54. Lecture Notes in Engineering. Springer Berlin Heidelberg, pp. 1–12. DOI: `10.1007/978-3-642-84010-4`.

Ferreira, Carlos, Wei Yu, Arianna Sala and Axelle Viré (2022). 'Dynamic inflow model for a floating horizontal axis wind turbine in surge motion'. In: *Wind Energy Science* 7.2, pp. 469–485. DOI: `10.5194/wes-7-469-2022`.

Frederik, J.A., B.M. Doekemeijer, S.P. Mulders and J.W. Wingerden (2020). 'The helix approach: Using dynamic individual pitch control to enhance wake mixing in wind farms'. In: *Wind Energy* 23.8, pp. 1739–1751. DOI: `10.1002/we.2513`.

Gasch, R. and J. Twele (2012). *Wind Power Plants*. Ed. by Robert Gasch and Jochen Twele. 2nd ed. Berlin, Heidelberg: Springer Berlin Heidelberg. ISBN: 978-3-642-22937-4. DOI: `10.1007/978-3-642-22938-1`.

Giguere, P. and M.S. Selig (1998). 'New Airfoils for Small Horizontal Axis Wind Turbines'. In: *ASME Journal of Solar Energy Engineering* 120, pp. 108–114.

Hand, M.M., D.A. Simms, L.J. Fingersh, D.W. Jager, J.R. Cotrell, S. Schreck and S.M. Larwood (2001). *Unsteady Aerodynamics Experiment Phase VI: Wind Tunnel Test Configurations and Available Data Campaigns*. Tech. rep. NREL/TP–500–29955. National Renewable Energy Laboratory (NREL), Golden.

Hansen, M.H., M. Gaunaa and H.A. Madsen (2004). *A Beddoes-Leishman type dynamic stall model in state-space and indicial formulations*. Tech. rep. Risø-R-1354(EN). Risø National Laboratory, Roskilde.

Hansen, M.O.L. (2008). *Aerodynamics of Wind Turbines*. Earthscan London. ISBN: 978-1-84407-438-9.

Heißelmann, H., J. Peinke and M. Hölling (2016). 'Experimental airfoil characterization under tailored turbulent conditions'. In: *Journal of Physics: Conference Series* 753.7, p. 072020. DOI: `10.1088/1742-6596/753/7/072020`.

Herráez, I., E. Daniele and J.G. Schepers (2018). 'Extraction of the wake induction and angle of attack on rotating wind turbine blades from PIV and CFD results'. In: *Wind Energy Science* 3.1, pp. 1–9. DOI: `10.5194/wes-3-1-2018`.

Hulskamp, A.W., J.W. van Wingerden, T. Barlas, H. Champliaud, G.A.M. van Kuik, H.E.N. Bersee and M. Verhaegen (2011). 'Design of a scaled wind turbine with a smart rotor for dynamic load control experiments'. In: *Wind Energy* 14.3, pp. 339–354. DOI: `10.1002/we.424`.

Jonkman, J., S. Butterfield, W. Musial and G. Scott (2009). *Definition of a 5-MW Reference Wind Turbine for Offshore System Development*. Tech. rep. NREL/TP-500-38060. National Renewable Energy Laboratory (NREL), Golden.

Jonkman, J.M. and M.L.Jr. Buhl (2005). *FAST User's Guide*. Tech. rep. NREL/EL-500-38230. National Renewable Energy Laboratory (NREL), Golden.

Kröger, L., J. Frederik, J.W. Van Wingerden, J. Peinke and M. Hölling (2018). 'Generation of user defined turbulent inflow conditions by an active grid for validation experiments'. In: *Journal of Physics: Conference Series* 1037.5, p. 052002. DOI: `10.1088/1742-6596/1037/5/052002`.

Krogstad, P.Å. and J.A. Lund (2012). 'An experimental and numerical study of the performance of a model turbine'. In: *Wind Energy* 15.3, pp. 443–457. DOI: `10.1002/we.482`.

Madsen, H.A., T.J. Larsen, G.R. Pirrung, A. Li and F. Zahle (2020). 'Implementation of the blade element momentum model on a polar grid and its aeroelastic load impact'. In: *Wind Energy Science* 5.1, pp. 1–27. DOI: `10.5194/wes-5-1-2020`.

Madsen, H.A., V. Riziotis, F. Zahle, M.O.L. Hansen, H. Snel, F. Grasso, T.J. Larsen, E. Politis and F. Rasmussen (2012). 'Blade element momentum modeling of inflow with shear in comparison with advanced model results'. In: *Wind Energy* 15.1, pp. 63–81. DOI: `10.1002/we.493`.

Marten, .D, M. Lennie, G. Pechlivanoglou, C.N. Nayeri and C.O. Paschereit (2016). 'Implementation, Optimization, and Validation of a Nonlinear Lifting Line-Free Vortex Wake Module Within the Wind Turbine Simulation Code qblade'. In: *Journal of Engineering for Gas Turbines and Power* 138.7. DOI: `10.1115/1.4031872`.

Marten, D., J. Wendler, G. Pechlivanoglou, C.N. Nayeri and C.O. Paschereit (2013). 'Qblade : an Open Source Tool for Design and Simulation of Horizontal and Vertical Axis Wind Turbines'. In: *International Journal of Emerging Technology and Advanced Engineering* 3.3, pp. 264–269.

Martínez-Tossas, L.A., M.J. Churchfield and S. Leonardi (2015). 'Large eddy simulations of the flow past wind turbines: actuator line and disk modeling'. In: *Wind Energy* 18.6, pp. 1047–1060. DOI: `10.1002/we.1747`.

Medici, D., S. Ivanell, J.Å. Dahlberg and P.H. Alfredsson (2011). 'The upstream flow of a wind turbine: blockage effect'. In: *Wind Energy* 14.5, pp. 691–697. DOI: `10.1002/we.451`.

Moriarty, P.J. and A.C. Hansen (2005). *AeroDyn Theory Manual*. Tech. rep. National Renewable Energy Laboratory (NREL), Golden.

Neuhaus, L., F. Berger, J. Peinke and M. Hölling (2021). 'Exploring the capabilities of active grids'. In: *Experiments in Fluids* 62.6, p. 130. DOI: `10.1007/s00348-021-03224-5`.

Onnen, D. (2018). 'Aerodynamic characterization of a scaled wind turbine model in a wind tunnel and comparison to simulations based on the Blade Element Momentum Theory'. Bachelor thesis. CvO University Oldenburg.

Øye, S. (1986). 'Unsteady wake effects caused by pitch-angle changes'. In: *Proceedings of the First. IEA Symposium on the aerodynamic of wind turbines*. London, pp. 58–74.

— (1990). 'A simple vortex model of a turbine rotor'. In: *Proceedings of the Third IEA Symposium on the Aerodynamics of Wind Turbines*. Harwell, pp. 1–15.

— (1991). *Tjæreborg Wind Turbine: 4. dynamic inflow measurement*. Tech. rep. Department of Fluid Mechanics, DTH, Lyngby.

Perez-Becker, S., F. Papi, J. Saverin, D. Marten, A. Bianchini and C.O. Paschereit (2020). 'Is the Blade Element Momentum theory overestimating wind turbine loads? – An aeroelastic comparison between OpenFAST's AeroDyn and QBlade's Lifting-Line Free Vortex Wake method'. In: *Wind Energy Science* 5.2, pp. 721–743. DOI: `10.5194/wes-5-721-2020`.

Peters, D.A. (2009). 'How Dynamic Inflow Survives in the Competitive World of Rotorcraft Aerodynamics'. In: *Journal of the American Helicopter Society* 54.1, pp. 11001–1100115. DOI: `10.4050/JAHS.54.011001`.

Pirrung, G.R. and H.A. Madsen (2018). 'Dynamic inflow effects in measurements and high-fidelity computations'. In: *Wind Energy Science* 3.2, pp. 545–551. DOI: `10.5194/wes-3-545-2018`.

Pirrung, G.R., V. Riziotis, H. Madsen, M. Hansen and T. Kim (2017). 'Comparison of a coupled near- and far-wake model with a free-wake vortex code'. In: *Wind Energy Science* 2.1, pp. 15–33. DOI: `10.5194/wes-2-15-2017`.

Pitt, D.M. and D.A. Peters (1981). 'Theoretical Prediction of Dynamic-Inflow Derivatives'. In: *Vertica* 5.1, pp. 21–34.

Rahimi, H., J.G. Schepers, W.Z. Shen, N.R. García, M.S. Schneider, D. Micallef, C.J.S. Ferreira, E. Jost, L. Klein and I. Herráez (2018). 'Evaluation of different methods for determining the angle of attack on wind turbine blades with CFD results under axial inflow conditions'. In: *Renewable Energy* 125, pp. 866–876. DOI: `10.1016/j.renene.2018.03.018`.

Ryi, J., W. Rhee, U. Chang Hwang and J.S. Choi (2015). 'Blockage effect correction for a scaled wind turbine rotor by using wind tunnel test data'. In: *Renewable Energy* 79, pp. 227–235. DOI: `10.1016/j.renene.2014.11.057`.

Schepers, J.G. (2007). *IEA Annex XX : Dynamic Inflow effects at fast pitching steps on a wind turbine placed in the NASA-Ames wind tunnel*. Tech. rep. ECN-E–07-085. Energy research Center of the Netherlands (ECN), Petten.

— (2012). 'Engineering models in wind energy aerodynamics: Development, implementation and analysis using dedicated aerodynamic measurements'. PhD thesis. TU Delft, p. 319. DOI: `https://doi.org/10.4233/uuid:92123c07-cc12-4945-973f-103bd744ec87`.

Schepers, J.G., K. Boorsma, T. Cho, P. Schaffarczyk, A. Jeromin, W.Z. Shen, T. Lutz, K. Meister, B. Stoevesandt, S. Schreck, D. Micallef, R. Pereira, T. Sant and H.A. Madsen (2012). *Final report of IEA Task 29, Mexnext (Phase 1)*. Tech. rep. ECN-E–12-004. Energy research Center of the Netherlands (ECN), Petten.

Schepers, J.G., K. Boorsma, H.A. Madsen, N.N. Sørensen and W.Z. Shen (2014). *Final report of IEA Wind Task 29 : Mexnext (Phase 2)*. Tech. rep. ECN-E–14-060. Energy research Center of the Netherlands (ECN), Petten.

Schepers, J.G. and S.J. Schreck (2018). 'Aerodynamic measurements on wind turbines'. In: *Wiley Interdisciplinary Reviews: Energy and Environment* 8.1, e320. DOI: `10.1002/wene.320`.

Schepers, J.G. and H. Snel (1995). *Dynamic inflow: yawed conditions and partial span pitch control*. Tech. rep. ECN-C–95-056. Energy research Center of the Netherlands (ECN), Petten.

— (2008). *Model Experiments in Controlled Conditions - Final Report*. Tech. rep. ECN-E-07-042. Energy research Center of the Netherlands (ECN), Petten.

Schottler, J., A. Hölling, J. Peinke and M. Hölling (2016). 'Design and implementation of a controllable model wind turbine for experimental studies'. In: *Journal of Physics: Conference Series* 753.7, p. 072030. DOI: `10.1088/1742-6596/753/7/072030`.

Shen, W.Z., R. Mikkelsen, J.N. Sørensen and C. Bak (2005). 'Tip loss corrections for wind turbine computations'. In: *Wind Energy* 8.4, pp. 457–475. DOI: `https://doi.org/10.1002/we.153`.

Shirzadeh, K., H. Hangan, C. Crawford and P. Hashemi Tari (2021). 'Investigating the loads and performance of a model horizontal axis wind turbine under reproducible IEC extreme operational conditions'. In: *Wind Energy Science* 6.2, pp. 477–489. DOI: `10.5194/wes-6-477-2021`.

Snel, H., R. Houwink, J. Bosschers, W.J. Piers, G.J.W. van Bussel and A. Bruining (1993). *Sectional prediction of 3-D effects for stalled flow on rotating blades and comparison with measurements*. Tech. rep. ECN-RX-93-028. Energy research Center of the Netherlands (ECN), Petten.

Snel, H. and J.G. Schepers (1994). *Joint investigation of dynamic inflow effects and implementation of an engineering method*. Tech. rep. ECN-C-94-107. Energy research Center of the Netherlands (ECN), Petten.

Sørensen, J.N. and W.Z. Shen (2002). 'Numerical modeling of wind turbine wakes'. In: *Journal of Fluids Engineering, Transactions of the ASME* 124.2, pp. 393–399. DOI: `10.1115/1.1471361`.

Sørensen, N.N. and H.A. Madsen (2006). 'Modelling of transient wind turbine loads during pitch motion'. In: *EWEC 2006*. Vol. 1, pp. 786–795.

Soto-Valle, R., S. Bartholomay, J. Alber, M. Manolesos, C.N. Nayeri and C.O. Paschereit (2020). 'Determination of the angle of attack on a research wind turbine rotor blade using surface pressure measurements'. In: *Wind Energy Science* 5.4, pp. 1771–1792. DOI: `10.5194/wes-5-1771-2020`.

SOWFA (2nd Dec. 2019). URL: `https://nwtc.nrel.gov/SOWFA`.

Suzuki, A. and A. Hansen (1999). 'Generalized dynamic wake model for YawDyn'. In: *37th Aerospace Sciences Meeting and Exhibit*. c. American Institute of Aeronautics and Astronautics. DOI: `10.2514/6.1999-41`.

Van Engelen, T.G. and E.L. Van Der Hooft (2004). *Dynamic inflow compensation for pitch controlled wind turbines*. Tech. rep. ECN-RX-04-129. Energy research Center of the Netherlands (ECN), Petten.

Van Garrel, A. (2003). *Development of a Wind Turbine Aerodynamics Simulation Module*. Tech. rep. ECN-C-03-079. Energy research Center of the Netherlands (ECN), Petten.

Van Kuik, G.A.M., J. Peinke, R. Nijssen, D. Lekou, J. Mann, J. N. Sørensen, C. Ferreira, J. W. Van Wingerden, D. Schlipf, P. Gebraad, H. Polinder, A. Abrahamsen, G. J.W. Van Bussel, J. D. Sørensen, P. Tavner, C. L. Bottasso, M. Muskulus, D. Matha, H. J. Lindeboom, S. Degraer, O. Kramer, S. Lehnhoff, M. Sonnenschein, P. E. Sørensen, R. W. Künneke, P. E. Morthorst and K. Skytte (2016). 'Long-term research challenges in wind energy- A research agenda by the European Academy of Wind Energy'. In: *Wind Energy Science* 1.1, pp. 1–39. DOI: `10.5194/wes-1-1-2016`.

Vermeer, L.J., J.N. Sørensen and A. Crespo (2003). 'Wind turbine wake aerodynamics'. In: *Progress in Aerospace Sciences* 39.6-7, pp. 467–510. DOI: `10.1016/S0376-0421(03)00078-2`.

Winslow, J., H. Otsuka, B. Govindarajan and I. Chopra (2018). 'Basic Understanding of Airfoil Characteristics at Low Reynolds Numbers (10^4–10^5)'. In: *Journal of Aircraft* 55.3, pp. 1050–1061. DOI: `10.2514/1.C034415`.

WTTC (10th Jan. 2022). URL: `https://www.eawe.eu/organisation/committees/wind-tunnel-testing-committee/`.

Yu, W., V.W. Hong, C. Ferreira and G.A.M. van Kuik (2017). ‘Experimental analysis on the dynamic wake of an actuator disc undergoing transient loads’. In: *Experiments in Fluids* 58.10, p. 149. DOI: `10.1007/s00348-017-2432-9`.

Yu, W., V.W. Hong, C. Ferreira and G.A.M. Van Kuik (2016). In: *Journal of Physics: Conference Series* 753.2, p. 022024. DOI: `10.1088/1742-6596/753/2/022024`.

Yu, W., D. Tavernier, C. Ferreira, G.A.M. van Kuik and G Schepers (2019). ‘New dynamic-inflow engineering models based on linear and nonlinear actuator disc vortex models’. In: *Wind Energy* 22.11, pp. 1433–1450. DOI: `10.1002/we.2380`.

Appendix

A MoWiTO aerodynamic characterisation

Torque correction

The friction losses in the drivetrain between rotor and torque meter (bearings and slipring) depend on the rotor speed. They were calibrated by rotating the drivetrain with the generator operated in motor mode and using the torque meter to measure the friction in the drivetrain from torque meter to blade mount (see Fig. 2.2 (a) for the detailed drivetrain). The blades were not mounted for this calibration. The measurment is plotted in Fig. A.1 and frictional torque M_{friction} is given by Eq. (A.1).

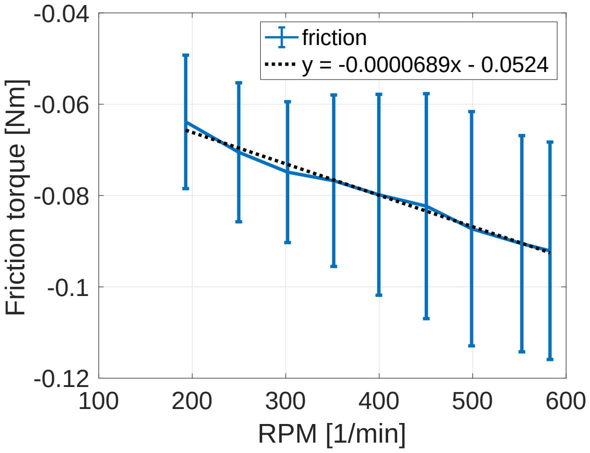

Figure A.1: Drivetrain friction calibration with uncertainty (95 % CI) and linear fit.

$$M_{\text{friction}} = (-6.89 \cdot 10^{-5} \cdot RPM \cdot 1\,\text{min} - 5.24 \cdot 10^{-2}) \cdot 1\,\text{Nm} \tag{A.1}$$

Thrust correction

The thrust correction procedure was developed by *Onnen (2018)* under the supervision of the author. The thrust of the model turbine with detached blades was derived by a wind tunnel experiment from the tower foot bending moment for a relevant range of wind velocities. This correction thrust force $\Delta F_{\mathrm{thrust,corr}}$, represented by the quadratic fit given in Eq. (A.2) has to be deducted from the actual derived thrust value.

$$\Delta F_{\mathrm{thrust,corr}} = (2.54 \cdot u^2 \cdot \frac{1\,\mathrm{s}^2}{1\,\mathrm{m}^2} + 8.45 \cdot u \cdot \frac{1\,\mathrm{s}}{1\,\mathrm{m}} + 5.14) \cdot 10^{-2} \cdot 1\,\mathrm{N} \tag{A.2}$$

The reference velocity u can be u_0 in the simplest form for the case of neglected induction effects. Alternatively a rotor effective induction can be obtained based on C_T with u as $u_{\mathrm{ax,mean}} = (1 - a_{\mathrm{eff}}) \cdot u_0$. a_{eff} is derived from momentum theory ($C_\mathrm{T} = 4a_{\mathrm{eff}} \cdot (1 - a_{\mathrm{eff}})$), and thus induction effects can be considered (for values below the turbulent wake state at $a = 0.4$). This thrust coefficient C_T is obtained in an iterative process where $u_{\mathrm{ax,mean}}$ is updated based on the updated thrust coefficient, until the thrust coefficient converges.

For design operation the error for an uncorrected thrust signal on C_T is $2.2\,\%$, whereas it is only $-0.9\,\%$ for the simplest correction form with $u = u_0$, both in relation to the corrected signal considering induction effects. For detailed characterisations thus induction effects should be considered, where for dynamic analysis the simple correction form seems more applicable, as for the dynamic inflow investigation where the momentum theory does not apply.

For further background information and illustrations the reader is forwarded to the thesis of *Onnen (2018)*.

Power and thrust characterisation

The power and thrust coefficient, including the torque correction and thrust correction including induction effects, for a characteristics over tip speed ratio at 480 rpm, 0° pitch and without a grid is presented in Fig. A.2 including an uncertainty based on the standard deviation of two combined reference hot wires, $1.5\,D$ upstream of the turbine. The values are additionally given in Tab. A.1.

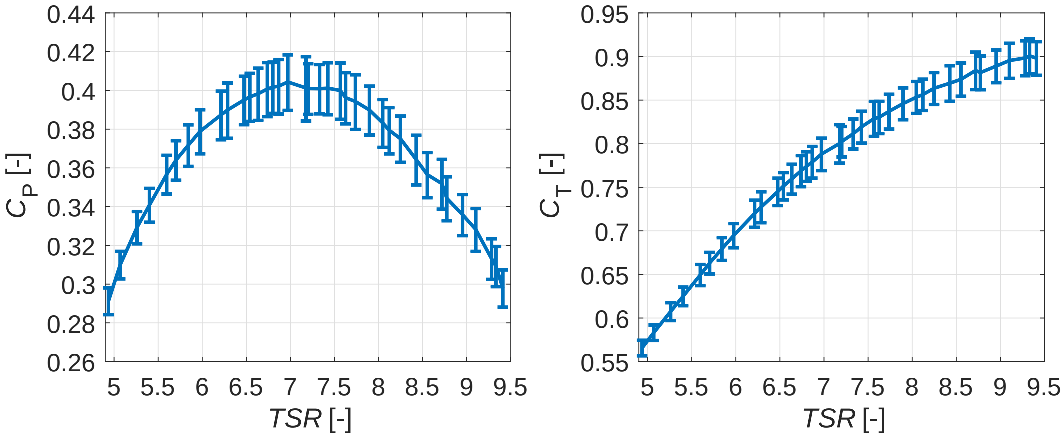

Figure A.2: Corrected power and thrust characteristic. Errorbars indicate the influence of the combined standard deviation of two used hot wires 1.5 D upstream of the turbine.

Table A.1: Power and thrust coefficient for different TSR.

TSR	C_P	C_T	**TSR**	C_P	C_T
4.94	0.291	0.566	7.33	0.401	0.811
5.07	0.310	0.583	7.42	0.401	0.819
5.26	0.329	0.607	7.57	0.400	0.829
5.40	0.341	0.625	7.57	0.400	0.829
5.60	0.357	0.649	7.63	0.396	0.830
5.70	0.364	0.663	7.74	0.394	0.837
5.84	0.372	0.679	7.90	0.390	0.846
5.98	0.379	0.695	8.05	0.383	0.853
6.21	0.387	0.720	8.12	0.379	0.856
6.29	0.390	0.727	8.25	0.375	0.864
6.47	0.395	0.745	8.43	0.364	0.869
6.54	0.397	0.751	8.55	0.357	0.874
6.63	0.398	0.760	8.72	0.352	0.884
6.74	0.401	0.769	8.77	0.344	0.882
6.80	0.402	0.774	8.95	0.336	0.889
6.87	0.402	0.779	9.10	0.328	0.895
6.97	0.404	0.788	9.28	0.313	0.898
7.18	0.401	0.800	9.33	0.309	0.901
7.20	0.401	0.803	9.41	0.298	0.898

B MoWiTO Information for aerodynamic simulations

The MoWiTO scaling process and design is outlined in Chap. 2. In Tab. B.1 the aerodynamic blade is defined. The profiles are aligned along the Aerocent ratio (relative position on chord line starting from the leading edge) of the profiles with the given twist and chord length. The geometrical blade was designed with computer aided design (CAD) based on an interpolated sweep between the stations. Three main profiles are used, a cylinder, the SG6040 and SG6041 airfoils *(Giguere and Selig, 1998)*. Differences in the profiles are due to minor corrections that had to be made for manufacturability, namely a finite TE thickness of 0.5 mm and a minimum leading edge radius of 0.5 mm. These changes showed to have negligible influence on the polars according to XFoil simulations.

In *Berger et al.* (*2021b*) the turbine information is permanently accessible alongside a dataset for the pitchsteps presented in Chap. 3 in the folder 'MoWiTO_for_simulations_2021.zip'. In this folder the respective polars and geometrical blade sections for each of the radii in Tab. B.1 are stored. A CAD file in 'step'-format is available for a single rotor blade (including the minor modifications to the tip) and a CAD file of the turbine geometry. In Fig. B.1 this turbine geometry along relevant dimensions of the MoWiTO 1.8 is sketched.

Table B.1: MoWiTO blade definition.

profile	**r [mm]**	**c [mm]**	**Aerocent**	**Twist [°]**
cylinder	90	40.000	0.5	13.08
cylinder	120	40.000	0.5	13.08
SG6040_166	166	86.000	0.33	13.08
SG6040_225	225	85.000	0.33	11.48
SG6040_281	281	81.267	0.33	10.16
SG6040_340	340	77.333	0.33	9.01
SG6040_41_interp_400	400	73.367	0.33	7.78
SG6041_459	459	69.400	0.33	6.54
SG6041_518	518	65.467	0.33	5.36
SG6041_577	577	61.533	0.33	4.19
SG6041_633	633	57.800	0.33	3.13
SG6041_693	693	53.800	0.33	2.32
SG6041_752	752	49.867	0.33	1.53
SG6041_800	800	46.667	0.33	0.86
SG6041_840	840	44.000	0.33	0.37
SG6041_900	900	40.000	0.33	0.00

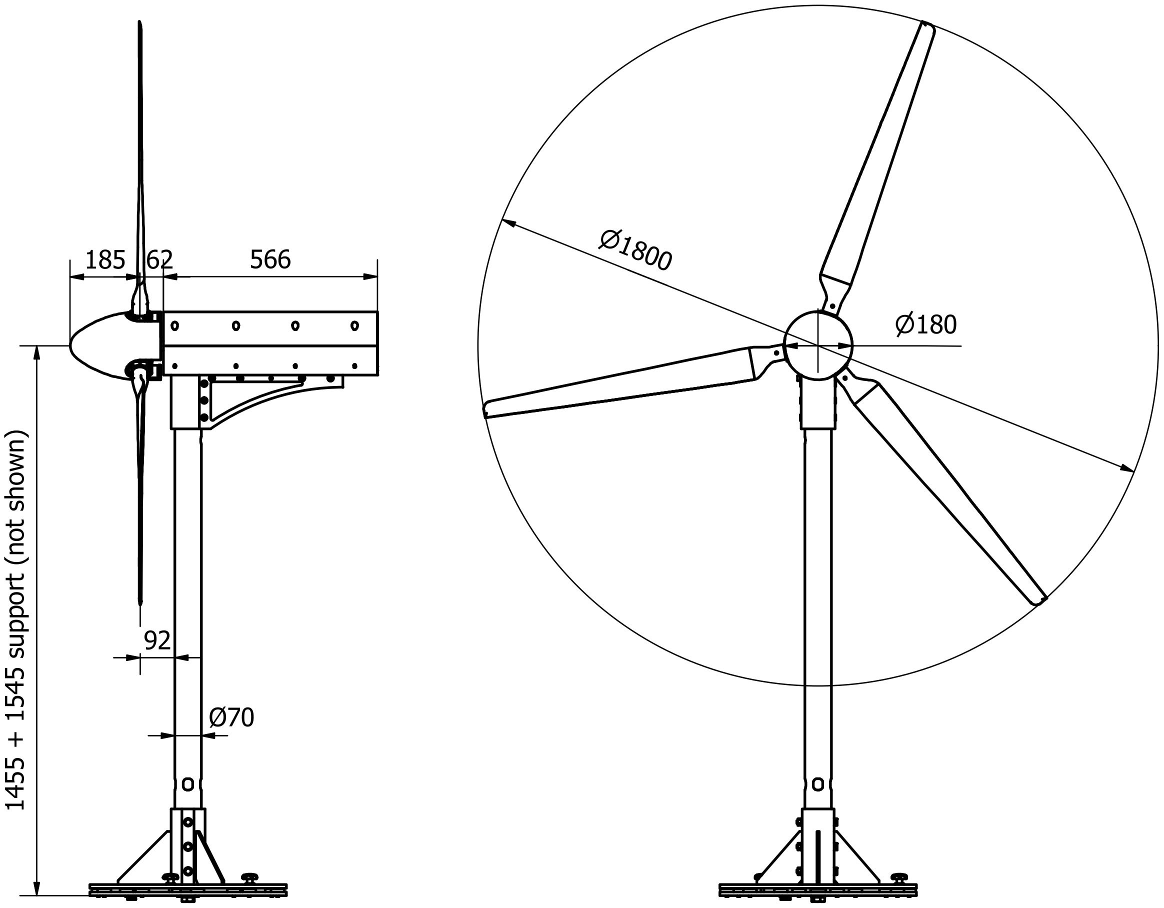

Figure B.1: Main dimensions of MoWiTO 1.8.

List of publications

Publications this thesis is based on

Journal peer-reviewed publications

- Berger, Frederik, David Onnen, Gerard Schepers and Martin Kühn (2021). 'Experimental analysis of radially resolved dynamic inflow effects due to pitch steps'. In: *Wind Energy Science* 6.6, pp. 1341–1361. DOI: `10.5194/wes-6-1341-2021`.

  Author contribution: FB performed the experiment, analysis and wrote the paper. DO assisted in the experiment and analysis. GS and MK contributed with discussions. MK supervised the work. All authors revised the paper.

  The content of this paper is reproduced in Chap. 3.

- Berger, Frederik, Lars Neuhaus, David Onnen, Michael Hölling, Gerard Schepers and Martin Kühn (2022). 'Wind tunnel analysis of dynamic inflow effects due to rotor uniform gusts'. In: *Wind Energy Science* 7.5, pp. 1827–1846. DOI: `10.5194/wes-7-1827-2022`.

  Author contribution: FB designed, performed, processed, and analysed the experiment and simulations; proposed the model improvements; and wrote the manuscript. LN developed the protocols for the active grid and assisted in the experiment. DO assisted in the experiment and protocol iterations. MH, GS and MK contributed with several fruitful discussions. MK supervised the work. All authors reviewed the manuscript.

  The content of this paper is reproduced in Chap. 5.

Conference peer-reviewed publications

- Berger, Frederik, Lars Kröger, David Onnen, Vlaho Petrović and Martin Kühn (2018). 'Scaled wind turbine setup in a turbulent wind tunnel'. In: *Journal of Physics: Conference Series* 1104, p. 012026. `DOI`: `10.1088/1742-6596/1104/1/012026`.

  Author contribution: FB designed and build the MoWiTO, performed the simulations, experiments and analysis and wrote the paper. LK made the active grid available. DO helped building the MoWiTO and perform the experiments. VP and MK contributed with discussions. MK supervised the work. All authors revised the paper.

  The content of this paper is reproduced in Chap. 2.

- Berger, Frederik, Leo Höning, Iván Herráez and Martin Kühn (2020). 'Comparison of a radially resolved dynamic inflow pitch step experiment to mid-fidelity simulations and BEM'. In: *Journal of Physics: Conference Series* 1618, p. 052055. `DOI`: `10.1088/1742-6596/1618/5/052055`.

  Author contribution: FB performed the analysis, wrote the paper, set up and performed all simulations but the AL simulations. LH set up and performed the AL simulations and wrote the subsection about the AL setup. IH and MK contributed with discussions. MK supervised the work. All authors revised the paper.

  The content of this paper is reproduced in Chap. 4.

Further publications

Journal peer-reviewed publications

- Sedano, Camilo A., Frederik Berger, Hamid Rahimi, Omar D. Lopez Mahija, Martin Kühn and Bernhard Stoevesandt (2019). 'CFD Validation of a Model Wind Turbine by Means of Improved and Delayed Detached Eddy Simulation in OpenFOAM'. In: *Energies* 12.7, p. 1306. `DOI: 10.3390/en12071306`.

- Neuhaus, Lars, Frederik Berger, Joachim Peinke and Michael Hölling (2021). 'Exploring the capabilities of active grids'. In: *Experiments in Fluids* 62.6, p. 130. `DOI: 10.1007/s00348-021-03224-5`.

- Pöschke, Florian, Vlaho Petrović, Frederik Berger, Lars Neuhaus, Michael Hölling, Martin Kühn and Horst Schulte (2021). 'Model-based wind turbine control design with power tracking capability: a wind-tunnel validation'. In: *Control Engineering Practice* 120, p. 105014. `DOI: 10.1016/j.conengprac.2021.105014`.

Conference peer-reviewed publications

- Berger, Frederik and Martin Kühn (2018). 'Experimental investigation of dynamic inflow effects with a scaled wind turbine in a controlled wind tunnel environment'. In: *Journal of Physics: Conference Series* 1037.5, p. 052017. `DOI: 10.1088/1742-6596/1037/5/052017`.

- Petrović, Vlaho, Frederik Berger, Lars Neuhaus, Michael Hölling and Martin Kühn (2019). 'Wind tunnel setup for experimental validation of wind turbine control concepts under tailor-made reproducible wind conditions'. In: *Journal of Physics: Conference Series* 1222.1., p. 012013. `DOI: 10.1088/1742-6596/1222/1/012013`.

- Sinner, Michael, Vlaho Petrović, Frederik Berger, Lars Neuhaus, Martin Kühn and Lucy Y. Pao (2020). 'Wind tunnel testing of an optimal feedback/feedfoward control law for wind turbines'. In: *IFAC-PapersOnLine* 53.2, pp. 12638–12643. `DOI: 10.1016/j.ifacol.2020.12.1838`.

- Langidis, Apostolos, Simon Nietiedt, Frederik Berger, Lars Kröger, Vlaho Petrović, Tom T.B. Wester, Gerd Gülker, Martina Göring, Robin Rofallski, Thomas Luhmann and Martin Kühn (2022). 'Design and evaluation of rotor blades for fluid structure interaction studies in wind tunnel conditions'. In: *Journal of Physics: Conference Series* 2265.2., p. 022079. `DOI: 10.1088/1742-6596/2265/2/022079`.

- Ribnitzky, Daniel, Frederik Berger and Martin Kühn (2022). ‘Innovative aerodynamic rotor concept for demand-oriented power feed-in of offshore wind turbines’. In: *Journal of Physics: Conference Series* 2265.3., p. 032017. `DOI`: `10.1088/1742-6596/2265/3/032017`.

Conference proceedings

- Berger, Frederik and Martin Kühn (2015). ′Investigating the aerodynamic implications of slender wind turbine blade design′. In Proceedings: *Proceedings of the German Wind Energy Conference DEWEK 2015*, Bremen, Germany.

Conference presentations

- as presenter

- Berger, Frederik and Martin Kühn (2015). ′Investigating the aerodynamic implications of slender wind turbine blade design′. At: *Deutsche Windenergie Konferenz (DEWEK)*, May 2015, Bremen, Germany. Oral presentation.
- Berger, Frederik and Martin Kühn (2015). ′Aerodynamic scaling of a generic wind turbine blade for wind tunnel investigations’. At: *EAWE PHD Seminar*, September 2015, Stuttgart, Germany. Oral presentation.
- Berger, Frederik, Michael Hölling and Martin Kühn (2017). ′Scaled wind turbine test setup in a wind tunnel with active turbulence generation for induction aerodynamics, load and control experiments′. At: *WindTech*, October 2017, Boulder, Colorado, USA. Oral presentation.
- Berger, Frederik, Lars Kröger, David Onnen, Vlaho Petrović and Martin Kühn (2018). ‘Scaled wind turbine setup in a turbulent wind tunnel′. At: *EERA DeepWind*, January 2018, Trondheim, Norway. Oral presentation.
- Berger, Frederik and Martin Kühn (2018). ‘Experimental investigation of dynamic inflow effects with a scaled wind turbine in a controlled wind tunnel environment’. At: *The Science of Making Torque from Wind (TORQUE)*, June 2018, Milan, Italy. Oral presentation.
- Berger, Frederik, Lars Neuhaus, David Onnen, Michael Hölling and Martin Kühn (2019). ‘Dynamic inflow due to gusts – an experimental wind tunnel study‘. At: *Wind Energy Science Conference*, June 2019, Cork, Ireland. Oral presentation.

- Berger, Frederik, Leo Höning, Iván Herráez and Martin Kühn (2020). 'Comparison of a radially resolved dynamic inflow pitch step experiment to mid-fidelity simulations and BEM'. At: *The Science of Making Torque from Wind (TORQUE)*, September 2020, Delft, The Netherlands, (online). Oral presentation.

- as co-author

- Petrović, Vlaho, Frederik Berger, Lars Neuhaus, Michael Hölling and Martin Kühn (2019). 'Wind tunnel setup for experimental validation of wind turbine control concepts under tailor-made reproducible wind conditions'. At: *WindEurope*, April 2019, Bilbao, Spain. Oral and poster presentation.

- Kröger, Lars, Dominik Traphan, Frederik Berger, Tom T.B. Wester, Vlaho Petrović, Joachim Peinke and Gerd Gülker (2019). 'Investigation of dynamic stall on a rotating model wind turbine using high speed PIV' At: *Wind Energy Science Conference*, June 2019, Cork, Ireland. Oral presentation.

- Langidis, Apostolos, Frederik Berger and Martin Kühn (2019). 'Aero-elastic scaled blade design of a model wind turbine'. At: *Wind Energy Science Conference*, June 2019, Cork, Ireland. Oral presentation.

- Neuhaus, Lars, Frederik Berger, Joachim Peinke, and Michael Hölling (2019). 'Capturing wind turbine power curve and dynamics by atmospheric-like inflow at lab-scale'. At: *Wind Energy Science Conference*, June 2019, Cork, Ireland. Oral presentation.

- Onnen, David, Frederik Berger, and Martin Kühn. 'Error Analysis of Local Aerodynamic Loads: Comparison of Measurements and BEM of a 1.8 m Model Turbine'. At: *Wind Energy Science Conference*, June 2019, Cork, Ireland. Oral presentation.

- Petrović, Vlaho, Frederik Berger, Lars Neuhaus, Oliver Huxdorf, Johannes Riemenschneider, Jochen Wild, Michael Hölling and Martin Kühn (2019). 'Wind tunnel validation of wind turbine load reducing concepts based on individual pitch control and blades with rigid leading edge slats'. At: *Wind Energy Science Conference*, June 2019, Cork, Ireland. Oral presentation.

- Peinke, Joachim, Lars Neuhaus, Lars Kröger, Frederik Berger, Martin Kühn and Michael Hölling (2019). 'Active grid in a wind tunnel used for wind energy research'. At: *NAWEA / WindTech*, October 2019, Amherst, Massachusetts, USA. Poster presentation.

- Sinner, Michael, Vlaho Petrović, Frederik Berger, Lars Neuhaus, Martin Kühn and Lucy Y. Pao (2020). ‘Wind tunnel testing of an optimal feedback/feedfoward control law for wind turbines’. At: *IFAC World Congress*, July 2020, Berlin, Germany, (online). Oral presentation.

- Langidis, Apostolos, Simon Nietiedt, Frederik Berger, Lars Kröger, Vlaho Petrović, Tom T.B. Wester, Gerd Gülker, Martina Göring, Robin Rofallski, Thomas Luhmann and Martin Kühn (2022). ‘Design and evaluation of rotor blades for fluid structure interaction studies in wind tunnel conditions’. At: *The Science of Making Torque from Wind (TORQUE)*, June 2022, Delft, The Netherlands. Oral presentation.

- Ribnitzky, Daniel, Frederik Berger and Martin Kühn (2022). ‘Innovative aerodynamic rotor concept for demand-oriented power feed-in of offshore wind turbines’. At: *The Science of Making Torque from Wind (TORQUE)*, June 2022, Delft, The Netherlands. Oral presentation.

Acknowledgements

First of all want to thank my supervisor and first referee Prof. Dr. Martin Kühn for the opportunity to pursue this work in the research group Wind Energy Systems at the Institute of Physics - University of Oldenburg and part of ForWind. His encouraging supervision, creative ideas and discussions contributed substantially to this work. I am grateful to Prof. Dr. Gerard Schepers for motivating me to look into the dynamic inflow effect and the several discussions over the years on the topic. Furthermore I want to thank Prof. Dr. Carlos Simão Ferreira for the effort to review this thesis as the second referee.

For further important input I would like to thank Dr. Filippo Campagnolo of TUM for giving me helpful hints on the practical model turbine design and Prof. Dr. Iván Herráez for motivating me to use the method for the induction extraction.

I enjoyed working, discussions, coffee breaks and barbeques with my colleagues from WeSys and also TWiSt and ForWind in general. I am further grateful for exchanges and also cooperation with various people in the national and international wind energy research community. I want to thank Stanislav Rockel who was responsible for my fast integration also in the TWiSt group. Special thanks to all the people who spend long hours in the wind tunnel with me during either joint measurement campaigns or helped me with MoWiTO, measurement equipment, software, the active grid and simulations, namely Agnieszka Hölling, Apostolos Langidis, Dominik Traphan, Gerrit Kampers, Hendrik Heißelmann, Ingrid Neunaber, Jannik Schottler, Jarek Puczylowski, Jörge Schneemann, Lars Kröger, Lars Neuhaus, Leo Höning, Lisa Rademacher, Martin Kraft, Mike Hölling, Tom Wester and Vlaho Petrović. I want to thank for and highlight the contributions from the (at that time) students David Onnen and Johannes Krauß, whose help in getting MoWiTO running was quite significant. I want to especially thank Stephan Voß, Andreas Rott and Marc Bromm for the nice lunch breaks and fruitful discussions. I especially thank Andreas for internal reviews on papers and this thesis and valuable ideas and inputs to data processing, as well as Stephan for his help in designing, assemblying and troubleshooting MoWiTO and the very cheerful time we had, sharing an office.

I want to thank my friends and family for their support, especially my father for proofreading the thesis and my mother for her help with the defence catering. Most importantly, I want to thank my wife Maria, who came to Oldenburg with me (then as my girlfriend) and shouldered the stressful times during wind tunnel campaigns and especially the last months of writing this thesis where also our second child was born.

Furthermore, I appreciate the financial support given by the German Ministry for Economic Affairs and Energy (project ’Smart Blades 2’ 0324032D), the Ministry for Education, Science and Culture of Lower Saxony (project ’ventus efficiens’ ZN3024) and the working group WeSys.

Curriculum Vitae

Personal:

Name	Frederik Thore Berger
Place of birth	Baden, Switzerland

Education:

10/2006 – 03/2014	Dipl.-Ing. Mechanical Engineering Specialisations: Fluid Mechanics and Metrology Friedrich-Alexander University Erlangen-Nuremberg
07/2010 – 12/2010	Semester Abroad Mechanical Engineering University of Cape Town, South Africa
09/1996 – 06/2006	High School Diploma (Abitur) Emil-von-Behring Gymnasium Spardorf

Scientific Experience:

11/2018 – 06/2022	Doctoral Candidate in group Wind Energy Systems Carl von Ossietzky University Oldenburg Supervision: Prof. Dr. Martin Kühn

Work Experience:

01/2022 –	Data Scientist at ENERCON, Westerstede
09/2014 – 01/2022	Research Assistant in group Wind Energy Systems Carl von Ossietzky University Oldenburg
11/2012 – 02/2013	Intern for CFD focused gas turbine R&D Siemens AG sector Energy, Berlin
03/2011 – 07/2012	Working Student (with gap) for combined cycle gas power plant commission Siemens AG sector Energy, Erlangen
04/2010 – 07/2010	Intern for manufacturing improvements of wind turbine gearboxes Bosch Rexroth AG, Nuremberg
02/2007 – 04/2010	Working Student (with gap) for project management AREVA NP GmbH, Erlangen

Erklärung

Ich erkläre hiermit, dass

- (a) eine Promotion zum Dr.-Ing. angestrebt wird,
- (b) ich diese Arbeit selbständig verfasst und nur die angegebenen Hilfsmittel benutzt habe, und dass die Arbeit in Teilen bereits veröffentlicht bzw. zur Veröffentlichung eingereicht wurde,
- (c) diese Dissertation weder in ihrer Gesamtheit noch in Teilen einer anderen Hochschule zur Begutachtung in einem Promotionsverfahren vorgelegen hat.

Oldenburg, 14.01.2022

....

(Frederik Thore Berger)